Skyrmion dynamics in magnetic thin films

Gan Weiliang

SCHOOL OF PHYSICAL AND MATHEMATICAL SCIENCES

2019

Skyrmion dynamics in magnetic thin films

Gan Weiliang

SCHOOL OF PHYSICAL AND MATHEMATICAL SCIENCES

A thesis submitted to the Nanyang Technological
University in partial fulfilment of the requirement for the
degree of Doctor of Philosophy

2019

Statement of Originality

I hereby certify that the work embodied in this thesis is the result of original research done by me except where otherwise stated in this thesis. The thesis work has not been submitted for a degree or professional qualification to any other university or institution. I declare that this thesis is written by myself and is free of plagiarism and of sufficient grammatical clarity to be examined. I confirm that the investigations were conducted in accord with the ethics policies and integrity standards of Nanyang Technological University and that the research data are presented honestly and without prejudice.

7th Aug 2019
. . . .
Date

. . . .
Gan Weiliang

Supervisor Declaration Statement

I have reviewed the content and presentation style of this thesis and declare it of sufficient grammatical clarity to be examined. To the best of my knowledge, the thesis is free of plagiarism and the research and writing are those of the candidate's except as acknowledged in the Author Attribution Statement. I confirm that the investigations were conducted in accord with the ethics policies and integrity standards of Nanyang Technological University and that the research data are presented honestly and without prejudice.

7th Aug 2019
. . . .
Date

. . . .
Assoc. Prof. Lew Wen Siang

Authorship Attribution Statement

This thesis contains material from 2 paper(s) published in the following peer-reviewed journal(s) in which I am listed as an author.

Chapter 4 is published as Weiliang Gan, Sachin Krishnia, and Lew Wen Siang, "Efficient in-line skyrmion injection method for synthetic antiferromagnetic systems", New Journal of Physics, 20,013029 (2018).

The contributions of the co-authors are as follows:

- I proposed the idea and designed the micromagnetic model.
- Sachin Krishnia and I performed the micromagnetic simulations on Mumax3.
- I analyzed the data using MATLAB.
- Sachin Krishnia and I discussed the results
- Prof. Lew Wen Siang supervised the study.
- All authors contributed to the discussion and preparation of the manuscript.

Chapter 5 is published as Wang Xuan*, Weiliang Gan*, Jose Chan Martinez, Tan Funan, M. B. A. Jalil and, Lew Wen Siang, "Efficient skyrmion transport mediated by voltage-controlled magnetic anisotropy gradient", Nanoscale, 10, 733-740 (2018), DOI: 10.1039/C7NR06482A

The contributions of the co-authors are as follows:

- I proposed the idea and designed the micromagnetic simulations on Mumax3.
- Jose Chan Martinez and M. B. A. Jalil formulated the mathematical framework
- Wang Xuan performed the micromagnetic simulations
- Wang Xuan, Tan Funan and I analyzed the data
- All authors contributed to the discussion and preparation of the manuscript.

7th Aug 2019

. . . .

Date

. . . .

Gan Weiliang

Abstract

Magnetic skyrmions are nanoscopic magnetization textures that have intrigued the spintronics community for more than a decade now due to their potential as a next-generation information carrier. Their highly sought-after characteristics, such as high current-induced transport speeds, small sizes, and topological stability allows them to simultaneously fulfil the function of both random-access memory and high capacity storage media. However, several challenges should first be addressed, such as the skyrmion Hall effect (SkHE), skyrmion transport efficiency, and the lack of suitable injection methods.

In this thesis, the dynamics of skyrmions under the influence of spin-orbit torques and magnetostatic field gradients were investigated by using a combination of theoretical and numerical modelling methods. Our model on spin-orbit torque reveals that the skyrmion speed scales linearly with its size, leading to a tradeoff between skyrmion density and speed. A mechanism exploiting the transverse repulsive forces from the nanowire edges was revealed, where the skyrmion speed was shown to be increased many times. A similar mechanism was found in antiferromagnetically-coupled skyrmions, that allows the negation of the SkHE while passively increasing their speed. Furthermore, the difficulty in nucleating these type skyrmions was also tackled; a combination of DMI-induced edge tilting and spin-orbit torque allows single skyrmions to be injected on-demand efficiently.

For the development of energy-efficient skyrmion memory devices, a model was developed to describe the skyrmion motion under a voltage-controlled magnetic anisotropy (VCMA) gradient. As no electric currents are required, the VCMA-based devices consume several orders of magnitude lesser power. A VCMA-based device architecture was proposed using multiplexed discrete gate electrodes. A maximum speed of 70 ms^{-1} was achieved, similar to current-induced speeds. However, VCMA-based devices are clear winners in terms of design flexibility; a recirculating skyrmion track was demonstrated, where skyrmions could be shifted and cycled in a loop. To overcome the SkHE in such devices, a transverse driving scheme was devised such that the net skyrmion motion is directed parallel to the device axis. Finally, a hybrid drive combining both the transverse and longitudinal scheme was also demonstrated, resulting in high velocity skyrmion motion with low SkHE. While only a few types of skyrmion devices were discussed, the model developed in this thesis serves as a platform for the design of novel VMCA devices.

Acknowledgements

This thesis was completed and could only be completed with the help and support of the many peers, superiors, friends and family members. My supervisor Prof. Lew Wen Siang played a key role by guiding me through my PhD journey. I truly appreciate the numerous advice that he has given me on career development and also words of wisdom that has shaped my life. I would like to thank my first mentor, Dr. Chandrasekhar Murapakar. In my undergraduate years, he had provided me with a good direction to get started in spintronics. Only with his mentorship, I have achieved my first milestones in spintronics research and developed the confidence needed for my PhD studies. Dr. Indra Purnama imparted to me a wealth of analytical skills and developed my spintronics “instincts”. The latter was what I relied on to conceive many of the ideas presented in this thesis.

Funan is always helpful with experiments and his light-heartedness and optimism made the long hours enjoyable. Waicheung inspired me with his perseverance as he built the high-temperature FMR system from ground up. Gerard was the go-to person for any technical assistance. Despite his busy work schedule, he has never shunned his responsibilities. Dr. Sachin, Dr. Pankaj, Dr. Ramu, and Dr. Feilong were always keen to assist me in experimental work and were forthcoming in sharing their ideas. Conversations with them on various topics in spintronics were always enlightening and appreciated.

My peers Grayson and Xu Zhan are experts in RF instruments and have broadened my technical knowledge. Calvin is always helpful, and it was with his help with sample fabrication and characterization that many of my experiments could be conducted. Wang Xuan and Tian Li are hardworking individuals, constantly pushing me to work harder in order to keep up. Without the comradery and strong support within the spintronics group, I would not have developed such a keen interest in spintronics. The spintronics laboratory in NTU was no doubt the place I had spent most of life in the past years. And it is my peers and colleagues who had made the environment so enjoyable. Thanks, everyone!

I would also like to thank all collaborators: Prof. Mansoor Bin Abdul Jalil, Dr. Jose Chan Martinez, Prof. Cao Jiangwei, Prof. Ma Fusheng, Prof. Mathias Klauei, Mariia Filianina, Sven Heinz, and all staffs and members of the Klauei lab at JGU, Mainz.

On this arduous journey, it was easy to take for granted the close support of my family members. My parents were kind and understanding in their support, always putting my needs ahead of theirs. I am truly grateful for their unwavering support.

Thank you, Ann, for all your love.

Table of Contents

Chapter 1 Introduction

Skyrmions are topological objects that exist in a non-linear field theory for interacting pions first proposed by particle physicist Tony Skyrme in 1961.[1] Although superseded by quantum field theory, the skyrmion has found relevance in other fields of physics such as in quantum Hall magnets,[2] Bose-Einstein condensates,[3] and most recently, magnetism. The magnetic skyrmion, which is the subject of the thesis, has garnered significant interest in the spintronics community due to its potential to be an information carrier to revolutionize data storage and manipulation. In this chapter, a brief history of magnetic skyrmions lasting the past decade will be presented. Following which, the practicality and advantages of magnetic skyrmions in memory and logic applications will be discussed.

1.1 Magnetic skyrmion

Magnetic skyrmions are swirling particle-like magnetization textures most commonly found in ferromagnetic materials. The skyrmion profile can then be described as a gradual magnetization switch from up (down) to down (up) in the radial direction. In any substrate, the skyrmion phase q which describes the chirality is locked. On the other hand, the skyrmion polarity p describes the skyrmion outer magnetization and is determined by the initial magnetization of the substrate. In Figure 1-1, all the possible skyrmion configurations of the Bloch type are illustrated.

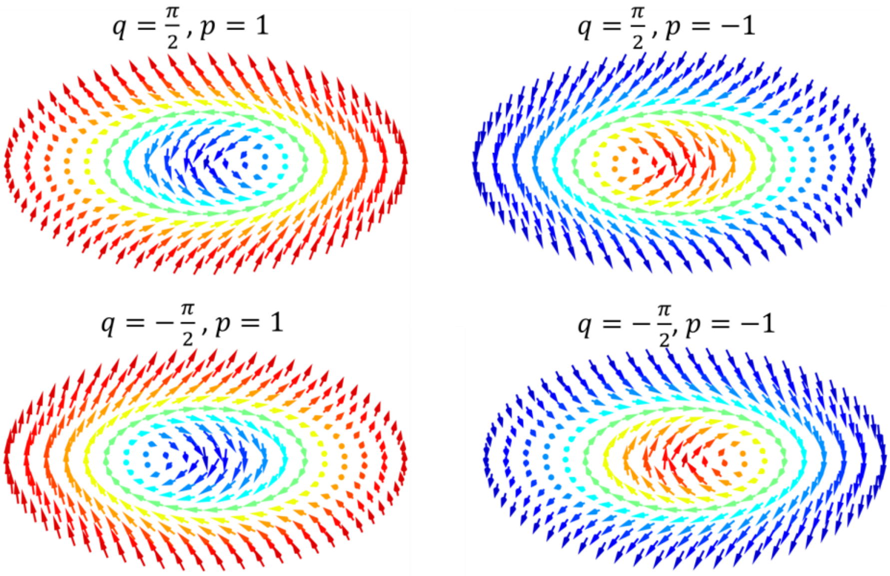

Figure 1-1 Magnetization vectors of different magnetic skyrmions in a 2D ferromagnetic system are represented by the individual arrows with their colours representing the out-of-plane components

Given the radial symmetry of the skyrmion profile, the skyrmion magnetization can be described by polar coordinates with the following set of equations:

$$\mathbf{M}(r,\phi)=\begin{pmatrix}\cos(\phi+q)\ \operatorname{sech}\left(\frac{r-c}{R}\right)\\ \sin(\phi+q)\ \operatorname{sech}\left(\frac{r-c}{R}\right)\\ p\tanh\left(\frac{r-c}{R}\right)\end{pmatrix}M_s, \qquad \text{Equation 1-1}$$

where R and c describe the skyrmion gradient and radius, respectively. The two parameters are mostly determined by material parameters such as exchange stiffness and effective magnetic anisotropy but can also be modified by externally applied magnetic fields.

Although magnetic skyrmions have been theorized to exist in non-centrosymmetric crystals decades ago, the first experimental observation of magnetic skyrmions was only in 2009. The team led by S. Mühlbauer performed neutron scattering experiments on a cubic B20 MnSi crystal.^{4} The lack of inversion symmetry in the crystal lattice gives rise to a three-site spin-orbit coupling that is also known as the Dzyaloshinskii-Moriya interaction (DMI). This chiral spin-orbit coupling results in adjacent magnetization preferring to be perpendicularly oriented to each other. However, such an arrangement is unfavourable for the ferromagnetic exchange interaction. The interplay between the chiral spin-orbit coupling and the ferromagnetic exchange then results in a gradually canting magnetization as shown in Figure 1-2. Below the Curie temperature, the magnetic ordering of MnSi at remanence is that of the helical phase where the magnetization winds around the propagation direction. Under an applied magnetic field, a conical phase develops where the magnetization also tilts in the direction of the magnetic field.

Figure 1-2 A 1D chain of spins is shown to visualize the conical and helical states. Each spin shown would have corresponded to a plane of spins in a bulk crystal. (a) The magnetization in the helical state winds along the propagation vector, resulting in net-zero magnetization. (b) The magnetization in the conical state sweeps between the up (red) and down (blue) directions, resulting in a net magnetization in the direction of the applied magnetic field.

Applying a stronger magnetic field to MnSi causes the cone angle of the conical phase to decrease, eventually saturating and becoming field-polarized. The other factor determining the magnetic phase is temperature. Due to the weak exchange interaction, the Curie temperature of MnSi is 29 K. The phase diagram of MnSi as a function of temperature and applied magnetic field is shown in Figure 1-3a. Close to the Curie temperature, a skyrmion phase emerges. The development of a skyrmion phase close to the Curie temperature can be attributed to the weakening of the exchange interaction which encourages the formation of longer-ranged magnetization textures. As the DMI becomes the dominant interaction, short-range magnetization textures such as the skyrmion crystal becoming more favourable.

In Figure 1-3b, the neutron scattering diffraction pattern at the A-phase is shown. A pattern of six-fold symmetry is clearly visible and indicates the presence of a hexagonal skyrmion lattice phase. Although direct evidence of the hexagonal skyrmion lattice was not shown in this pioneering work, many subsequent works have imaged the skyrmion lattice in real space.[5-14] In Figure 1-3c, a rendered magnetization map of the skyrmion is shown with hexagonal lattice is highlighted. Due to the interplay between the minimization of DMI energy by nucleating more skyrmions and the inter-skyrmion repulsion, a close-packed hexagonal lattice is formed.

A major milestone for skyrmionics was the experimental demonstration of the writing and deletion of single skyrmions by Niklas Romming and team.[15] The experiments were performed at 4.2 K on a Pd/Fe bilayer and under a magnetic field of between 1 to 2 T. A spin-polarized scanning tunneling microscope (SP-STM) was used to observe the skyrmions. The magnetic phase of the Pd/Fe bilayer is similar to that of MnSi, where at zero applied external magnetic field, the dominant magnetic ordering is that of a helical phase in Figure 1-2a. Applying increasing magnetic field reduces the energy costs for skyrmion formation and the skyrmion population gradually increases. At 1.4 T, a pure skyrmion state is obtained. Applying an even greater magnetic field results in skyrmions gradually annihilating, with no skyrmions left at the field-polarized ferromagnetic phase at 2 T.

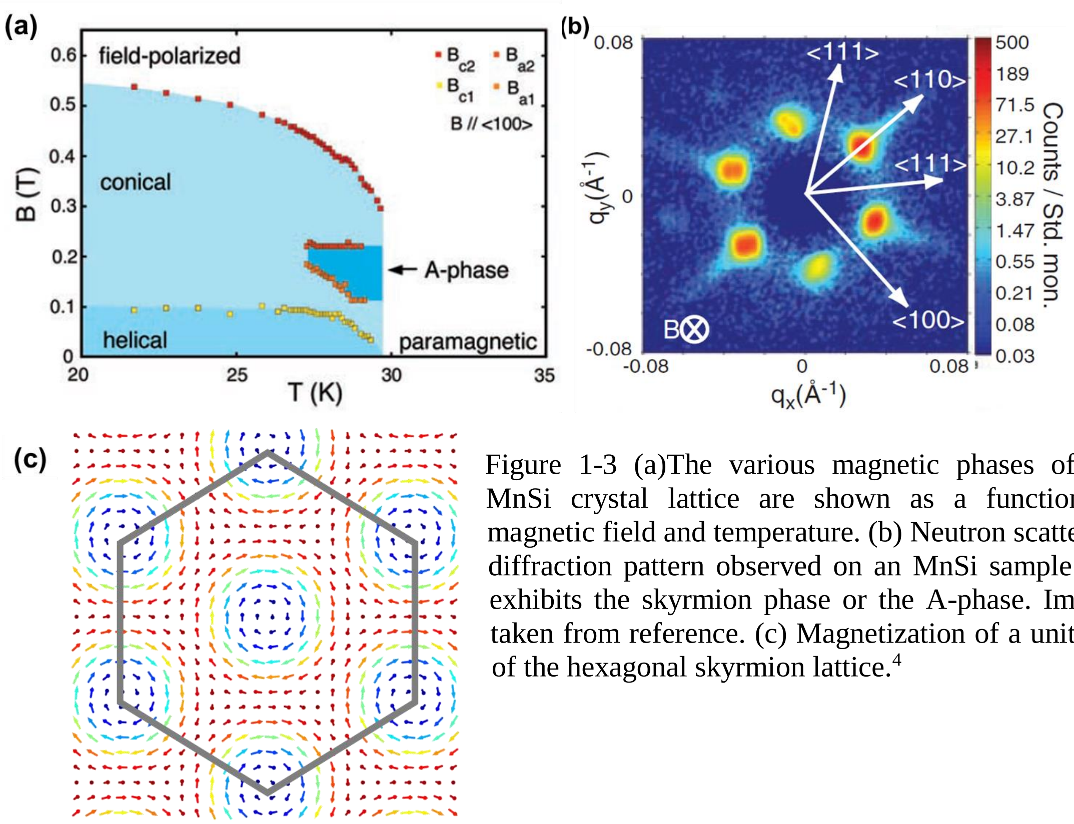

Figure 1-3 (a)The various magnetic phases of the MnSi crystal lattice are shown as a function of magnetic field and temperature. (b) Neutron scattering diffraction pattern observed on an MnSi sample that exhibits the skyrmion phase or the A-phase. Images taken from reference. (c) Magnetization of a unit cell of the hexagonal skyrmion lattice.[4]

The injected spin currents from the SP-STM have a chance to inject or annihilate skyrmions depending on the current amplitude. Figure 1-4(a) shows the potential energy for the skyrmion phase and the ferromagnetic phase. The model developed by Romming explains that each local area has a switching outcome (success or failure) that depends on the potential energy. By increasing the magnetic field, the energy cost for the ferromagnetic phase is reduced and thus it is more likely to annihilate skyrmions. Operating at a field of 1.8 T, Figure 1-4b-c shows a differential SP-STM image before and after injecting spin-polarized currents at a few local areas. An increase in the skyrmion population is apparent, thus demonstrating the ability to ‘write’ skyrmions. By applying a lower magnetic field, skyrmion injection is performed.

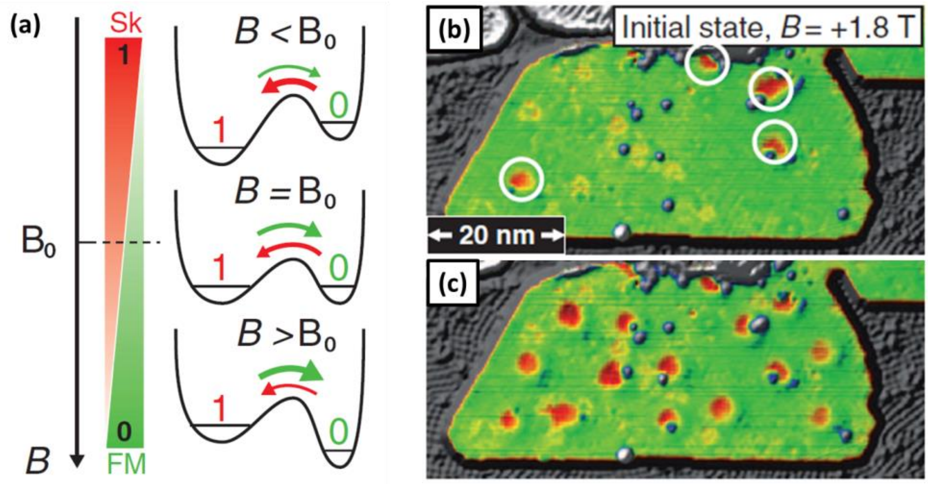

Figure 1-4 (a) Magnetic field dependence of the potential energy for the skyrmion (Sk) and ferromagnetic (FM) phase. Increasing the magnetic field deepens the potential well for the ferromagnetic phase and is useful for deleting skyrmions.[15] (b) Differential spin-polarized scanning tunnelling microscopy images before and (c) after local injection of large spin currents. A much lower spin current is used for imaging to preserve the magnetization states.[15]

The work by N. Romming is also interesting in another sense; a metallic bilayer was used, instead of the bulk crystals used by S. Mühlbauer. The work demonstrates that skyrmion formation is supported in 2D materials. Importantly, it has also shown that a large DMI can be present in an ultra-thin ferromagnetic film. To compensate for the lack of inversion asymmetry in the crystal structure of ferromagnetic elements such as Co, Ni, and Fe, the interface can be exploited. By having a heavy metal layer only on one side of the ferromagnet, a net DMI can be produced as shown in Figure 1-5. The DMI is a three-site spin-orbit coupling phenomenon, where the coupling between spins $\mathbf{S}_1$ and $\mathbf{S}_2$ is mediated by the heavy metal atom. In the absence of a symmetric top interface, the spins experience a net DMI vector $\mathbf{D}_{12}$ in the in-plane direction. However, it is also known that nominally symmetric materials can still exhibit a net DMI due to the inherent differences in the interfaces due to material growth processes.[16] Heavy metals have an enhanced spin-orbit coupling strength due to their large atomic numbers and are thus the favoured for interfacing with the ferromagnet.[17, 18]

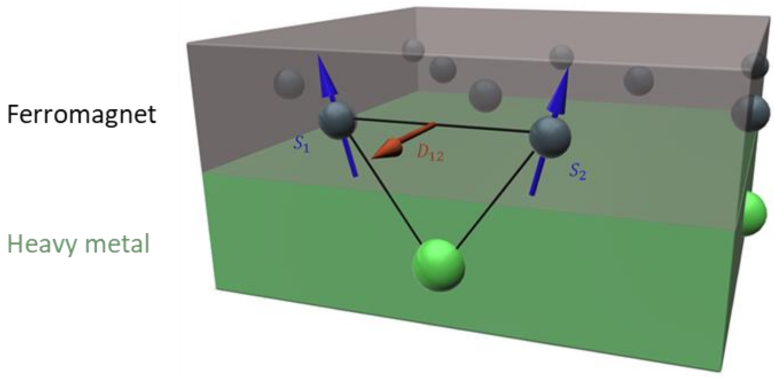

Figure 1-5 Schematic representation of the three-site spin-orbit coupling at ferromagnet/heavy metal interfaces which gives rise to the interfacial DMI.

The interfacial DMI acting on spins $\mathbf{S}_1$ and $\mathbf{S}_2$ and its Hamiltonian is expressed as:

$$H_{DM} = -\mathbf{D}_{12} \cdot \left(\mathbf{S}_1 \times \mathbf{S}_2 \right) \qquad \text{Equation 1-2}$$

Compared to the bulk DMI in crystals with no inversion symmetry, the interfacial DMI most notably cant adjacent spins in the same direction as their separation vector. This results in the formation of another type of skyrmion, the radial-type skyrmion and also commonly known as Néel-type or hedgehog type. The names give a strong hint of their configuration, that the spins cant outwards from the skyrmion core, as shown in Figure 1-6. This is in contrast with what is shown in Figure 1-1 where the spins spiral around the skyrmion core instead. To model the magnetization profile of the Néel type skyrmions, the phase φ in Equation 1-1 is set to either 0 or $\pm\pi$. While the change of skyrmion type from Bloch to Néel type seems trivial, we shall see in the next chapter that the skyrmion's magnetization profile has important implications on skyrmion transport.

The next major breakthrough in skyrmionics occurred in 2016 with the first observation of electric current-induced skyrmion transport by Woo Seunghoon and team.[19] The current-induced propagation of skyrmions due to spin transfer torque or spin-orbit torques has been predicted in micromagnetics and would be a necessity if magnetic skyrmions are to be used for memory or logic applications. Using magnetic transmission soft X-ray microscopy (MTXM), the team was able to observe a translation of skyrmions under applied currents in $[Pt/Co/Ta]_{15}$ and $[Pt/CoFeB/MgO]_{15}$ where the subscript numbers represent the number of repeats of the multilayer thin films.

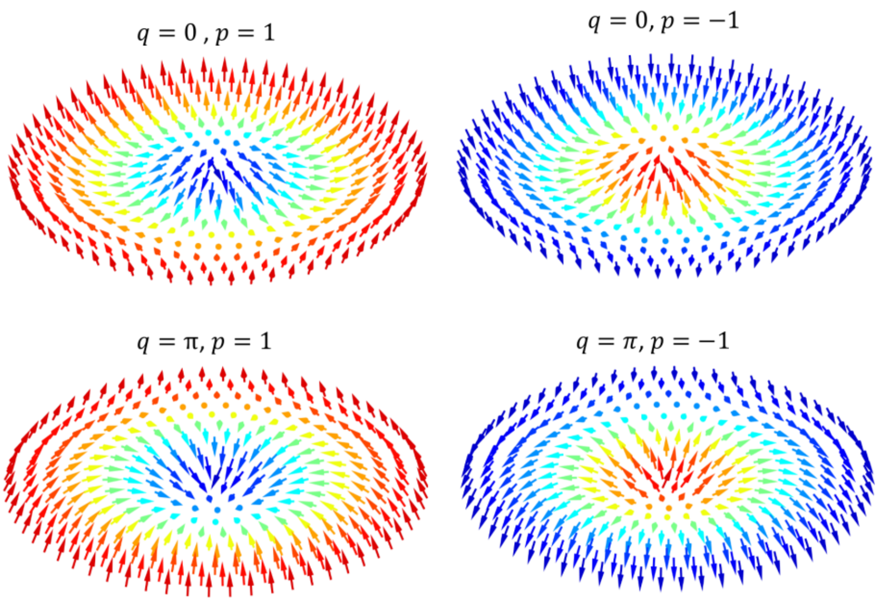

Figure 1-6 Magnetization vectors of different Néel magnetic skyrmions in a 2D ferromagnetic system are represented by the individual arrows with their colours representing the out-of-plane components.

Néel type skyrmions were nucleated by utilizing the strong interfacial DMI found at the Pt/Co interface.[20-27] Applying a current pulse, the nucleated skyrmions were observed to translate along the nanowire. While the MTXM was not time-resolved, the skyrmion propagation velocity due to the applied current pulse can be determined due to the finite current pulse duration. In this case, the current pulses were of 20 ns. In the Pt/Co/Ta sample and at a current density of 3.5×10^{11} Am^{-2}, speeds of about 40 ms^{-1} were observed. Although the speed of 40 ms^{-1} was already respectable, it was suspected that the polycrystalline structure of the sputtered Pt/Co would have caused grain boundaries and pinned the skyrmions.[28]

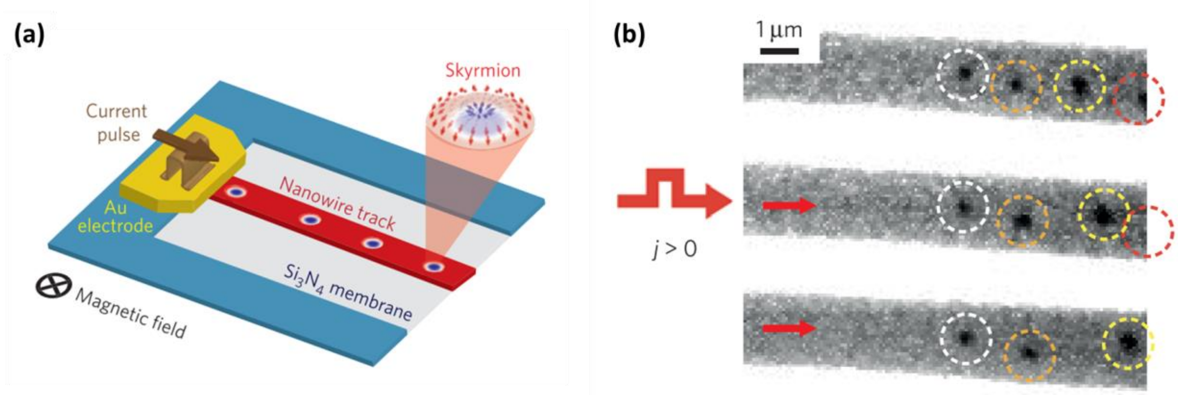

Figure 1-7 (a) Experimental set up for the magnetic transmission soft X-ray microscopy for the observation of current-induced skyrmion transport.[19] (b) MTXM images obtained after the application of current pulses. Skyrmions were observed to be displaced rightwards, in the direction of the applied current.[19]

To increase the skyrmion transport speed, the team also measured the skyrmion speed in $[\mathrm{Pt/CoFeB/MgO}]_{15}$ stacks. Due to the amorphous nature of MgO, there would be fewer grain boundaries in the magnetic CoFeB layer. The measured speeds in the Pt/CoFeB/MgO layers were found to be comparable to that of the Pt/Co/Ta. However, when taking the spin Hall angles into consideration, the Pt/CoFeB/Ta would have a speed that is three times higher at the same current density. The spin Hall angle is a coefficient that quantifies the conversion efficiency from charge current into spin current due to the spin Hall effect.[29-35] A detailed overview of the spin Hall effect will be given in Chapter 2. Important to note here is that the spin Hall effect was predicted to be highly efficient in driving skyrmions. The team further confirmed that the spin Hall effect was the dominant driving force as the skyrmions moved in the direction of the applied current density. If the skyrmions were to be driven by the spin transfer torque, the propagation direction would be against the current direction. The work by Woo not only demonstrated the first current-induced skyrmion motion but also proved that the spin Hall effect is the dominant driving force, many times stronger than the spin transfer torque.

Although there exists a multitude of other significant and valuable works on skyrmions outside of the discussed works, the discussion here has covered the major milestones in the decade-long modern history of skyrmions. Next, the unique properties of magnetic skyrmions will be reviewed.

Skyrmions have good stability due to their topologically protected magnetization configuration. The topological protection is a result of the locked chirality granted by the presence of a DMI. In Figure 1-8, the benefits of having a locked chirality are demonstrated. In the initial (rest) state, each chain of spins has two domain walls. The only difference is that both the domain walls in the top chain have a right-handed chirality, while the bottom chain two domain walls of different chiralities. At rest, and under no perturbations, both chains remain unchanged. However, as soon as a magnetic field in the down direction is applied, the domain walls would converge on the centre. The shrinking of the central domain is a result of the minimization of Zeeman energy given by $E_{Zeeman} = \mu_0 \mathbf{M} \cdot \mathbf{H}$, where $\mathbf{M}$ is the magnetization vector and $\mathbf{H}$ is the applied magnetic field.

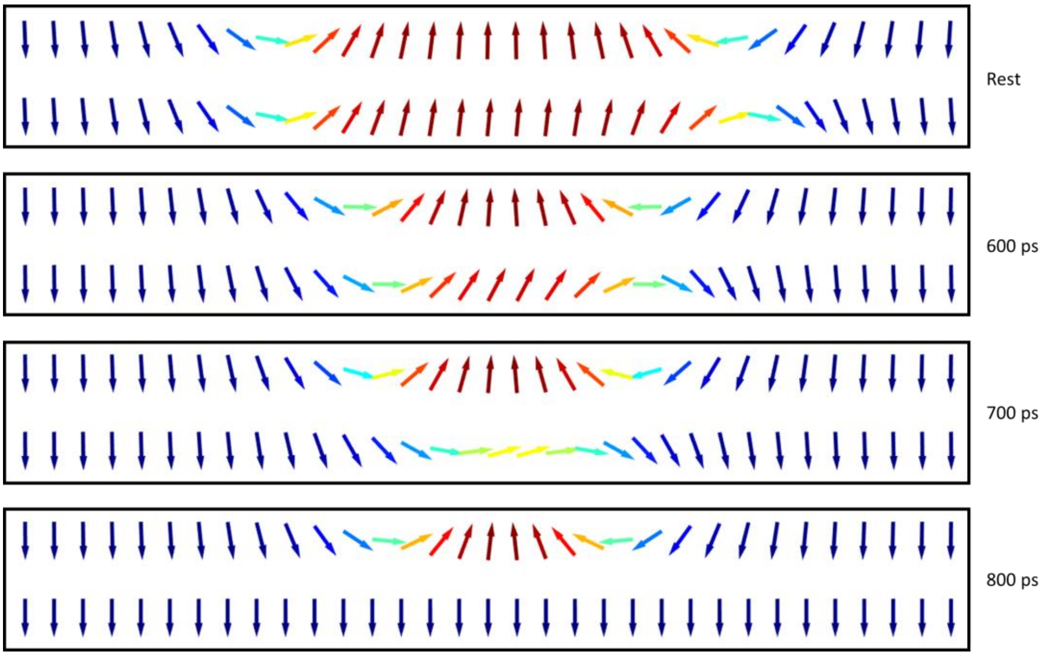

Figure 1-8 Magnetization vectors of a chain of spins at different times after the application of a 0.2 T magnetic field was applied. In each frame, the top and bottom spins differ only in their initial magnetization. The magnetization vectors were calculated with micromagnetic simulations.

At 600 ps, the domain walls are almost in contact. At this time, the first differences appear; the centre domain on the top chiral chain has magnetization mostly pointing up while in the bottom chain, the centre domain is clearly canted towards the right. In the next moment, both domain walls in the bottom chain are merged and quickly annihilated. Due to the lack of topological protection in non-chiral magnetization, the magnetization is easily perturbed and annihilated even in the presence of the small disturbances. On the other hand, the chiral pair of domain walls survives until the applied magnetic field reaches 0.4 T.

The topological protection can be understood from the cant direction induced by the inward pressure. In the non-protected case, both domain walls cant in the same direction, leading to a coherent rotation of the centre domain wall, after which the two side domains are allowed to merge. However, the cant directions in the topologically protected chain oppose each other, maintaining an upright direction despite the strong inward pressure. With the centre domain still upright, the side domains cannot merge. When the perturbation is removed, the centre domain can then again relax into its rest state. Such resilience will prove to be an important asset for memory applications.

Due to the skyrmion's topological attributes, it can be described by a topological charge.[36] In a two dimensional space, it reads:

$$Q = \frac{1}{4\pi}\int d^2\mathbf{r}\cdot\mathbf{m}(\mathbf{r})\cdot\left(\partial_x\mathbf{m}(\mathbf{r})\times\partial_y\mathbf{m}(\mathbf{r})\right) \qquad \text{Equation 1-3}$$

The topological charge can be thought of as the number of times the magnetization $\mathbf{m}(\mathbf{r})$ winds around across the space of the two cartesian coordinates x and y. The topological charge is an integer of ± 1 for all types of skyrmions. In practical applications, the topological charge is important as the sign ($\pm$) determines the direction of skyrmion motion under the influence of a spin Hall torque. The topological charge of a skyrmion is equal to its polarity ($Q = p$).[37, 38] However, theoretical predictions and recent experiments have found the existence of antiskyrmions with opposite topological charge and polarity ($Q = -p$).[39, 40] Such skyrmions consists of a mix of Bloch and Néel characteristics, as shown in Figure 1-9.

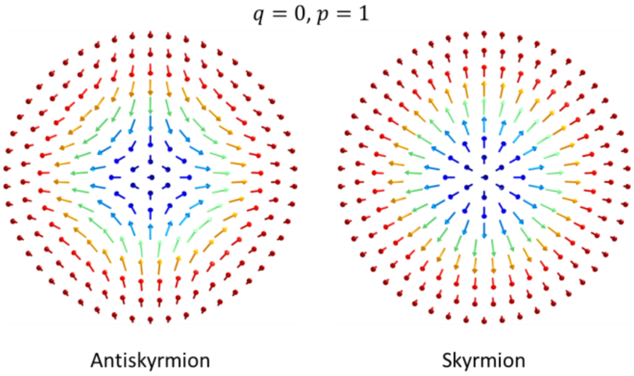

Figure 1-9 Top down view of the magnetization configuration of antiskyrmions and skyrmion.

Besides skyrmions, there exists a wide range of other topological magnetization textures, such as the meron (+0.5), antimeron (-0.5), and bimeron (+1).[41, 42] Even within the skyrmion family there exists the biskyrmion state which can be described as two bound skyrmions with overlapping magnetization.[43]

The second characteristic is that the skyrmions can be driven efficiently by magnetostatic energy gradients,[9, 44-51] by spin transfer torques,[11, 52-59] and by spin Hall torques. This is enabled by the fact that the skyrmion is particle-like and is translationally invariant on a 2D surface. Therefore, they are not easily pinned by defects on the two dimensions that they reside in. Faced with a defect, a skyrmion can simply skirt around as shown in Figure 1-10. Although the ability may seem trivial, domain walls in nanowires are often pinned by defects in the nanowire geometry. Domain walls are translationally invariant in one dimension and thus must be bounded by two other physical dimensions. The extra points of contact with the nanowire wall cause pinning as current fabrication processes inevitably result in imperfect edges. Even nanometer-sized defects can produce a significant pinning effect.

Figure 1-10 Trajectory (white dotted line) of a skyrmion moving past a barrier. The skyrmion deflects lightly to avoid the pinning site (shaded triangle).[54]

1.2 Skyrmions for memory applications

Memory devices are essential for computer operations as they store the information for both immediate use and future use in a computer. In most modern computing architectures, different types of memory devices have to be used in tandem to leverage on the strengths and overcome the shortcomings of each memory type. A memory hierarchy is shown in Figure 1-11, where at the top of the hierarchy, the fastest but also smallest capacity are present. These are usually static random-access memory (SRAM) that are very expensive to produce and are of relatively low density.[60] When the processing units require information not contained within the cache memory, a copy process is required to retrieve the information from the next level, the main memory. Up till the main memory, the data storage mediums are considered volatile, where a small amount of power is required to preserve the information. The disk storage then functions as the non-volatile memory, allowing for long-term information storage. Although the most dominant form of long-term storage currently, hard disk drives have to spin the disk platters mechanically which causes a significant latency.

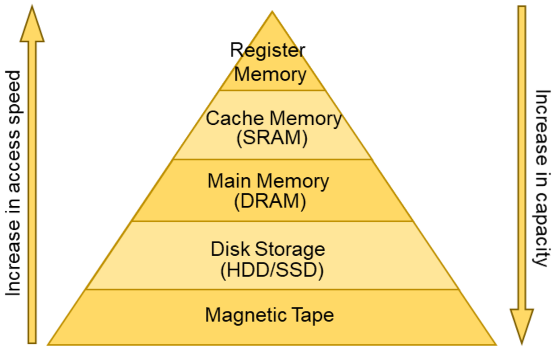

Figure 1-11 Illustration of the memory hierarchy. The fastest and most important, and most scarce memory type reside at the top of the pyramid. Going down the pyramid, the capacity is increased at the cost of reduced access speeds.

The memory hierarchy was designed to leverage the strengths of each type of memory, however, it also incurs significant penalties associated with data transfers between different types of memory. Furthermore, the volatility of the faster memory types also causes computers to be susceptible to sudden power losses. To resolve the aforementioned drawbacks, the concept of a universal memory device is proposed. Universal memories should possess the positive characteristics of every memory type in the hierarchy; the speed and read-write endurance of SRAM and DRAM, and the non-volatility and low cost of hard disk drives. Owing to their ease of manipulation, nanoscale sizes, and high stability, magnetic skyrmions are prime candidates for universal memories. In this section, we will review the proposed skyrmion racetrack memory architecture and discuss how the read and write operations can be achieved.

The idea of a skyrmion racetrack was first proposed in 2013 by Sampaio,[54] as an upgrade over the domain wall racetrack memory proposed by S. Parkin.[61, 62] Instead of storing the information as domains, the skyrmion racetrack utilizes skyrmions.[45, 63-67] In Figure 1-12, the main processes in a skyrmion racetrack memory are illustrated. In the first phase, the skyrmions have to be created or injected into the magnetic wire. Then, by applying a spin current, a magnetic force is applied on the skyrmions which propagate it in either direction, depending on the spin current direction. Other than using a spin current, several works have demonstrated that it is possible to use magnetostatic energy gradients or thermal gradients to drive the skyrmions.[48-50] To read the encoded information, the skyrmion chain is moved across a magnetoresistive read head and a sequential readout is performed simultaneously. Magnetic tunnel junctions (MTJs) are preferred for this task as they exhibit large magnetoresistance changes of up to a few hundred percent.[68-72] The skyrmion racetrack is reminiscent of the now obsoleted delay line memory, where acoustic pulses in a metallic wire are recirculated indefinitely at a frequency of about one MHz .[73, 74]

The first experimental electrical detection of skyrmions was achieved by Du *et. al.* in 2014. By measuring the magnetoresistance of the MnSi substrate as a function of the magnetic field, they were able to observe rapid changes in magnetoresistance that correspond to the skyrmion states.[75] In 2015, Dax M. Crum *et. al.* explored with first principles and determined that the electrical readout of single skyrmions in a current perpendicular to plane geometry and based on tunnelling non-collinear magnetoresistance (NCMR) effect could be achieved.[68] Christian Hanneken *et. al.* experimentally demonstrated the detection of skyrmions using the NCMR effect which arises due to the spin-mixing magnetoresistance.[76] As NCMR is dependent only on the non-collinearity of the local magnetization, it is not affected by material choice, while MTJs are very sensitive to the crystallinity and interface conditions.[77] Kubetza et. al. later analyzed in detail the impact of local properties of the skyrmions on the detected peak energy.[70]

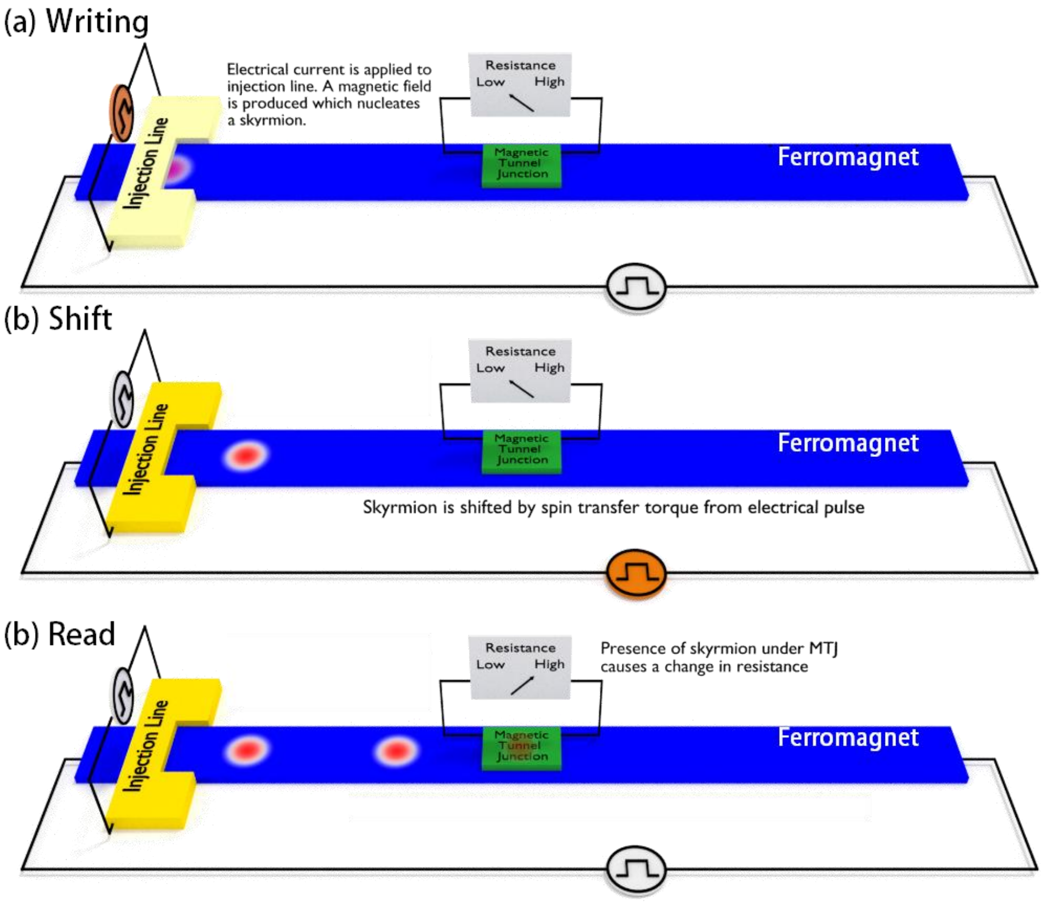

Figure 1-12 Schematic diagrams of a skyrmion racetrack at different stages of operation. (a) A current is passed through the injection line, which produces an Oersted field and nucleates a skyrmion. (b) the shift operation is performed by passing an electric current through the nanowire to generate spin currents that move the skyrmions forward. (c) A magnetic tunnel junction is used to read the presence and absence of a skyrmion.

While NCMR may seem to be a strong candidate for reading skyrmions, it has only been demonstrated using the scanning tunnelling microscope tip. However, an on-device method is necessary for any commercial memory applications. Maccariello *et. al.* has recently demonstrated the reading of single skyrmions by using the anomalous Hall effect.[78] The experiment setup is shown in Figure 1-13(a), where magnetic force microscopy was used to observe the skyrmions while the anomalous Hall resistance ρ_{xy} was measured. The anomalous Hall effect is directly proportionate to the perpendicular magnetization state of the ferromagnet. When skyrmions are present in the cross region, also known as the Hall bar, the transverse voltage (V_y) changes. In Figure 1-13(b), a clear trend between the number of skyrmions and the change in anomalous Hall resistance is observed. The observation can potentially be useful for memristor type devices that are demanded by neuromorphic computing.

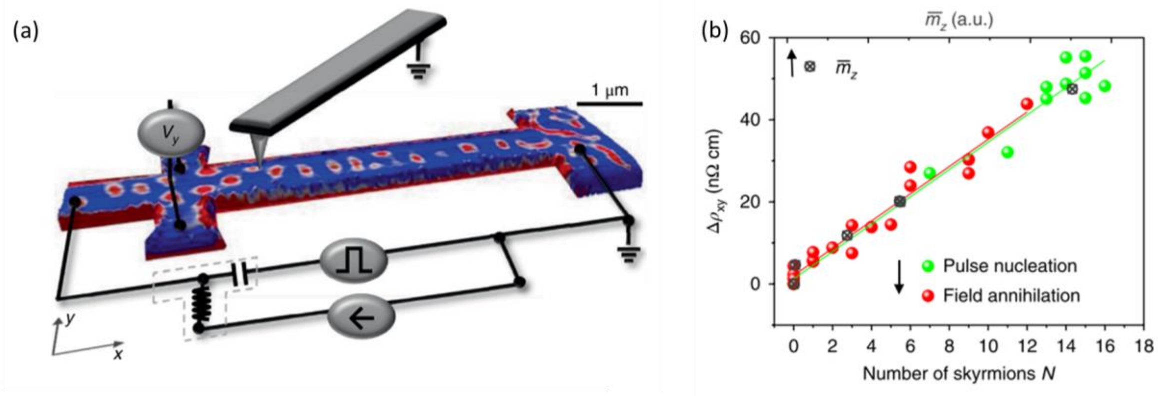

Figure 1-13 (a) Schematic illustration of the setup for magnetic force microscopy and electrical readout of the anomalous Hall voltage (V_y). [78] (b) The measured anomalous Hall voltage as a function of the number of skyrmions.[78]

The other great challenge lies in the reliable injection of skyrmions. In 2014, Zhou Yan *et. al.* proposed a mechanism for the bidirectional conversion between skyrmions and domain walls in a racetrack memory architecture. The reversible conversion between the two types of topological objects allows skyrmionic devices to enjoy the advantages of both.[58] This is especially true for the injection process, as domain wall injection methods have been very well studied.[79-81] In 2015, Axel Hoffman *et. al.* demonstrated experimentally a similar concept.[82] By pushing a stripe domain through a micro-constriction, the chiral stripes were converted into skyrmions, as shown in Figure 1-14. In 2017, Felix Büttner demonstrated a deterministic electrical injection of skyrmions. Using a constriction, the local current density is concentrated which results in a strong spin-orbit torque that can switch the magnetization.[83]

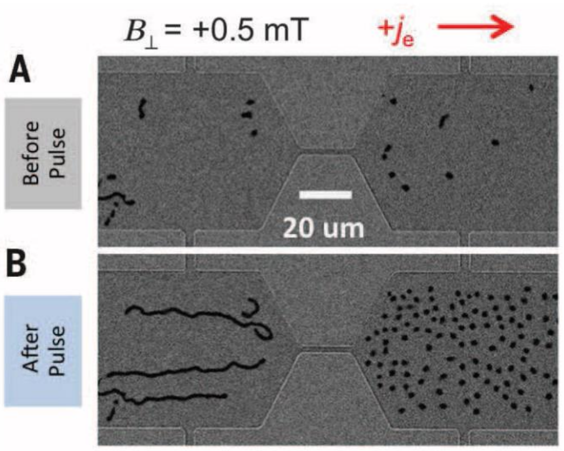

Figure 1-14 Differential Kerr images demonstrating the conversion between chiral stripes and skyrmions. Upon applying a current density j_e, the right side of the microwire becomes filled with skyrmions.[82]

Due to their high current-induced transport speeds, skyrmions can be shifted to the read/write heads without requiring any moving parts and enabling high access speeds and high read-write endurance. Their atomic- to nano-scale sizes enable skyrmion memory devices to have data densities similar to that of hard disk drives. Their stability grants them the ability to store data in a non-volatile manner.[13, 84-92] Despite the apparent benefits of a skyrmion racetrack memory, there exist significant challenges in the integration of various technologies required for the skyrmion racetrack memory. Thus, a fully functioning prototype remains elusive.

With the recent surge of interest in artificial intelligence, various ideas have been proposed to employ skyrmions for neuromorphic computing.[93-98] Li Sai *et. al.* conceived of a racetrack-like device with a magnetic anisotropy gradient that uses skyrmions to function as a leaky-integrate-fire spiking neuron.[94] By applying current pulses, the skyrmion is propagated forward along the track. However, when no current is applied, the skyrmion slips back due to the anisotropy gradient. When sufficient current spikes are supplied, the skyrmion eventually reaches the detection unit. Chen Xing et. al. took a different approach to recreate the “leakiness”; the racetrack was tapered and causes a gradient in magnetostatic energy. George Bourianoff et. al. proposed that a skyrmion fabric, which is a wider microwire containing tens or potentially hundreds of skyrmions in a disordered state, can be used to implement Echo State recognition and prediction.[95] The mechanism relies on the formation of differential current flows resulting from the anisotropic magnetoresistance.

1.3 Skyrmion Hall Effect

Despite the many positive characteristics of skyrmions, they exhibit a crippling behaviour known as the skyrmion Hall effect (SkHE).[67, 99-101] When driven by an excitation, regardless of origin, the skyrmion velocity direction deviates from the driving excitation. The phenomenon is a consequence of magnetization precession which results in a gyrotropic force. The Thiele equation which describes the skyrmion equilibrium motion reads:[52, 102]

$$0 = \mathbf{G} \times \mathbf{v} + D(\alpha \mathbf{v}) \qquad \text{Equation 1-4}$$

The first term describes the gyrotropic force, with $G = 4\pi Q\hat{z}$ where Q is the topological charge given by Equation 1-3. The second term describes the dissipative forces, with D being the dissipative dyadic. In general, the gyrotropic force acts transverse to the skyrmion velocity, which has also led to some calling it the Magnus force.

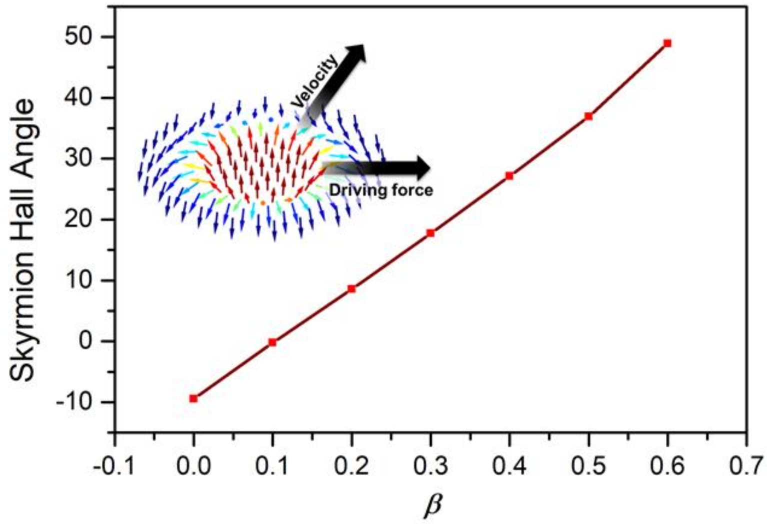

Figure 1-15 Plot of skyrmion Hall angle versus degree of non-adiabaticity of spin current β. A typical value of β is 0.3 which results in almost 20 degrees. Being a material parameter, it is not easy to optimize without compromising other material properties. Figure inset shows the geometry of the SkHE.

The SkHE has become a huge obstacle in skyrmionics due to its role in annihilating skyrmions as they touch the edges. Under a weak driving force, the skyrmions experience an increasingly strong repulsion from the nanowire edge as the skyrmion drifts towards the edge.[66] Eventually, the transverse gyrotropic forces from the nanowire are cancelled by the edge repulsion and the skyrmion moves in a straight line. However, when a stronger driving force is applied, the gyrotropic force can overcome the nanowire edge repulsion and annihilate at the edges. Such a sequence of events is shown in Figure 1-16. As a result, the driving forces for skyrmion is limited and consequently, the maximum translational speed of the skyrmion is reduced.

The SkHE was identified relatively early in skyrmion research and many solutions have been proposed. The first type of solution involves building a magnetostatic barrier on the edge of the nanowire to prevent the skyrmion from touching the edges and annihilating. Indra *et. al.* first proposed the use of thickened curbs on the sides of the nanowire.[103, 104] The thickened curb acts as an extremely strong potential barrier, thus being able to resist the gyrotropic forces from a strong driving force. The magnetostatic field profile is shown in Figure 1-17. Incidentally, the work also discovered that the curbs can compress the skyrmions, resulting in a higher skyrmion density than allowed for in the material. Other similar methods were also explored, such as the modulation of perpendicular magnetic anisotropy,[105-107] or modulation in the DMI,[108] or even by modulating the Gilbert damping.[104]

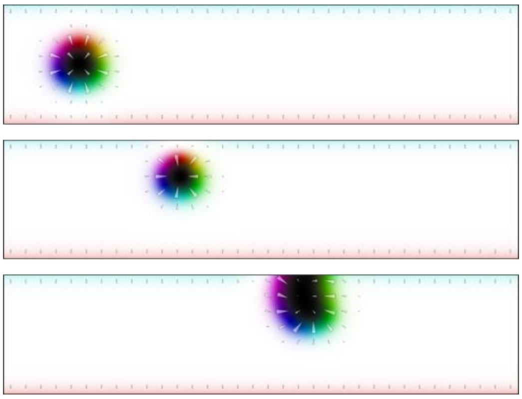

Figure 1-16 Magnetization snapshots at various times. Under a large applied spin torque, the skyrmion Hall effect pushes the skyrmion upwards and eventually leads to annihilation.

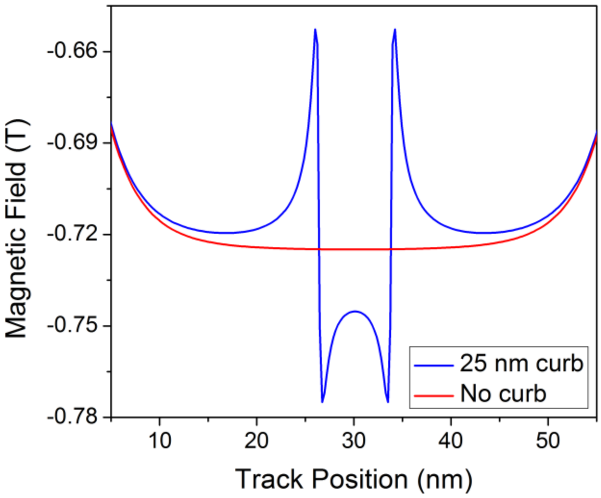

Figure 1-17 Plot of the demagnetizing field that is acting on the nanowire, across the nanowire width. The presence of a curb causes a huge potential well to be formed, trapping the skyrmion.

The other type of SkHE mitigation strategy involves coupling two skyrmions with opposite SkHE. The first concept was shown by Zhang Xichao *et. al.* using a RKKY-type interlayer antiferromagnetic coupling.[100] To achieve antiferromagnetic coupling between two ferromagnetic layers, a thin Ruthenium layer typically 0.4 nm or 0.8 nm,[62] can be inserted to create an antiferromagnetic coupling between the two layers that can reach strengths of 0.7 Tesla.[109] The strong coupling between the two opposite Q skyrmions allow for complete cancellation of the SkHE. Works on this type of SkHE mitigation method have shown that skyrmions speeds of up to 10 km/s can be achieved without annihilation.[50] The disadvantage of this approach is in the loss of choices for the material interfaces, which is important for sustaining a strong DMI and also to create a strong spin Hall current.

Recent trends in skyrmionics are headed towards the use of true antiferromagnetic materials or at least ferrimagnetic materials. The rationale is similar to the use of an interlayer antiferromagnetic coupling. In antiferromagnetic materials, the magnetization can be deconstructed into two spin lattices that have opposite magnetization to each other. As such, the SkHE can also be effectively cancelled out.[110-114] The first experimental observation of ferrimagnetic skyrmions was performed by Woo *et. al.* on GdFeCo films.[115] A later study by Lucas *et. al.* further demonstrated that domain walls can be driven at a km/s on GdCo films,[116] a huge improvement over ferromagnetic domain walls. It is expected that ferrimagnetic skyrmions will benefit from such speed gains.

1.4 Objective of this thesis

The ultimate aim of this thesis is to enable high-performance skyrmion memory devices. Therefore, the individual objectives are designed to improve or aid in the improvement of key performance indicators of the proposed skyrmion racetrack memory architecture such as skyrmion transport speed, skyrmion transport efficiency, skyrmion nucleation efficiency, and the reduction of the skyrmion Hall effect.

1) Develop analytical models for skyrmion dynamics under various forms of excitations such as:
    a. Spin-orbit torques
    b. Magnetostatic energy gradients
2) Demonstrate skyrmion devices that utilizes voltage-controlled magnetic anisotropy for skyrmion transport.
3) Demonstrate an energy-efficient skyrmion injection method for antiferromagnetic devices.

References

1. T. H. R. Skyrme, *Proceedings of the Royal Society of London. Series A. Mathematical and Physical Sciences*, 1961, **260**, 127-138.
2. L. Brey, H. A. Fertig, R. Côté and A. H. MacDonald, *Physical Review Letters*, 1995, **75**, 2562-2565.
3. U. Al Khawaja and H. Stoof, *Nature*, 2001, **411**, 918-920.
4. S. Mühlbauer, B. Binz, F. Jonietz, C. Pfleiderer, A. Rosch, A. Neubauer, R. Georgii and P. Böni, *Science*, 2009, **323**, 915-919.
5. W. Münzer, A. Neubauer, T. Adams, S. Mühlbauer, C. Franz, F. Jonietz, R. Georgii, P. Böni, B. Pedersen, M. Schmidt, A. Rosch and C. Pfleiderer, *Physical Review B*, 2010, **81**.
6. X. Z. Yu, Y. Onose, N. Kanazawa, J. H. Park, J. H. Han, Y. Matsui, N. Nagaosa and Y. Tokura, *Nature*, 2010, **465**, 901-904.
7. S. Heinze, K. von Bergmann, M. Menzel, J. Brede, A. Kubetzka, R. Wiesendanger, G. Bihlmayer and S. Blügel, *Nature Physics*, 2011, **7**, 713-718.
8. X. Z. Yu, N. Kanazawa, Y. Onose, K. Kimoto, W. Z. Zhang, S. Ishiwata, Y. Matsui and Y. Tokura, *Nature materials*, 2011, **10**, 106-109.
9. S. Seki, X. Z. Yu, S. Ishiwata and Y. Tokura, *Science*, 2012, **336**, 198-201.
10. P. Milde, D. Kohler, J. Seidel, L. M. Eng, A. Bauer, A. Chacon, J. Kindervater, S. Muhlbauer, C. Pfleiderer, S. Buhrandt, C. Schutte and A. Rosch, *Science*, 2013, **340**, 1076-1080.
11. X. Z. Yu, N. Kanazawa, W. Z. Zhang, T. Nagai, T. Hara, K. Kimoto, Y. Matsui, Y. Onose and Y. Tokura, *Nature Communications*, 2012, **3**, 988.
12. X. Yu, J. P. DeGrave, Y. Hara, T. Hara, S. Jin and Y. Tokura, *Nano Letters*, 2013, **13**, 3755-3759.
13. H. Du, J. P. DeGrave, F. Xue, D. Liang, W. Ning, J. Yang, M. Tian, Y. Zhang and S. Jin, *Nano Letters*, 2014, **14**, 2026-2032.
14. H. S. Park, X. Yu, S. Aizawa, T. Tanigaki, T. Akashi, Y. Takahashi, T. Matsuda, N. Kanazawa, Y. Onose, D. Shindo, A. Tonomura and Y. Tokura, *Nature Nanotechnology*, 2014, **9**, 337-342.
15. N. Romming, C. Hanneken, M. Menzel, J. E. Bickel, B. Wolter, K. von Bergmann, A. Kubetzka and R. Wiesendanger, *Science*, 2013, **341**, 636-639.
16. A. Hrabec, N. A. Porter, A. Wells, M. J. Benitez, G. Burnell, S. McVitie, D. McGrouther, T. A. Moore and C. H. Marrows, *Physical Review B*, 2014, **90**, 020402.
17. H. Yang, A. Thiaville, S. Rohart, A. Fert and M. Chshiev, *Physical Review Letters*, 2015, **115**, 267210.

18. A. Belabbes, G. Bihlmayer, F. Bechstedt, S. Blügel and A. Manchon, *Physical Review Letters*, 2016, **117**, 247202.

19. S. Woo, K. Litzius, B. Krüger, M.-Y. Im, L. Caretta, K. Richter, M. Mann, A. Krone, R. M. Reeve, M. Weigand, P. Agrawal, I. Lemesh, M.-A. Mawass, P. Fischer, M. Kläui and G. S. D. Beach, *Nature materials*, 2016, **15**, 501.

20. M. Belmeguenai, J.-P. Adam, Y. Roussigné, S. Eimer, T. Devolder, J.-V. Kim, S. M. Cherif, A. Stashkevich and A. Thiaville, *Physical Review B*, 2015, **91**, 180405.

21. K. Di, V. L. Zhang, H. S. Lim, S. C. Ng, M. H. Kuok, J. Yu, J. Yoon, X. Qiu and H. Yang, *Physical Review Letters*, 2015, **114**, 047201.

22. A. W. J. Wells, P. M. Shepley, C. H. Marrows and T. A. Moore, *Physical Review B*, 2017, **95**, 054428.

23. T. Ha Pham, J. Vogel, J. Sampaio, M. Vaňatka, J. C. Rojas-Sánchez, M. Bonfim, D. S. Chaves, F. Choueikani, P. Ohresser, E. Otero, A. Thiaville and S. Pizzini, *Europhysics Letters*, 2016, **113**, 67001.

24. K. Di, V. L. Zhang, H. S. Lim, S. C. Ng, M. H. Kuok, X. Qiu and H. Yang, *Applied Physics Letters*, 2015, **106**, 052403.

25. O. Boulle, S. Rohart, L. D. Buda-Prejbeanu, E. Jué, I. M. Miron, S. Pizzini, J. Vogel, G. Gaudin and A. Thiaville, *Physical Review Letters*, 2013, **111**, 217203.

26. S. Pizzini, J. Vogel, S. Rohart, L. D. Buda-Prejbeanu, E. Jué, O. Boulle, I. M. Miron, C. K. Safeer, S. Auffret, G. Gaudin and A. Thiaville, *Physical Review Letters*, 2014, **113**, 047203.

27. R. M. Rowan-Robinson, A. A. Stashkevich, Y. Roussigné, M. Belmeguenai, S. M. Chérif, A. Thiaville, T. P. A. Hase, A. T. Hindmarch and D. Atkinson, *Scientific Reports*, 2017, **7**, 16835.

28. S. Jaiswal, K. Litzius, I. Lemesh, F. Büttner, S. Finizio, J. Raabe, M. Weigand, K. Lee, J. Langer, B. Ocker, G. Jakob, G. S. D. Beach and M. Kläui, *Applied Physics Letters*, 2017, **111**, 022409.

29. J. E. Hirsch, *Physical Review Letters*, 1999, **83**, 1834-1837.

30. E. Martinez, S. Emori and G. S. D. Beach, *Applied Physics Letters*, 2013, **103**, 072406.

31. L. Liu, C.-F. Pai, Y. Li, H. W. Tseng, D. C. Ralph and R. A. Buhrman, *Science*, 2012, **336**, 555-558.

32. T. Jungwirth, J. Wunderlich and K. Olejník, *Nature materials*, 2012, **11**, 382.

33. A. Manchon, H. C. Koo, J. Nitta, S. M. Frolov and R. A. Duine, *Nature materials*, 2015, **14**, 871.

34. S.-h. C. Baek, V. P. Amin, Y.-W. Oh, G. Go, S.-J. Lee, G.-H. Lee, K.-J. Kim, M. D. Stiles, B.-G. Park and K.-J. Lee, *Nature materials*, 2018, **17**, 509-513.

35. J. Sinova, S. O. Valenzuela, J. Wunderlich, C. H. Back and T. Jungwirth, *Reviews of Modern Physics*, 2015, **87**, 1213-1260.

36. A. Belavin and A. Polyakov, *Jetp Letters*, 1975, **22**, 245-248.

37. A. A. Kovalev and S. Sandhoefner, *Frontiers in Physics*, 2018, **6**.

38. X. Zhang, Y. Zhou, K. M. Song, T.-E. Park, J. Xia, M. Ezawa, X. Liu, W. Zhao, G. Zhao and S. Woo, *arXiv preprint arXiv:1906.04718*, 2019.

39. A. K. Nayak, V. Kumar, T. Ma, P. Werner, E. Pippel, R. Sahoo, F. Damay, U. K. Rößler, C. Felser and S. S. P. Parkin, *Nature*, 2017, **548**, 561-566.

40. W. Koshibae and N. Nagaosa, *Nature Communications*, 2016, **7**, 10542.

41. S. Bera and S. S. Mandal, *Physical Review Research*, 2019, **1**, 033109.

42. X. Z. Yu, W. Koshibae, Y. Tokunaga, K. Shibata, Y. Taguchi, N. Nagaosa and Y. Tokura, *Nature*, 2018, **564**, 95-98.

43. X. Z. Yu, Y. Tokunaga, Y. Kaneko, W. Z. Zhang, K. Kimoto, Y. Matsui, Y. Taguchi and Y. Tokura, *Nature Communications*, 2014, **5**, 3198.

44. P. Upadhyaya, G. Yu, P. K. Amiri and K. L. Wang, *Physical Review B*, 2015, **92**, 134411.

45. W. Kang, Y. Huang, C. Zheng, W. Lv, N. Lei, Y. Zhang, X. Zhang, Y. Zhou and W. Zhao, *Scientific Reports*, 2016, **6**, 23164.

46. A. Rosch, *Nature Nanotechnology*, 2016, **advance online publication**.

47. P. J. Hsu, A. Kubetzka, A. Finco, N. Romming, K. von Bergmann and R. Wiesendanger, *Nature Nanotechnology*, 2017, **12**, 123-126.

48. X. Wang, W. L. Gan, J. C. Martinez, F. N. Tan, M. B. A. Jalil and W. S. Lew, *Nanoscale*, 2018, **10**, 733-740.

49. H. Xia, C. Song, C. Jin, J. Wang, J. Wang and Q. Liu, *Journal of Magnetism and Magnetic Materials*, 2018, **458**, 57-61.

50. C. C. I. Ang, W. Gan and W. S. Lew, *New Journal of Physics*, 2019, **21**.

51. C. Ma, X. Zhang, J. Xia, M. Ezawa, W. Jiang, T. Ono, S. N. Piramanayagam, A. Morisako, Y. Zhou and X. Liu, *Nano Letters*, 2019, **19**, 353-361.

52. A. A. Thiele, *Physical Review Letters*, 1973, **30**, 230-233.

53. A. Brataas, A. D. Kent and H. Ohno, *Nature materials*, 2012, **11**, 372-381.

54. A. Fert, V. Cros and J. Sampaio, *Nature Nanotechnology*, 2013, **8**, 152-156.

55. J. Iwasaki, M. Mochizuki and N. Nagaosa, *Nature Nanotechnology*, 2013, **8**, 742-747.

56. J. Iwasaki, W. Koshibae and N. Nagaosa, *Nano Letters*, 2014, **14**, 4432-4437.

57. C. Schütte, J. Iwasaki, A. Rosch and N. Nagaosa, *Physical Review B*, 2014, **90**, 174434.

58. Y. Zhou and M. Ezawa, *Nature Communications*, 2014, **5**, 4652.

59. J. Ding, X. Yang and T. Zhu, *Journal of Physics D: Applied Physics*, 2015, **48**, 115004.

60. Y. Nakagome, M. Horiguchi, T. Kawahara and K. Itoh, *IBM journal of research and development*, 2003, **47**, 525-552.

61. K. S. Ryu, S. H. Yang, L. Thomas and S. S. Parkin, *Nature Communications*, 2014, **5**, 3910.

62. S.-H. Yang, K.-S. Ryu and S. Parkin, *Nature Nanotechnology*, 2015, **10**, 221-226.

63. J. Müller, *New Journal of Physics*, 2017, **19**, 025002.

64. S. S. Parkin, M. Hayashi and L. Thomas, *Science*, 2008, **320**, 190-194.

65. R. Tomasello, V. Puliafito, E. Martinez, A. Manchon, M. Ricci, M. Carpentieri and G. Finocchio, *Journal of Physics D: Applied Physics*, 2017, **50**, 325302.

66. X. Zhang, G. P. Zhao, H. Fangohr, J. P. Liu, W. X. Xia, J. Xia and F. J. Morvan, *Scientific Reports*, 2015, **5**, 7643.

67. Y. Zhang, S. Luo, B. Yan, J. Ou-Yang, X. Yang, S. Chen, B. Zhu and L. You, *Nanoscale*, 2017, DOI: 10.1039/C7NR01980G.

68. D. M. Crum, M. Bouhassoune, J. Bouaziz, B. Schweflinghaus, S. Blügel and S. Lounis, *Nature Communications*, 2015, **6**, 8541.

69. S. Ikeda, K. Miura, H. Yamamoto, K. Mizunuma, H. D. Gan, M. Endo, S. Kanai, J. Hayakawa, F. Matsukura and H. Ohno, *Nature materials*, 2010, **9**, 721.

70. A. Kubetzka, C. Hanneken, R. Wiesendanger and K. von Bergmann, *Physical Review B*, 2017, **95**, 104433.

71. R. Tomasello, M. Ricci, P. Burrascano, V. Puliafito, M. Carpentieri and G. Finocchio, *Aip Advances*, 2017, **7**, 056022.

72. X. Zhang, W. Cai, X. Zhang, Z. Wang, Z. Li, Y. Zhang, K. Cao, N. Lei, W. Kang, Y. Zhang, H. Yu, Y. Zhou and W. Zhao, *ACS Applied Materials & Interfaces*, 2018, **10**, 16887-16892.

73. M. Wilkes and W. Renwick, *Electronic Engineering*, 1948, **20**, 208.

74. J. P. Eckert, *IEEE Annals of the History of Computing*, 1998, **20**, 15-28.

75. H. Du, D. Liang, C. Jin, L. Kong, M. J. Stolt, W. Ning, J. Yang, Y. Xing, J. Wang, R. Che, J. Zang, S. Jin, Y. Zhang and M. Tian, *Nature Communications*, 2015, **6**, 7637.

76. C. Hanneken, F. Otte, A. Kubetzka, B. Dupé, N. Romming, K. von Bergmann, R. Wiesendanger and S. Heinze, *Nature Nanotechnology*, 2015, **10**, 1039.

77. J.-G. Zhu and C. Park, *Materials Today*, 2006, **9**, 36-45.

78. D. Maccariello, W. Legrand, N. Reyren, K. Garcia, K. Bouzehouane, S. Collin, V. Cros and A. Fert, *Nature Nanotechnology*, 2018, **13**, 233-237.

79. C. Guite, I. S. Kerk, M. C. Sekhar, M. Ramu, S. Goolaup and W. S. Lew, *Scientific Reports*, 2014, **4**, 7459.

80. T. Phung, A. Pushp, L. Thomas, C. Rettner, S.-H. Yang, K.-S. Ryu, J. Baglin, B. Hughes and S. Parkin, *Nano Letters*, 2015, **15**, 835-841.

81. S. F. Zhang, W. L. Gan, J. Kwon, F. L. Luo, G. J. Lim, J. B. Wang and W. S. Lew, *Scientific Reports*, 2016, **6**, 24804.

82. W. Jiang, P. Upadhyaya, W. Zhang, G. Yu, M. B. Jungfleisch, F. Y. Fradin, J. E. Pearson, Y. Tserkovnyak, K. L. Wang, O. Heinonen, S. G. E. te Velthuis and A. Hoffmann, *Science*, 2015, **349**, 283-286.

83. F. Büttner, I. Lemesh, M. Schneider, B. Pfau, C. M. Günther, P. Hessing, J. Geilhufe, L. Caretta, D. Engel, B. Krüger, J. Viefhaus, S. Eisebitt and G. S. D. Beach, *Nature Nanotechnology*, 2017, **12**, 1040.

84. D. Cortes-Ortuno, W. Wang, M. Beg, R. A. Pepper, M. A. Bisotti, R. Carey, M. Vousden, T. Kluyver, O. Hovorka and H. Fangohr, *Scientific Reports*, 2017, **7**, 4060.

85. M. B. A. Jalil, S. G. Tan, Z. B. Siu, W. Gan, I. Purnama and W. S. Lew, *Journal of Magnetism and Magnetic Materials*, 2016, **399**, 155-158.

86. R. P. Loreto, W. A. Moura-Melo, A. R. Pereira, X. Zhang, Y. Zhou, M. Ezawa and C. I. L. de Araujo, *Journal of Magnetism and Magnetic Materials*, 2018, **455**, 25-31.

87. S. Montoya, S. Couture, J. Chess, J. Lee, N. Kent, D. Henze, S. Sinha, M.-Y. Im, S. Kevan and P. Fischer, *arXiv preprint arXiv:1608.01368*, 2016.

88. C. Moreau-Luchaire, S. C. Mouta, N. Reyren, J. Sampaio, C. A. Vaz, N. Van Horne, K. Bouzehouane, K. Garcia, C. Deranlot, P. Warnicke, P. Wohlhuter, J. M. George, M. Weigand, J. Raabe, V. Cros and A. Fert, *Nature Nanotechnology*, 2016, **11**, 444-448.

89. R. L. Novak, F. Garcia, E. R. P. Novais, J. P. Sinnecker and A. P. Guimarães, *Journal of Magnetism and Magnetic Materials*, 2018, **451**, 749-760.

90. H. Oike, A. Kikkawa, N. Kanazawa, Y. Taguchi, M. Kawasaki, Y. Tokura and F. Kagawa, *Nature Physics*, 2015, **12**, 62-66.

91. S. D. Pollard, J. A. Garlow, J. Yu, Z. Wang, Y. Zhu and H. Yang, *Nature Communications*, 2017, **8**, 14761.

92. J. Sampaio, V. Cros, S. Rohart, A. Thiaville and A. Fert, *Nature Nanotechnology*, 2013, **8**, 839-844.

93. D. Prychynenko, M. Sitte, K. Litzius, B. Krüger, G. Bourianoff, M. Kläui, J. Sinova and K. Everschor-Sitte, *Physical Review Applied*, 2018, **9**, 014034.

94. S. Li, W. Kang, Y. Huang, X. Zhang, Y. Zhou and W. Zhao, *Nanotechnology*, 2017, **28**, 31LT01.

95. G. Bourianoff, D. Pinna, M. Sitte and K. Everschor-Sitte, *Aip Advances*, 2018, **8**, 055602.

96. C. Reichhardt and C. J. O. Reichhardt, *Journal of Physics: Condensed Matter*, 2018, **31**, 07LT01.

97. X. Chen, W. Kang, D. Zhu, X. Zhang, N. Lei, Y. Zhang, Y. Zhou and W. Zhao, *Nanoscale*, 2018, **10**, 6139-6146.

98. M. Chen, A. Sengupta and K. Roy, *Ieee Transactions on Magnetics*, 2018, **54**, 1-7.

99. K. Litzius, I. Lemesh, B. Krüger, P. Bassirian, L. Caretta, K. Richter, F. Büttner, K. Sato, O. A. Tretiakov, J. Förster, R. M. Reeve, M. Weigand, I. Bykova, H. Stoll, G. Schütz, G. S. D. Beach and M. Kläui, *Nature Physics*, 2016, **13**, 170.

100. X. Zhang, Y. Zhou and M. Ezawa, *Nature Communications*, 2016, **7**, 10293.

101. W. Jiang, X. Zhang, G. Yu, W. Zhang, X. Wang, M. Benjamin Jungfleisch, J. E. Pearson, X. Cheng, O. Heinonen, K. L. Wang, Y. Zhou, A. Hoffmann and S. G. E. te Velthuis, *Nature Physics*, 2017, **13**, 162-169.

102. N. Nagaosa and Y. Tokura, *Nature Nanotechnology*, 2013, **8**, 899-911.

103. I. Purnama, W. L. Gan, D. W. Wong and W. S. Lew, *Scientific Reports*, 2015, **5**, 10620.

104. W. S. Lew, W. L. Gan, I. Purnama and F. Ma, in *Skyrmions*, CRC Press, 2016, pp. 429-456.

105. H. T. Fook, W. L. Gan, I. Purnama and W. S. Lew, *Ieee Transactions on Magnetics*, 2015, **51**, 1-4.

106. P. Lai, G. Zhao, H. Tang, N. Ran, S. Wu, J. Xia, X. Zhang and Y. Zhou, *Scientific Reports*, 2017, **7**, 45330.

107. Y. Zhang, S. Luo, B. Yan, J. Ou-Yang, X. Yang, S. Chen, B. Zhu and L. You, *Nanoscale*, 2017, **9**, 10212-10218.

108. S. Bhatti and S. N. Piramanayagam, *physica status solidi (RRL) – Rapid Research Letters*, 2019, **0**, 1900090.

109. S. Krishnia, P. Sethi, W. L. Gan, F. N. Kholid, I. Purnama, M. Ramu, T. S. Herng, J. Ding and W. S. Lew, *Scientific Reports*, 2017, **7**, 11715.

110. V. Baltz, A. Manchon, M. Tsoi, T. Moriyama, T. Ono and Y. Tserkovnyak, *Reviews of Modern Physics*, 2018, **90**, 015005.

111. B. Göbel, A. Mook, J. Henk and I. Mertig, *Physical Review B*, 2017, **96**, 060406.

112. J. Barker and O. A. Tretiakov, *Physical Review Letters*, 2016, **116**, 147203.

113. R. M. Menezes, J. Mulkers, C. C. d. S. Silva and M. V. Milošević, *Physical Review B*, 2019, **99**, 104409.

114. X. Zhang, Y. Zhou and M. Ezawa, *Scientific Reports*, 2016, **6**, 24795.

115. S. Woo, K. M. Song, X. Zhang, Y. Zhou, M. Ezawa, X. Liu, S. Finizio, J. Raabe, N. J. Lee and S.-I. Kim, *Nature Communications*, 2018, **9**, 959.

116. L. Caretta, M. Mann, F. Büttner, K. Ueda, B. Pfau, C. M. Günther, P. Hessing, A. Churikova, C. Klose, M. Schneider, D. Engel, C. Marcus, D. Bono, K. Bagschik, S. Eisebitt and G. S. D. Beach, *Nature Nanotechnology*, 2018, **13**, 1154-1160.

Chapter 2 Model for magnetization dynamics

The magnetization dynamics of a material is governed by the collective effects of its individual spin angular momentums, which is an intrinsic quantum property that does not have a classical parallel. In this chapter, we will discuss the Landau-Lifshitz-Gilbert equation that governs the magnetization dynamics and introduces the various effective fields that can act on the spin angular momentum. With this all-encompassing model, magnetization dynamics of macroscopic systems, such as those supporting the formation of skyrmions, can be numerically solved with finite difference algorithms.

2.1 Landau-Lifshitz-Gilbert Equation

The Hamiltonian of a single spin angular momentum **S**, under a time-varying applied magnetic field **B** is given by:[1]

$$H_s = \frac{g\mu_B}{\hbar}\mathbf{S}\cdot\mathbf{B}(t) \qquad \text{Equation 2-1}$$

where g is the gyromagnetic ratio, μ_B is the Bohr magneton. By applying the angular momentum commutation relations on the Schrödinger equation, the following is obtained:

$$\frac{d}{dt}\langle\mathbf{S}(t)\rangle = \frac{g\mu_B}{\hbar}\langle\mathbf{S}(t)\rangle\times\mathbf{B}(t) \qquad \text{Equation 2-2}$$

where $\langle\mathbf{S}(t)\rangle$ is the expectation value of the **S**. However, most magnetic materials are quantified based on their magnetization vector **M**. Therefore, we can define magnetization to be:

$$\mathbf{M} = \left(\frac{g\mu_B}{\hbar}\right)\langle\mathbf{S}\rangle \qquad \text{Equation 2-3}$$

The magnitude of the magnetization vector **M** is given by the magnetization per unit volume of the material itself. Substituting into Equation 2-2, the following is obtained:

$$\frac{d\mathbf{M}}{dt} = -\gamma_0\left[\mathbf{M}(t)\times\mathbf{H}(t)\right] \qquad \text{Equation 2-4}$$

where $\gamma_0 = \frac{\mu_0 g \mu_B}{\hbar}$ is the gyromagnetic ratio. Equation 2-4 describes the magnetization precession around an external magnetic field. However, in experiments, it was found that the macroscopic magnetization always aligns with the external magnetic field and that the precession was damped within tens of nanoseconds. This led Landau and Lifshitz to introduce a damping parameter that produces the Landau-Lifshitz equation:

$$\frac{d\mathbf{m}}{dt} = -\gamma_0 \left[\mathbf{m} \times \mathbf{B}\right] + \lambda \left[\mathbf{m} \times \left(\mathbf{m} \times \mathbf{B}\right)\right] \qquad \text{Equation 2-5}$$

where $\mathbf{m} = \frac{\mathbf{M}}{\|\mathbf{M}\|}$ is the normalized magnetization and $\lambda = \alpha\gamma_0$ is the phenomenological damping parameter and α is the dimensionless damping factor. Damping can be attributed to eddy currents,[2] the coupling of the magnetization field to spin waves, lattice vibrations, and crystallographic defects.

In 1955, T. L. Gilbert proposed that the damping term should be more accurately represented by a term that relies on the time derivative of the magnetization.[3, 4] The equation, commonly known as the Landau-Lifshitz-Gilbert equation can be written as:[5]

$$\frac{d\mathbf{m}}{dt} = -\gamma_0 \left[\mathbf{m} \times \mathbf{B} - \alpha \left(\mathbf{m} \times \frac{d\mathbf{m}}{dt}\right)\right] \qquad \text{Equation 2-6}$$

The LLG equation produces more accurate predictions when the material damping is large. Therefore, it has been regarded as the gold standard for magnetization dynamics.[6, 7] However, the LLG equation has the disadvantage of having the time-derivative of magnetization on both sides which makes it difficult to solve. Fortunately, the LLG equation is mathematically equivalent to the LL equation, given several substitutions:[3]

$$\lambda = \frac{\gamma_0 \alpha}{1+\alpha^2} \qquad \text{Equation 2-7}$$

$$\gamma_0' = \frac{\gamma_0}{1+\alpha^2} \qquad \text{Equation 2-8}$$

which gives us the simplified LLG equation:

$$\frac{d\mathbf{m}}{dt} = -\gamma_0' \left[\mathbf{m} \times \mathbf{B} - \alpha \left(\mathbf{m} \times \left(\mathbf{m} \times \mathbf{B}\right)\right)\right] \qquad \text{Equation 2-9}$$

In Figure 2-1, the spin dynamics under an applied magnetic field is plotted. Without the Gilbert damping parameter, the spin precesses indefinitely due to the direction of $\frac{d\mathbf{m}}{dt}$ which is perpendicular to **B**. With the addition of a small Gilbert damping, **m** eventually damps to the direction of the external magnetic field. The rate at which the damping occurs is given by the magnitude of the Gilbert damping parameter, which is usually between 0.01 to 0.3 for thin film materials commonly used for skyrmion studies.[8-11]

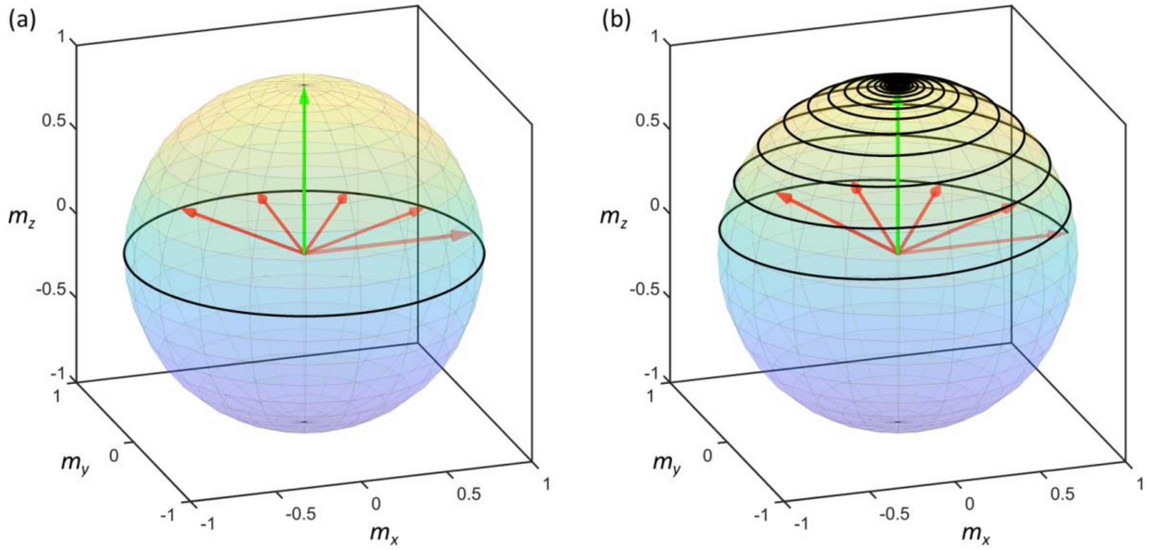

Figure 2-1 The spin dynamics as modelled by the LLG equation. The spin angular momentum is represented by the red arrows, the applied magnetic field by the green arrow and the black lines represents the trajectory of the spin angular momentum over time. Spin dynamics (a) without damping and (b) with damping term.

2.2 Effective fields

While Figure 2-1 models the spin dynamics of a single spin, magnetic materials are most often considered as an ensemble of spins with mutual interactions. As such, the most complex component of magnetization dynamics is in the calculation of the various interactions acting on each local magnetization unit. While the interactions are varied, they can all be quantified by effective fields which then allow all interactions to be summed together. The effective fields can then be substituted into Equation 2-9:

$$\frac{d\mathbf{m}}{dt} = -\gamma_0 \frac{1}{1+\alpha^2}\left[\mathbf{m}\times\mathbf{B}_{eff} + \alpha\left(\mathbf{m}\times\left(\mathbf{m}\times\mathbf{B}_{eff}\right)\right)\right] \qquad \text{Equation 2-10}$$

In this subsection, we discuss in detail each of the effective fields.

2.2.1 Magnetostatic interactions

Magnetic moments experience a torque when subject to a magnetic field, which eventually aligns the magnetic moments to the net magnetic field. The experienced magnetic fields can be extrinsic, as in the case of an applied magnetic field, or intrinsic in the form of a demagnetizing field. The latter field arises from the magnetic field generated by each magnetic dipole in the system. While the demagnetizing field can be solved analytically for well-behaving shapes, most situations call for costly and complex numerical calculations.[12]

Demagnetizing fields have a great influence on the magnetization states and dynamics. For example, anisotropic shapes like bars typically have their magnetization aligned along the long axis to reduce the surface magnetic charges. Figure 2-2(a-b) shows the surface charge distribution in an elongated shape. The resulting magnetic anisotropy is termed shape anisotropy and has been used in magnetic memory devices to form energy barriers between states.[13] In the perpendicularly magnetized thin films that are central to this thesis, the demagnetizing factor is ~1 due to the generation of surface charges on the film surface. This indicates that each magnetic moment experiences a magnetic field that is equal to its saturation magnetization $\mathbf{B}_{\text{sat}}$. When a skyrmion is nucleated, it experiences a demagnetizing field from its surrounding, as illustrated in Figure 2-2 (c). This interaction can stabilize skyrmions.[14] In Figure 2-2 (d), the skyrmion-skyrmion repulsion is shown. Due to the similar magnetic charges that form on skyrmions, they are known to mutually repel.[15, 16] This places a limit to the maximum skyrmion density and thus a maximum data density for skyrmion memory devices.

In the implementation of micromagnetics, magnetostatic interactions have a very high computational cost as compared to the other types of interaction due to its long-ranged nature; every magnetization produces a magnetic field that acts on all other magnetizations. Most micromagnetic solvers apply the convolution theorem to complete the calculation efficiently. Once calculated, the magnetostatic fields are directly added to the $\mathbf{B}_{eff}$ term in the LLG equation.

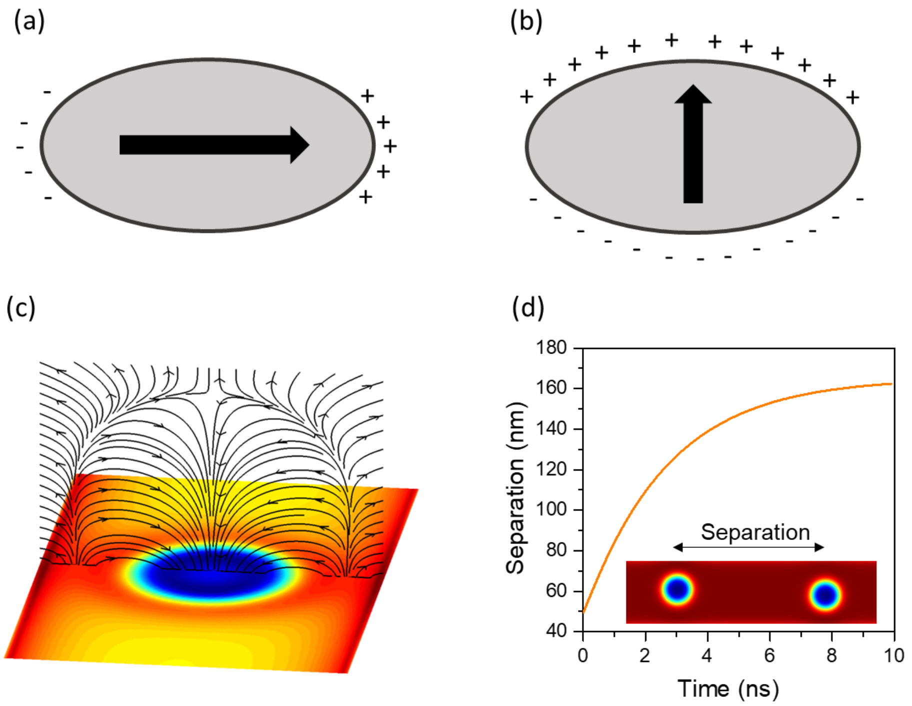

Figure 2-2 (a) Illustration of surface charge generation due to magnetization direction in an elongated shape. (b) Surface charges are greatly increased when the magnetization does not lie in the long axis. (c) Stray magnetic field emanating from the nanowire and flowing into the skyrmion centre. (d) Skyrmion separation over time, demonstrating the magnetostatic field-induced repulsion.

2.2.2 Exchange interaction

The exchange interaction is the phenomena responsible for the four types of magnetism exhibited by all materials; ferromagnetism, antiferromagnetism, diamagnetism, and paramagnetism. However, only ferromagnetism can produce macroscopic and significant magnetic interactions and are therefore commonly referred by many to be “magnetic”. Ferromagnetic materials, as compared to the other three types of magnetic materials, have become an integral part of modern technology, due to their ability to produce macroscopically-evident interactions. Ferromagnetic materials form the core element for hard disks, motors, generators, speakers, and electromagnets etc. Thus, it would be difficult to imagine the absence of ferromagnetism, despite only a few pure elements exhibiting this type of magnetism.

At its core, the exchange interaction is a quantum mechanical interaction that occurs between electrons. Due to the antisymmetric shape of an electron’s wavefunction, the superposition of two electrons of the same spin always result in an expectation value of zero at their center. The phenomenon is better known as the Pauli-exclusion principle, which states that two fermions cannot occupy the same quantum states at the same time. The quantum mechanical effect itself does not result in a preference between parallel and antiparallel spin configurations. However, when coulombic repulsion is considered, a difference in electrostatic energy results. Considering two electrons with opposite spins, the quantum superposition of the electrons allows them to occupy the same space. However, significant electrostatic energy is required to maintain the electrons' close proximity. On the other hand, electrons with parallel spins have expectation values that are further away and thus incur a lower cost in electrostatic energy. The difference in the electrostatic energy results in the preference for parallel spins.[17]

The example given is true only for a particular overlap of wavefunction between the valence electrons of two neighbouring atoms. In general, the overlap is not perfect and depending on the phase, antiparallel spins can be favoured. In 1930, John C. Slater proposed the idea that the antiferromagnetic and ferromagnetic type ordering can be predicted based on the interatomic distance. Illustrated by Bethe later, the Bethe-Slater curve in Figure 2-3 show good agreement with observed exchange energy of atoms with unpaired 3d valence electrons.

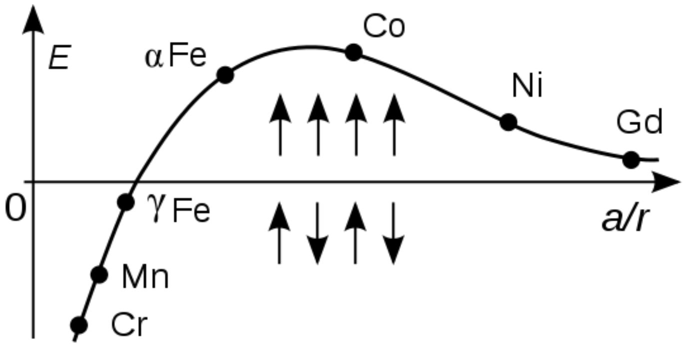

Figure 2-3 The Bethe-Slater curve. It provides a heuristic understanding of the exchange interaction. The *x*-axis shows the ratio of atomic separation *a* and atomic radius *r*. At exchange energy $E < 0$, antiferromagnetism results.

The Hamiltonian of the exchange interaction between two spins can be given by:

$$H = -J_{ex}\left(\mathbf{S}_1 \cdot \mathbf{S}_2\right) \qquad \text{Equation 2-11}$$

where J_{ex} is the exchange coefficient and its sign determine whether the exchange is ferromagnetic or antiferromagnetic. In micromagnetic simulations where each cell volume can represent more than one spin, the exchange stiffness A_{ex} (J/m) is often used. A_{ex} is given by $\frac{4J_{ex}}{a}$ in fcc lattices where a is the lattice parameter. In the continuum limit, the effective field is expressed as:

$$\mathbf{B}_{exch} = \frac{2A_{ex}}{M_{sat}} \Delta\mathbf{m} \qquad \text{Equation 2-12}$$

where A_{ex} is the exchange stiffness, M_{sat} is the saturation magnetization, and $\mathbf{m}$ is the reduced magnetization. For numerical calculations, the magnetization volume is discretized into a cuboidal lattice. Thus, the six nearest-neighbour approximation is used:[18, 19]

$$\mathbf{B}_{exch} = \frac{2A_{ex}}{M_{sat}} \sum_i \frac{\mathbf{m}_i - \mathbf{m}}{\Delta r_i^2} \qquad \text{Equation 2-13}$$

where i is the index of the six nearest-neighbours. An important consequence of using only six neighbours is that the spin angles should be kept as small as possible by using a smaller discretization cuboid. At regions where the magnetization is missing a neighbour, the Neumann boundary condition is used.

2.2.3 Dzyaloshinskii-Moriya interaction

The DMI is an anisotropic superexchange interaction that was first proposed to exist in $\alpha-\mathrm{Fe_2O_3}$ to explain the presence of weak ferromagnetism in the antiferromagnet.[20] In 1958, Moriya theorized that spin-orbit coupling was responsible for the interaction.[21] As shown in Figure 1-5, DMI in magnetic thin films is mediated by the presence of heavy atoms with strong spin-orbit coupling. Here, we recall that the DMI is given by:

$$H_{DM} = \mathbf{D}_{ij} \cdot \left(\mathbf{m}_i \times \mathbf{m}_j\right) \qquad \text{Equation 2-14}$$

where $\mathbf{D}_{ij}$ is the DMI vector and i, j are the indices of two adjacent magnetic moments. Defining $\Delta\mathbf{m}_{ij} = \mathbf{m}_j - \mathbf{m}_i$ and assuming that $\Delta\mathbf{m}_{ij} \ll 1$, we can approximate that:

$$\Delta\mathbf{m}_{ij} \approx \left(\mathbf{r}_{ij} \cdot \nabla\right)\mathbf{m} \qquad \text{Equation 2-15}$$

where $\mathbf{r}_{ij}$ is the separation vector. Substituting Equation 2-12 into 2-11, we have:

$$\begin{aligned} H_{DM} &= \mathbf{D}_{ij} \cdot \left[\mathbf{m}_i \times \left(\mathbf{m}_i + \Delta\mathbf{m}_i\right)\right] \\ &= \mathbf{D}_{ij} \cdot \left(\mathbf{m}_i \times \Delta\mathbf{m}_i\right) \\ &= \mathbf{D} \cdot \left(\mathbf{m} \times \left(\mathbf{r} \cdot \nabla\right)\mathbf{m}\right) \end{aligned} \qquad \text{Equation 2-16}$$

where in the last line, the indices can be removed since the operation is centered on $\mathbf{m}_i$ alone. Here, we note that Equation 2-13 is general since the DMI vector **D** can be oriented in any direction. However, for the interfacial DMI studied, **D** is on the same plane as **r** but $\mathbf{D} \perp \mathbf{r}$.[22] Then, $\mathbf{D} = D\left(\hat{r} \times \hat{z}\right)$ and the DMI energy is given by:

$$\begin{aligned} H_{DM} &= D\left|\mathbf{r}\right|\left[\mathbf{m} \times \left(\mathbf{r} \cdot \nabla\right)\mathbf{m}\right] \cdot \left(\hat{r} \times \hat{z}\right) \\ &= D\left|\mathbf{r}\right|\left[\left(\mathbf{m} \cdot \nabla\right)\mathbf{m} - \mathbf{m}\left(\nabla \cdot \mathbf{m}\right)\right] \cdot \hat{z} \end{aligned} \qquad \text{Equation 2-17}$$

Then the effective field arising from the DMI can be expressed, in vector notation:

$$\mathbf{B}_{DM} = \frac{2D}{M_s}\left(\frac{\partial m_z}{\partial x}, \frac{\partial m_z}{\partial y}, -\frac{\partial m_x}{\partial x} - \frac{\partial m_y}{\partial y}\right) \qquad \text{Equation 2-18}$$

For DMI, a boundary condition is applied to the edge magnetization:[23]

$$\frac{d\mathbf{m}}{dn} = \frac{D}{2A}\left(\hat{z} \times \hat{n}\right) \times \mathbf{m} \qquad \text{Equation 2-19}$$

Where **n** is the direction normal to the edge.

2.2.4 Magnetic anisotropy

Magnetic anisotropy refers to the preference of the magnetization vector to certain axes termed easy axes, in contrast to isotropic materials. Magnetic anisotropy is an umbrella term for all interactions resulting in an anisotropic magnetization. For data storage applications, magnetic anisotropy plays a critical role in locking the magnetization to either direction in an axis. Although the causes can be varied, such as from magnetocrystalline, magnetostrictive, external electric fields, etc., the spin-orbit coupling can be considered the microscopic origin for most of them. With the distortion of the electron orbitals for whatever reasons, magnetic anisotropy is manifested through the spin-orbit coupling.

For the thin films systems considered, a uniaxial anisotropy is dominant and its energy density can be expressed as:[24]

$$\varepsilon_{anis} = -K_{u1}\left(\hat{u}\cdot\mathbf{m}\right)^2 - K_{u2}\left(\hat{u}\cdot\mathbf{m}\right)^4 \tag{Equation 2-20}$$

where K_{u1} and K_{u2} are the first and second-order anisotropy energy terms and $\hat{u}$ is the unit vector representing the anisotropy axis. The corresponding effective field is then:

$$\mathbf{B}_{anis} = \frac{2K_{u1}}{M_s}\left(\hat{u}\cdot\mathbf{m}\right)\hat{u} - \frac{4K_{u2}}{M_s}\left(\hat{u}\cdot\mathbf{m}\right)^3\hat{u} \tag{Equation 2-21}$$

In the 2D skyrmion material systems with strong perpendicular magnetic anisotropy (PMA), the demagnetizing field opposes K_{u1} and reduce its effective field strength. Therefore, the effective anisotropy parameter $K_{u,eff}$ is often used, where $K_{u,eff} = K_{u1} - M_s$.

To create stable skyrmions with large energy barriers preventing its annihilation, a strong $K_{u,eff}$ is necessary.[25, 26] However, large magnetic anisotropies could also prevent the formation of skyrmions, as shown in Figure 2-4.[27] To determine if a material can support skyrmion formation, the critical material parameter $\kappa = \frac{\pi D}{4\sqrt{A_{ex}K_{u,eff}}}$ must be considered.[28, 29] The numerator represents the DMI energy reduction caused by a skyrmion formation while the denominator represents the domain wall energy cost while forming the in-plane components of a skyrmion. When $\kappa > 1$, skyrmions are energetically stable. However, when $\kappa < 1$, skyrmions are metastable states which can spontaneously annihilate. To improve skyrmion stability, it is thus necessary to increase both D and $K_{u,eff}$ simultaneously.

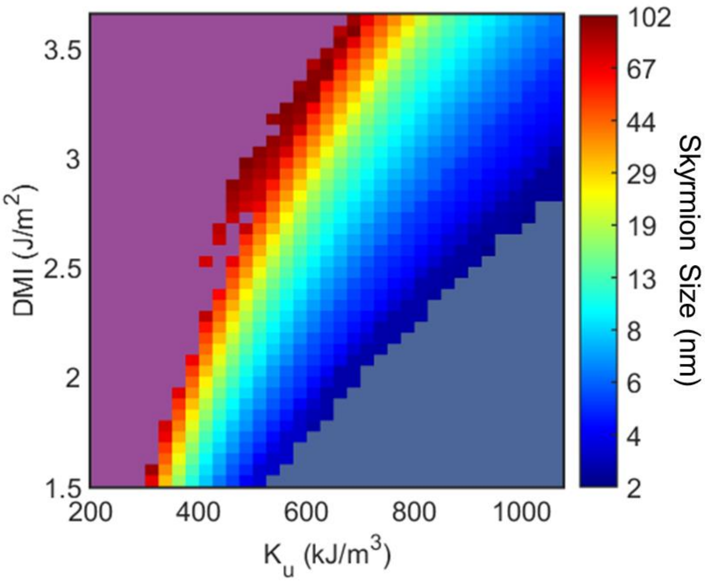

Figure 2-4 Phase diagram showing the skyrmion size as a function of both DMI and magnetic anisotropy (K_u). On the top left section (purple), a chiral stripe state is dominant and, on the bottom right section (dark blue), a ferromagnetic state is dominant.

2.3 Spin transfer torque

The phenomenon of giant magnetoresistance was made known by 1995.[30] As with other forms of magnetoresistance, the resistance of a conducting ferromagnet was found to be dependent on the magnetization states due to spin-dependent scattering. In the following year, seminal work by Slonczewski *et. al.* and Berger *et. al.* demonstrated that the back action of the spin-dependent scattering develops a torque that also acts on the spin.[31, 32] An applied current in a ferromagnet can then develop a nonzero average spin and develops into an angular momentum flux. In spatially varying magnetization, the angular momentum flux creates a net torque that can deflect the local magnetization.[33]

The spin transfer torque (STT) phenomenon is an extremely useful one. For one, it was the key enabling factor in the development of domain wall memories where fast, solid-state operation can be achieved.[34, 35] In Figure 2-5, the illustration shows how the spin-transfer torque due to the angular momentum flux, the magnetization can be shifted in the direction of the electron flow direction.

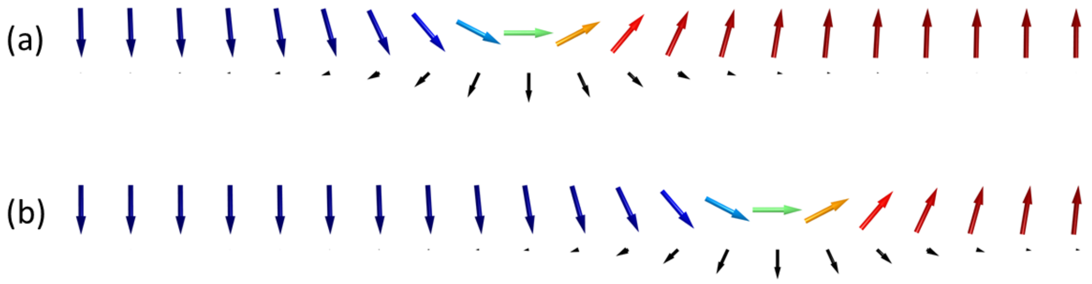

Figure 2-5 Illustration of the spin-transfer torque (black arrows). (b) With the passage of time, the magnetization is shifted in the electron flow direction.

The STT can be integrated into the LLG equation as an additional torque term.[36] The most commonly accepted form of the spin transfer torque is the Zhang-Li spin transfer torque and is given by:[37]

$$\tau_{ZL} = \frac{1}{1+\alpha^2}\left[(1+\xi\alpha)\mathbf{m}\times(\mathbf{m}\times(\mathbf{s}\cdot\nabla)\mathbf{m}) + (\xi-\alpha)\mathbf{m}\times(\mathbf{s}\cdot\nabla)\mathbf{m}\right] \qquad \text{Equation 2-22}$$

where ξ is the degree of non-adiabaticity. **s** is the spin current density given by:

$$\mathbf{s} = \frac{\mu_0 \mu_B}{2e\gamma M_s \left(1+\xi^2\right)} \mathbf{j}$$ Equation 2-23

where μ_0 is the permeability of free space, μ_B is the Bohr magneton, e is the elementary charge, and $\mathbf{j}$ is the current density vector. The two terms in Equation 2-19 represents the adiabatic torque and non-adiabatic terms, which are orthogonal to each other.

2.4 Spin Hall torque

While the spin-transfer torque applies for current flowing within a ferromagnet, the Slonczewski spin-transfer torque was developed for spin currents permeating into a ferromagnet.[32] Cases where this type of spin transfer torque occurs are spin injection from magnetic tunnel junctions,[38, 39] or spin diffusion caused by the spin Hall effect (SHE).[40] Both methods attempt to generate a pure spin current and then to diffuse it on another layer, in order to exert a torque on the ferromagnet. Slonczewski-type spin torques were first considered for the switching of magnetic tunnel junctions.[41] However, in recent years, it has been shown to efficiently propagate chiral spin textures at high velocities.[42]

The geometry for SHE is shown in Figure 2-6 where an unpolarized current passing through a heavy metal generates a transverse spin current.[43] The effect of spin current originating from the spin Hall effect is termed as spin Hall torque. Since it is a torque term, its inclusion in the LLG equation is possible. For a thin film with a current flowing in the in-plane direction, the torque is given by:

$$\tau_{SHE} = \frac{\mu_B \hbar \theta_{SH} j}{2eM_s t} \left[\mathbf{m} \times \left(\mathbf{m} \times \hat{u}_P\right)\right]$$ Equation 2-24

where θ_{SH} is the spin Hall angle which quantizes the efficiency of spin current conversion from charge current, t is the thickness of the ferromagnet, and $\hat{u}_P$ is the polarization of the spin current.

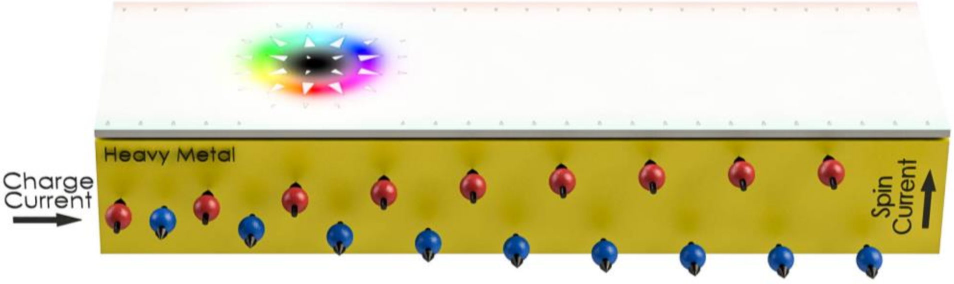

Figure 2-6 Schematic showing the spin separation and resulting spin accumulation within the heavy metal due to the spin Hall effect. The diffusion of spins into the ferromagnet results in the spin Hall torque.

2.5 Micromagnetic simulations

The MuMax3 micromagnetics package was used for the modelling performed in this work. Released in 2015, MuMax3 is the successor to MuMax1 and Mumax2 and exploits the massive parallel computing power of GPUs.[44] MuMax3 uses a finite difference method to discretize the simulation area. To evolve the LLG equation in time, the solver uses explicit Runge-Kutta methods with adaptive time steps to optimize between solver error and solver speed. Although the LLG solver is the main component in a micromagnetic solver, functionalities present in MuMax3 such as geometry creation, region definition, built-in real-time display, and extensibility greatly improve the simulation design workflow. The MuMax3 scripting language is based on a subset of the Go programming language and provides good flexibility while still being concise.[45] Figure 2-7 shows a simulation snapshot of a nanowire where skyrmions are nucleated on the left and shifted right until it is full. The entire script is only 40 lines.

The benefits of GPU-based calculations cannot be understated: it has allowed MuMax3 to achieve tremendously increase of up to 100 times in calculation throughput as compared to CPU-based solvers such as the popular OOMMF.[46, 47] A single computer can also be equipped with multiple GPUs that can perform multiple simulations at once, thus being the more scalable option. Not without drawbacks, the use of GPUs has two noticeable limitations. Most GPUs are equipped to deal only with 32-bit variables due to the low precision required for computer graphics. However, the limitation does not seem to greatly affect the simulation as verified by MuMax3's solution of the standard micromagnetic problems.[46] Also, GPUs typically have lower memory sizes and do not benefit from having expandable memory like the CPU. As such, the maximum simulation grid size is limited. Efficient design methods such as employing periodic boundary conditions should be used to reduce the simulation volume.

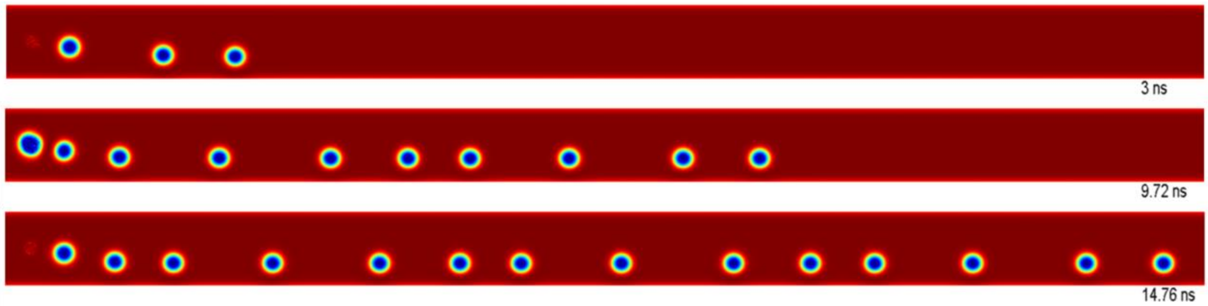

Figure 2-7 Simulation snapshots of a skyrmion racetrack device. Skyrmions are being nucleated on the left and shifted rightwards.

Several modifications were made to the MuMax3 source code and will be discussed here. The first change was made to allow for automatic inclusion of spin Hall torques and STTs when an electric current is applied. By default, MuMax3 only applies the spin Hall torque if a current perpendicular to plane (CPP) with a fixed polarization is applied. This was because, at the time of its conception, MuMax3 was commonly employed to simulate the magnetization dynamics of magnetic tunnel junctions. In our implementation, there is no need to apply current in a CPP geometry in order to generate spin Hall torques. This then removes the perpendicular STT effect which may have be unrealistic in simulations of thicker magnetic materials.

The second modification was to extend the range of the exchange coupling calculation. Originally, only the six nearest neighbours were used for exchange calculations. However, the range is too short for materials with an interlayer exchange coupling mediated by non-magnetic materials. The modification allows the exchange solvers to look at the nearest eight neighbours, which further includes the next nearest top and bottom elements. The change allows the simulation of bilayer skyrmions which has been very interesting for skyrmionic devices.[48, 49]

References

1. M. Lakshmanan, *Philosophical Transactions of the Royal Society A: Mathematical, Physical and Engineering Sciences*, 2011, **369**, 1280-1300.
2. E. Lee, *Proceedings of the IEE-Part C: Monographs*, 1958, **105**, 337-342.
3. T. L. Gilbert, *Ieee Transactions on Magnetics*, 2004, **40**, 3443-3449.
4. M. Lakshmanan and K. Nakamura, *Physical Review Letters*, 1984, **53**, 2497-2499.
5. T. L. Gilbert, *Physical Review*, 1955, **100**, 1243.
6. M. D. Stiles and J. Miltat, in *Spin dynamics in confined magnetic structures III*, Springer, 2006, pp. 225-308.
7. D. C. Mattis, *The theory of magnetism I: Statics and Dynamics*, Springer Science & Business Media, 2012.
8. A. Barman, S. Wang, O. Hellwig, A. Berger, E. E. Fullerton and H. Schmidt, *Journal of Applied Physics*, 2007, **101**, 09D102.
9. Y. Zhao, Q. Song, S. H. Yang, T. Su, W. Yuan, S. S. Parkin, J. Shi and W. Han, *Scientific Reports*, 2016, **6**, 22890.
10. T. Devolder, S. Couet, J. Swerts and G. S. Kar, *Journal of Physics D: Applied Physics*, 2018, **51**, 135002.
11. J. Lourembam, A. Ghosh, M. Zeng, S. K. Wong, Q. J. Yap and S. Ter Lim, *Physical Review Applied*, 2018, **10**, 044057.
12. R. D. McMichael, M. J. Donahue, D. G. Porter and J. Eicke, *Journal of Applied Physics*, 1999, **85**, 5816-5818.
13. K. C. Chun, H. Zhao, J. D. Harms, T.-H. Kim, J.-P. Wang and C. H. Kim, *IEEE Journal of Solid-State Circuits*, 2012, **48**, 598-610.
14. S. A. Montoya, S. Couture, J. J. Chess, J. C. T. Lee, N. Kent, D. Henze, S. K. Sinha, M. Y. Im, S. D. Kevan, P. Fischer, B. J. McMorran, V. Lomakin, S. Roy and E. E. Fullerton, *Physical Review B*, 2017, **95**, 024415.
15. I. Purnama, W. L. Gan, D. W. Wong and W. S. Lew, *Scientific Reports*, 2015, **5**, 10620.
16. X. Zhang, G. P. Zhao, H. Fangohr, J. P. Liu, W. X. Xia, J. Xia and F. J. Morvan, *Scientific Reports*, 2015, **5**, 7643.
17. T. Miyazaki and H. Jin, *The physics of ferromagnetism*, Springer Science & Business Media, 2012.
18. M. J. Donahue, *Journal of Applied Physics*, 1998, **83**, 6491-6493.
19. M. J. Donahue and D. G. Porter, *Physica B: Condensed Matter*, 2004, **343**, 177-183.
20. I. Dzyaloshinsky, *Journal of Physics and Chemistry of Solids*, 1958, **4**, 241-255.

21. T. Moriya, *Physical Review*, 1960, **120**, 91-98.

22. A. N. Bogdanov and U. K. Rößler, *Physical Review Letters*, 2001, **87**, 037203.

23. S. Rohart and A. Thiaville, *Physical Review B*, 2013, **88**.

24. D. Jiles, *Introduction to magnetism and magnetic materials*, CRC press, 2015.

25. D. Cortes-Ortuno, W. Wang, M. Beg, R. A. Pepper, M. A. Bisotti, R. Carey, M. Vousden, T. Kluyver, O. Hovorka and H. Fangohr, *Scientific Reports*, 2017, **7**, 4060.

26. N. K. Duong, M. Raju, A. P. Petrović, R. Tomasello, G. Finocchio and C. Panagopoulos, *Applied Physics Letters*, 2019, **114**, 072401.

27. R. L. Novak, F. Garcia, E. R. P. Novais, J. P. Sinnecker and A. P. Guimarães, *Journal of Magnetism and Magnetic Materials*, 2018, **451**, 749-760.

28. M. Raju, A. Yagil, A. Soumyanarayanan, A. K. C. Tan, A. Almoalem, F. Ma, O. M. Auslaender and C. Panagopoulos, *Nature Communications*, 2019, **10**, 696.

29. A. Soumyanarayanan, M. Raju, A. L. Gonzalez Oyarce, A. K. C. Tan, M.-Y. Im, A. P. Petrović, P. Ho, K. H. Khoo, M. Tran, C. K. Gan, F. Ernult and C. Panagopoulos, *Nature materials*, 2017, **16**, 898.

30. A. Fert, A. Barthélémy, P. Galtier, P. Holody, R. Loloee, R. Morel, F. Pétroff, P. Schroeder, L. B. Steren and T. Valet, *Materials Science and Engineering: B*, 1995, **31**, 1-9.

31. L. Berger, *Physical Review B*, 1996, **54**, 9353-9358.

32. J. C. Slonczewski, *Journal of Magnetism and Magnetic Materials*, 1996, **159**, L1-L7.

33. Y. B. Bazaliy, B. A. Jones and S.-C. Zhang, *Physical Review B*, 1998, **57**, R3213-R3216.

34. A. Thiaville, Y. Nakatani, J. Miltat and Y. Suzuki, *Europhysics Letters*, 2005, **69**, 990-996.

35. S. S. Parkin, M. Hayashi and L. Thomas, *Science*, 2008, **320**, 190-194.

36. S. Zhang, P. M. Levy and A. Fert, *Physical Review Letters*, 2002, **88**, 236601.

37. S. Zhang and Z. Li, *Physical Review Letters*, 2004, **93**, 127204.

38. C. Barraud, P. Seneor, R. Mattana, S. Fusil, K. Bouzehouane, C. Deranlot, P. Graziosi, L. Hueso, I. Bergenti, V. Dediu, F. Petroff and A. Fert, *Nature Physics*, 2010, **6**, 615.

39. S. A. Wolf, D. D. Awschalom, R. A. Buhrman, J. M. Daughton, S. von Molnár, M. L. Roukes, A. Y. Chtchelkanova and D. M. Treger, *Science*, 2001, **294**, 1488.

40. L. Liu, C.-F. Pai, Y. Li, H. W. Tseng, D. C. Ralph and R. A. Buhrman, *Science*, 2012, **336**, 555-558.

41. S. Fukami, T. Anekawa, C. Zhang and H. Ohno, *Nature Nanotechnology*, 2016, **11**, 621.

42. I. Mihai Miron, G. Gaudin, S. Auffret, B. Rodmacq, A. Schuhl, S. Pizzini, J. Vogel and P. Gambardella, *Nature materials*, 2010, **9**, 230.

43. A. Manchon, H. C. Koo, J. Nitta, S. M. Frolov and R. A. Duine, *Nature materials*, 2015, **14**, 871.

44. A. Vansteenkiste and B. Van de Wiele, *Journal of Magnetism and Magnetic Materials*, 2011, **323**, 2585-2591.

45. A. A. Donovan and B. W. Kernighan, *The Go programming language*, Addison-Wesley Professional, 2015.

46. A. Vansteenkiste, J. Leliaert, M. Dvornik, M. Helsen, F. Garcia-Sanchez and B. Van Waeyenberge, *Aip Advances*, 2014, **4**, 107133.

47. M. J. Donahue, *OOMMF user's guide, version 1.0*, 1999.

48. C. C. I. Ang, W. Gan and W. S. Lew, *New Journal of Physics*, 2019, **21**.

49. X. Zhang, Y. Zhou and M. Ezawa, *Nature Communications*, 2016, **7**, 10293.

Chapter 3 Skyrmion motion under spin-orbit torques

In this chapter, we develop a model to describe skyrmion dynamics under the influence of spin-orbit torques. By expanding the method used by Thiele,[1] we show that the presence of spin-orbit torques in a skyrmion-enabled film results in the emergence of a force whose direction and amplitude depend on the configuration and the size of the skyrmion, respectively. Micromagnetics were performed to further corroborate our model accuracy. The model predicts dismal scalability for skyrmionic devices. However, we show that by choosing the correct skyrmion types, an amplification in driving force can be induced which compensates the skyrmion's dismal scaling.

3.1 Introduction

The quest to create hi-performance novel magnetic memory devices has led to significant advances on the topic of spin-orbit torques as well as magnetic skyrmions in recent years.[2-8] The first topic, i.e. the spin-orbit torques, correspond to the torques that are induced by the spin Hall effect and the Rashba effect when electrical currents are injected into a ferromagnetic film interfaced with materials with strong spin-orbit coupling.[9-11] The spin Hall effect is an interfacial spin accumulation that is created due to the deflection of the up and down spins of the conduction electrons. As a result, a transverse pure spin current is created in materials with spin-orbit coupling which in turn exerts a position-dependent torque on the local magnetizations in the ferromagnetic film.[12, 13] On the other hand, the Rashba effect corresponds to the coupling between the spin and the momentum of the conduction electrons of the injected current, which results in the emergence of a field-like torque in the ferromagnetic film.[14-16]

The second topic, i.e. the magnetic skyrmion, represents a single magnetic domain, and therefore it has been proposed to be used as a binary representation in a memory or logic device, in a manner similar to what is shown in Figure 1-12.[17, 18] From the application perspective, the inclusion of spin-orbit torques in magnetic devices has led to fast and energy-efficient device operation,[19-21] whereas research on magnetic skyrmions has led to the conception of novel memory and logic devices.[22-26] However, work on the fundamental understanding of skyrmions under the influence of spin-orbit torque is lacking. Therefore, this chapter serves to create a model from which the high spin-orbit torque efficiencies acting on skyrmions can be understood.

3.2 Model for skyrmion dynamics

In the original Thiele equation, the stable-state motion of a magnetic bubble was obtained by converting the Landau-Lifshitz-Gilbert (LLG) equation into a force equilibrium equation. The Landau-Lifshitz-Gilbert (LLG), which describes the dynamics of the magnetizations (**M**) of a ferromagnet is written as [27, 28]:

$$\frac{d\mathbf{M}}{dt} = -\gamma \mathbf{M} \times \mathbf{H}_{eff} + \frac{\alpha}{M_s} \mathbf{M} \times \frac{d\mathbf{M}}{dt} \ , \qquad \text{Equation 3-1}$$

where γ is the gyromagnetic ratio, H_{eff} is the effective field, α is the damping parameter, and M_{s} is the saturation magnetization constant of the ferromagnetic layer. In the Thiele approach, each term that is described in the LLG equation is associated with a specific magnetic field (**H**). The magnetic fields are then used to calculate the forces that are acting on the skyrmion by using:

$$\mathbf{F} = \int \mathbf{f} dV = -\int (\nabla \mathbf{H}) \cdot \mathbf{M} dV \qquad \text{Equation 3-2}$$

This turns the LLG equation into a force density equilibrium equation [29, 30]:

$$\mathbf{G} \times \mathbf{v} + D(\alpha \mathbf{v}) = 0 \ , \qquad \text{Equation 3-3}$$

where the first term is the gyrocoupling term resulting from magnetization precession with gyrocoupling vector $\mathbf{G} = G\hat{z}$, where $G = \int \frac{d\mathbf{m}}{dx} \times \frac{d\mathbf{m}}{dy} dr^2$ and is equals to 4π for the skyrmion magnetization configuration. The second term is the dissipative force that results from the Gilbert damping parameter α . D is the dissipation dyadic where the elements ∂_{ij} are $\partial_{xx} = \partial_{yy} = \int \frac{d\mathbf{m}}{dx} \cdot \frac{d\mathbf{m}}{dx} + \frac{d\mathbf{m}}{dy} \cdot \frac{d\mathbf{m}}{dy} \cdot dr^2$ for a skyrmion. Otherwise, all elements are zero and D can be treated as a scalar.[31] **v** is the velocity of the skyrmion in the stable-state motion.

It is then possible to extend the Thiele approach to calculate the contribution of spin-orbit torques to the skyrmion dynamics. The associated field ($\mathbf{H}_{SH}$) from the spin Hall effect is written as [32]:

$$\mathbf{H}_{SH} = -\frac{\hbar\theta_H j}{2eM_s t_F}\left(\boldsymbol{\sigma}\times\mathbf{M}\right) = \frac{\hbar\theta_H j}{2eM_s t_F}\begin{pmatrix} M_z \\ 0 \\ -M_x \end{pmatrix} \qquad \text{Equation 3-4}$$

where θ_H is the spin Hall angle characterizing the conversion yield of the longitudinal charge current density into a transverse spin current density, j is the conduction electron current density, t_F is the thin film thickness, while $\sigma = \hat{x}\times\hat{z}$ is the spin current direction, where $\hat{x}$ and $\hat{z}$ are unit-vectors in the conduction electron flow and out-of-plane directions. Here, the conduction electron flows along the $+x$ direction, which causes the spin current to be directed in the $-y$-direction. By substituting Equation 3-4 into Equation 3-2, the force density ($\mathbf{f}_{SH}$) for the spin Hall effect is expressed as:

$$\mathbf{f}_{SH} = -\frac{\hbar\theta_H j}{2et_F}\left(\left(m_z\frac{\partial m_x}{\partial x} - m_x\frac{\partial m_z}{\partial x}\right)\hat{\mathbf{x}} + \left(m_z\frac{\partial m_x}{\partial y} - m_x\frac{\partial m_z}{\partial y}\right)\hat{\mathbf{y}}\right) \qquad \text{Equation 3-5}$$

where m_i is the normalized magnetization in each of the cartesian coordinates. The equation shows that $\mathbf{f}_{SH}$ depends only on the x- and z-magnetization configuration of the system. The magnetization configuration of skyrmions can then be described by [33]:

$$M = \begin{pmatrix} \cos(\phi+q)\ \mathrm{sech}\left(\frac{r-c}{R}\right) \\ \sin(\phi+q)\ \mathrm{sech}\left(\frac{r-c}{R}\right) \\ p\tanh\left(\frac{r-c}{R}\right) \end{pmatrix} M_s, \qquad \text{Equation 3-6}$$

$$R = \sqrt{A/K}\,, \qquad \text{Equation 3-7}$$

where c is the skyrmion radius, R is the skyrmion steepness while A and K are the exchange stiffness and the crystalline anisotropy constants of the material, respectively. q is the phase of the skyrmion and determines the skyrmion type; a Néel skyrmion is formed at $\{0,\pi\}$, while a Bloch skyrmion is formed at $\pm\frac{\pi}{2}$. $p = \pm 1$ is the polarity of the skyrmion and describes the direction of the skyrmion z-magnetization outside the skyrmion core. Together, q and p describe the skyrmion type.

Substituting Equation 3-6 into Equation 3-5 in cylindrical coordinates:

$$\mathbf{F}_{SHE}=-p\frac{\hbar M_s\theta_H j}{2et_F}\left(\left(\begin{array}{l}-\int_0^R\left(\frac{r}{R}\operatorname{sech}\left(\frac{r-c}{R}\right)\tanh^2\left(\frac{r-c}{R}\right)\right)dr\int_0^{2\pi}\cos^2\left(\phi+q\right)d\phi\\+\int_0^R\left(\operatorname{sech}\left(\frac{r-c}{R}\right)\tanh\left(\frac{r-c}{R}\right)\right)dr\int_0^{2\pi}\sin^2\left(\phi+q\right)d\phi\\-\int_0^R\left(\frac{r}{R}\operatorname{sech}^3\left(\frac{r-c}{R}\right)\right)dr\int_0^{2\pi}\cos^2\left(\phi+q\right)d\phi\end{array}\right)\hat{\mathbf{x}}+\left(\begin{array}{l}-\int_0^R\left(\frac{r}{R}\operatorname{sech}\left(\frac{r-c}{R}\right)\tanh^2\left(\frac{r-c}{R}\right)\right)dr\int_0^{2\pi}\cos\left(\phi+q\right)d\phi\sin\left(\phi+q\right)d\phi\\-\int_0^R\left(\operatorname{sech}\left(\frac{r-c}{R}\right)\tanh\left(\frac{r-c}{R}\right)\right)dr\int_0^{2\pi}\cos\left(\phi+q\right)d\phi\sin\left(\phi+q\right)d\phi\\-\int_0^R\left(\frac{r}{R}\operatorname{sech}^3\left(\frac{r-c}{R}\right)\right)dr\int_0^{2\pi}\cos\left(\phi+q\right)d\phi\sin\left(\phi+q\right)d\phi\end{array}\right)\hat{\mathbf{y}}\right)$$

Equation 3-8

By performing the integration over the ϕ angle, the SHE force can be simplified to:

$$\mathbf{F}_{SHE}=-\pi p\frac{\hbar\theta_H j}{2et_F}\left(\int_0^\infty\left(\operatorname{sech}\left(\frac{r-c}{R}\right)\tanh\left(\frac{r-c}{R}\right)-\frac{r}{R}\operatorname{sech}\left(\frac{r-c}{R}\right)\right)dr\right)\left(\cos q\hat{\mathbf{x}}-\sin q\hat{\mathbf{y}}\right)$$

Equation 3-9

which shows that the direction of the force from the SHE depends only on the *q* and *p* of the skyrmion. Fig. 1 shows the magnetization texture generated from Equation 3-6 and the corresponding $\mathbf{f}_{SH}$ acting on the skyrmion. For Néel type skyrmions, the $\mathbf{F}_{SHE}$ cancels out along the *y*-direction but a net $\mathbf{F}_{SHE}$ along the *x*-direction is present. The resulting propagative force is then purely in the direction of the current flow. We find that for all the skyrmion types considered, $\mathbf{F}_{SHE}$ always acts along either the *x*- and *y*-axis. Another observation is the lack of a radial symmetry in the force density which could distort the skyrmion magnetization if the applied spin currents are too large. Accordingly, care should be taken in applying Equation 3-9 in the limit of large SHE forces. Fortunately, for the current densities considered in this work and most other experimental works at ~10^{11} Am^{-2}, the distortion was found to have minimal impact on the magnetization.[34]

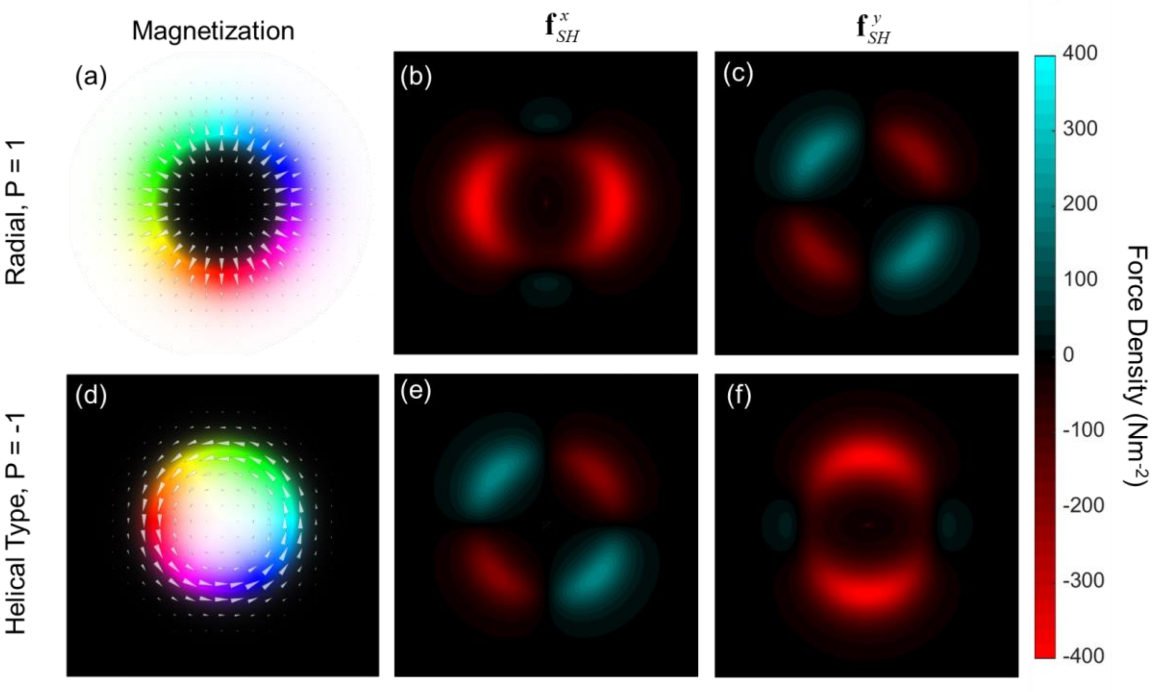

Figure 3-1 (a, d) Magnetization configuration of skyrmions generated analytically from Equation 3-5. The colours represent in-plane magnetization while their brightness represents the out-of-plane magnetization. (b-f**)** Force density acting on skyrmions resolved along the cartesian axes.

The skyrmion shape parameters *p* and *q* sets the direction of the SHE forces but does not affect its amplitude. On the other hand, the parameters *R* and *c* are part of the integral in Equation 3-9 and affects the force amplitude. By solving Equation 3-9 numerically with various *R* and *c* values, the relationship between *R*, *c* and $|\mathbf{F}_{SHE}|$ is determined, as shown in Figure 3-2. A simple visual examination reveals that the steepness *R* has little if any effects on $|\mathbf{F}_{SHE}|$. Although the integral does not set any limits to the values of *c* and *R*, unrealistic conditions such as *R*>*c* would generate magnetization profiles that are physically impossible. Their corresponding $|\mathbf{F}_{SHE}|$ would therefore also be erroneous (see bottom right corner of Figure 3-2). Otherwise, it can be said that the $|\mathbf{F}_{SHE}|$ depends only on the radius *c* of the skyrmion.

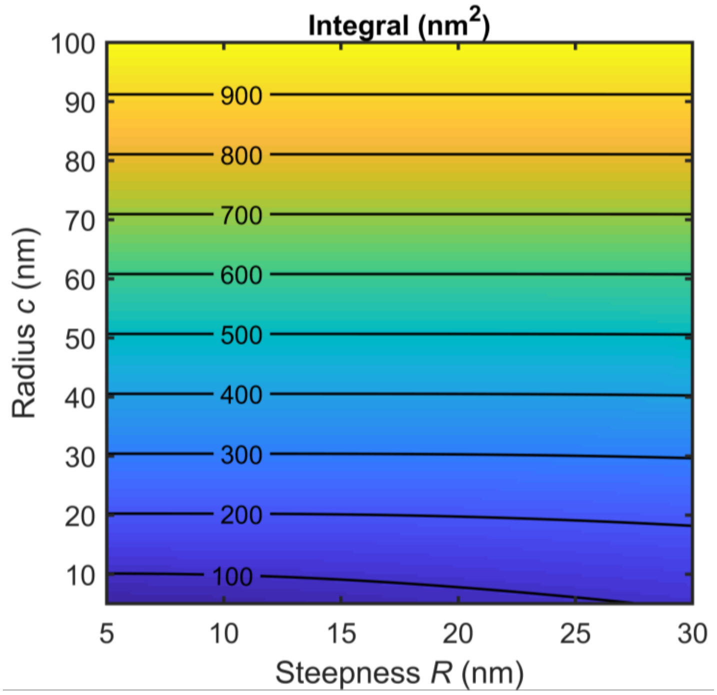

Figure 3-2 Contour plot of the force density integral versus the skyrmion wall steepness R and skyrmion radius c. The integral is calculated from Eq. (8).

Although the integral in Equation 3-9 can be solved analytically, the resulting expression is complex and unwieldy. Thankfully, the integral has an almost linear dependence with c, such that a linear fit can be used. Substituting the fitted equation into Equation 3-9, we get:

$$\mathbf{F}_{SHE} = p\frac{\hbar\theta_H j}{2e}\left(\pi^2 c\right)\left(\cos q\hat{\mathbf{x}} - \sin q\hat{\mathbf{y}}\right) \qquad \text{Equation 3-10}$$

3.3 Modified Thiele Equation

To get the skyrmion velocities, $\mathbf{F}_{SHE}$ is added to the Thiele equation, resulting in:

$$0 = \mathbf{G}\times\mathbf{v} + D\alpha\mathbf{v} + \frac{\gamma}{M_s t_F}\mathbf{F}_{SHE} \qquad \text{Equation 3-11}$$

which when resolved into the parallel and perpendicular components, the following is obtained:

$$v_{\parallel} = -\frac{\alpha D}{G^2 + \alpha^2 D^2}\frac{\gamma}{M_s t_F}\left|\mathbf{F}_{SHE}\right| \qquad \text{Equation 3-12}$$

$$v_{\perp} = -\frac{G}{\alpha D} v_x = \frac{G}{G^2 + \alpha^2 D^2} \frac{\gamma}{M_s t_F} \left| \mathbf{F}_{SHE} \right| \qquad \text{Equation 3-13}$$

where $G = 4\pi$ is the magnitude of the gyrocoupling vector.

Due to the skyrmion Hall effect, skyrmions rarely move in the direction of the applied force. The skyrmion Hall effect arises from the interplay between the various forces.[29] Although there are only three forces acting on a skyrmion, the direction of the forces can be quite complex. The first term in Equation 3-11 is the gyrotropic force which acts perpendicularly to the velocity, the second term is the dissipative force which acts opposite to the velocity. The dissipative force can be seen as a form of drag acting on the skyrmion, mainly arising from the Gilbert damping parameter. The third term is the driving force, which may be caused by SHE or any other types of forces. At equilibrium, all the forces must cancel out. Figure 3-3 shows the forces acting on the skyrmion.

To quickly determine the skyrmion velocity direction, the skyrmion Hall angle θ_{Sk}, which is the angle between the force vector and velocity vector can be used. θ_{Sk} is determined by material parameters and the skyrmion number and is given by taking the ratio between $v_{\perp}$ and $v_{\parallel}$:

$$\theta_{Sk} = \tan^{-1}\left(\frac{G}{\alpha D} \right) \qquad \text{Equation 3-14}$$

Given the skyrmion configurations studied, $\mathbf{F}_{SHE}$ is always along one of the cartesian axes, depending on *p* and *q*. It is then possible to quickly derive the skyrmion velocity.

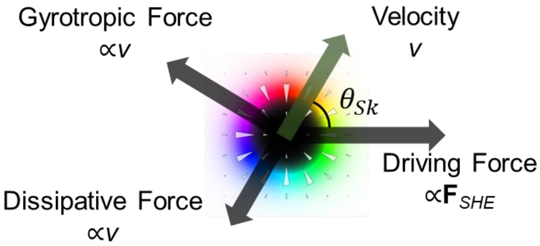

Figure 3-3 Illustration of the effective forces acting on a $(\pi, 1)$ skyrmion when a spin Hall force is applied. Not drawn to scale.

The other effective field exerted by the spin-orbit torque, the Rashba field (H_R), is expressed by:

$$\mathbf{H}_R = \frac{\alpha_R jP}{\mu_B M_s}\boldsymbol{\sigma} \,, \qquad \text{Equation 3-15}$$

where α_{R} is the Rashba parameter that is averaged over the magnetic film thickness, μ_{B} is the Bohr magneton and P is the polarization of the carries in the ferromagnetic layer. In contrast to the magnetization-dependent field from the SHE, the Rashba effect only creates a constant field throughout the ferromagnetic film. Therefore, instead of driving the skyrmion, the Rashba field only creates a change in the magnetization configuration of the skyrmion. Although the altered magnetization configuration will affect the calculated $\mathbf{F}_{SHE}$, the change is negligible as compared to the other effective fields[35].

3.4 Micromagnetic Validation

To validate our model, micromagnetic simulations were performed and compared against the analytical calculations. The MuMax3 software was used for the micromagnetic simulations in this work.[28] The considered geometry was chosen to resemble an infinite ultrathin film with a simulation area of 256 nm × 256 nm × 1 nm discretized into 1 nm cubes and a periodic boundary condition applied along the *x*- and *y*-axis. The material parameters were chosen to be similar to that of a Pt/Co multilayer films,[36] as shown in Table 3-1. A pure spin current was assumed for the simplicity of conversion between charge current and spin current.

Parameter	Value
Saturation magnetization (M_s)	580 kA/m
Gilbert damping (α)	0.1
Exchange stiffness (A_{ex})	15 pJ/m
Interfacial DMI (D)	3 mJ/m^2
Uniaxial anisotropy (K_u)	700 kJ/m^3
Spin Hall angle (θ_{SH})	1

Table 3-1 Material parameters used for the micromagnetic simulations in this chapter. The parameters were chosen to be similar to that of Co/Pt.[36]

In the first scenario, the dependence of $\mathbf{F}_{SHE}$ on *c* was checked. A Néel type skyrmion (q = 0, p = -1) is driven by a pure spin current of amplitude 5×10^{10} Jm^{-2}. The skyrmion radius *c* was varied by changing the applied magnetic field from -20 mT to 200 mT in steps of 10 mT. The skyrmion speed was then calculated based on the total displacement over 2 ns. The time span considered is sufficiently long such that skyrmion inertia can be ignored.[37] Analytical calculations were performed by using Equation 3-12 and Equation 3-13. An excellent agreement between the micromagnetic simulations and model was obtained, as shown in Figure 3-4(a). To validate our omission of R in Equation 3-10, a second scenario was considered, where the steepness was modified by increasing the exchange stiffness from 15 pJm^{-1} to 18 pJm^{-1}. The modification would have decreased the steepness by a factor of $\sqrt{18/15}$. However, Figure 3-4(a) shows that the change in R has an imperceptible effect on the skyrmion speed. In Figure 3-4(b), the model was demonstrated to be robust against changes in saturation magnetization and provides an accurate prediction over a wide skyrmion size range.

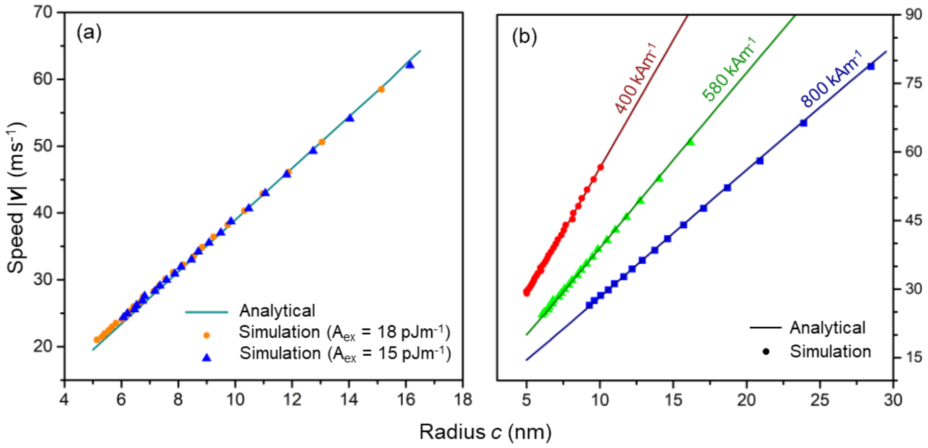

Figure 3-4 Plot of skyrmion speed versus radius with data generated analytical and by means of micromagnetics. (a) The skyrmion radius from the latter was tuned by an applied magnetic field. The skyrmion shape was modified by changing the exchange stiffness used for micromagnetics. (b) The saturation magnetization was varied.

The skyrmion motion direction was found to have a high degree of symmetry as a function of p and q. With two possible values for p (1, -1) and four possible values for q $(0,\pm\frac{\pi}{2},\pi)$, a total of eight skyrmion types can be formed. Under the same spin Hall effect, each skyrmion type experiences a driving force that is of the same amplitude but of a different direction, as predicted by Equation 3-10. In Figure 3-5, the x- and y-velocity for each skyrmion type is plotted with the star symbols. Due to the excellent agreement between the analytical calculations and micromagnetics, only the analytical data is shown. An observation here is that the Bloch skyrmions tend to be driven along the axis of the conduction current (x-axis in this case) while the Néel skyrmions prefer to be driven in the y-

axis. Thus, a unique value proposition is presented by Bloch skyrmions; they can be driven by the spin Hall effect with a much lower transverse angle as compared to their Néel brethren.

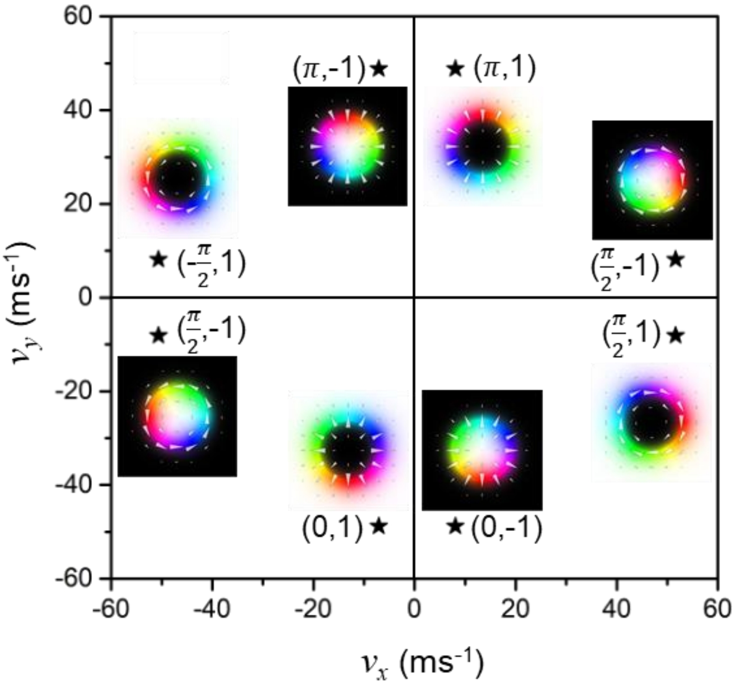

Figure 3-5 Plot of *y*-versus *x*-velocity generated analytically from Eq. 11. The velocities of all possible skyrmion configurations are marked with a star symbol with their magnetization profile shown beside. Also shown beside is the phase and polarity (q, p) of each skyrmion.

3.5 Skyrmion transport in nanowire geometries

Our model predicts a serious challenge for skyrmion-based magnetic devices. While semiconductor devices typically run at higher speeds and efficiencies when scaled down, we have just shown that skyrmions are slowed significantly when they are shrunk. Further, at the limit of $c \rightarrow 0$, skyrmions can no longer be driven by SOTs. Unfortunately, the same grim prediction is also true for skyrmions on synthetic antiferromagnets and antiferromagnets that have been touted as the future of skyrmionics [38-40]. In modelling such vanishing-moment skyrmions [25, 41], the systems are considered as two separate spin lattices that are mutually antiferromagnetically-coupled and their combined dynamics is described by the sum of the forces acting on the individual sublattices. It can then be understood that the combined force also does not scale well with *c*.

To overcome the poor scalability, the correct skyrmion types should be used. Using the proposed model, we show that the choice of skyrmion types may be counter-intuitive but can amplify or diminish the skyrmions' velocity. Figure 3-6 superimposes the trajectory of two different skyrmion types driven by a SOT in a confined nanowire of 192 nm$\times$60 nm. Each skyrmion trajectory is generated by applying a spin Hall current of 1×10^{10} Am^{-2}. Both skyrmions start at the same position on the left marked with blue crosses with a similar initial speed but the Néel skyrmion accelerates while the Bloch skyrmion decelerated to a halt. This is surprising given that Bloch skyrmions have a velocity direction that is very close the direction of the conduction current. Therefore, it is apparent that the transverse velocity due to the gyrotropic force plays a critical role in determining the skyrmion velocity in finite geometries. Several studies in the past have revealed a similar phenomenon but with spin transfer torques as the main driving force.[42, 43]

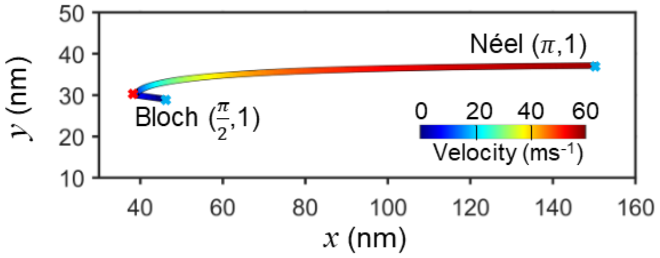

Figure 3-6 Displacement of the two different skyrmions types under the same spin Hall current of $1\times10^{10}\,\mathrm{Am}^{-2}$ after 3 ns. The velocity at each displacement point is represented by the line colour. The starting and ending points of the trajectories are marked by red and blue crosses, respectively.

The counterintuitive phenomena can be explained in terms of the forces acting on the skyrmion. Figure 3-7 shows the direction and magnitude of the forces acting on the skyrmions such as the gyrotropic force $\mathbf{F}_\mathrm{G}$, dissipative force $\mathbf{F}_\mathrm{D}$, and also the repulsion force $\mathbf{F}_\mathrm{R}$ in nanowire geometries. To obtain such a diagram, $\mathbf{F}_\mathrm{SHE}$ is first plotted. Then, $\mathbf{F}_\mathrm{G}$ and $\mathbf{F}_\mathrm{D}$ can be added with the condition that $\mathbf{F}_\mathrm{G} \perp \mathbf{F}_\mathrm{D}$ and that all forces must cancel out. Finally, $\mathbf{v}$ is determined from the condition that $\mathbf{v} \parallel -\mathbf{F}_\mathrm{D}$. In infinite planes, the result is the same as Figure 3-5.

However, in nanowire geometries, the transverse repulsive force $\mathbf{F}_\mathrm{R}$ is exerted by the edges of the nanowire to keep the skyrmion centred.[44] $\mathbf{F}_\mathrm{R}$ significantly impacts the dynamics of the system. For the Néel skyrmion, the upwards velocity results in a greater downwards ($-y$) $\mathbf{F}_\mathrm{R}$ which results in the skyrmion velocity increasing but having a lower transverse direction. At equilibrium, the skyrmion must have a velocity in the direction of the nanowire; $\mathbf{F}_\mathrm{R}$ would need to have a magnitude roughly 6 times larger than $\mathbf{F}_\mathrm{SHE}$ such that it's downwards force can completely negate the transverse velocity component. The massive increase in velocity can be attributed to $\mathbf{F}_R$.

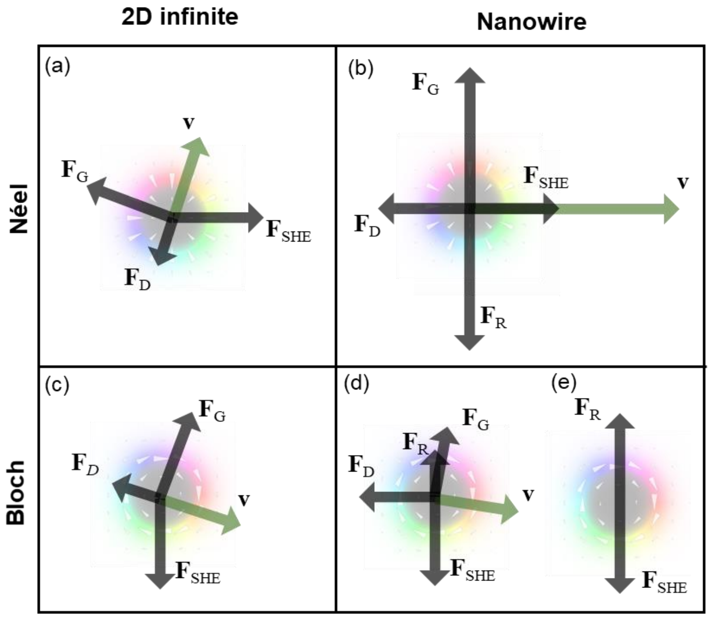

Figure 3-7 Forces acting on a Néel (π,1) and Bloch ($\frac{\pi}{2}$,1) skyrmions on 2D infinite planes and on nanowire geometries. The nanowire axis in the *x*-direction. In (d), the effective forces are shown at the onset of $\mathbf{F}_{SHE}$ and (e) at equilibrium after about 3 ns. Forces are not drawn to scale.

By considering the velocity due to the SHE ($\mathbf{v}_{SHE}$) and due to $\mathbf{F}_R$ ($\mathbf{v}_R$), it is possible to derive the net velocity ($\mathbf{v}_{eff}$) of the skyrmion in a finite nanowire, purely from vector sums, as shown in Figure 3-8(a). Applying the trigonometric relations, $\mathbf{v}_{eff}$ can be expressed in this form:

$$\mathbf{v}_{eff} = \mathbf{v}_{SHE}\cos\theta_{Sk} + \mathbf{v}_{SHE}\sin\theta_{Sk}\cdot\tan\theta_{Sk}$$

Equation 3-16

For parameters used in this study, a very significant amplification in the skyrmion velocity is obtained, where $\sin\theta_{Sk}\cdot\tan\theta_{Sk} = 6.23$.

For the Bloch skyrmions to fulfil the condition that the skyrmion has no net transverse velocity, the only solution is that $\mathbf{F}_R$ cancels $\mathbf{F}_{SHE}$ completely, as shown in Figure 3-7(d-e). This is a consequence of $\mathbf{F}_R$ being antiparallel to $\mathbf{F}_{SHE}$; as the skyrmion drifts closer to the edge, $\mathbf{F}_R$ increases and negates $\mathbf{F}_{SHE}$. At equilibrium, $\mathbf{F}_R = -\mathbf{F}_{SHE}$ and skyrmion motion is stopped.

The results presented suggests that a constructive $\mathbf{v}_R$ can be generated at no cost to increase $\mathbf{v}_{eff}$. . It is then tempting to change the electric current direction to push the skyrmion more strongly against the edge, i.e. $\mathbf{v}_{\mathrm{SHE}}$ points closer to $+y$ direction and increases $\mathbf{v}_{\mathrm{R}}$. Changing the electric current direction has been proposed thus far to reduce the skyrmion Hall angle, such that $\mathbf{v}_{\mathrm{SHE}}$ is in the direction of the nanowire.[45] However, in our case, the intention is to increase the skyrmion speed by setting $\mathbf{v}_{\mathrm{SHE}}$ perpendicular to the nanowire in order to maximize $\mathbf{v}_{\mathrm{R}}$. In Figure 3-8, the velocity vectors are illustrated for (a) the default case and (b) electric current rotated by an angle δ.

$$\mathbf{v}_{eff} = \mathbf{v}_{SHE} \cdot \cos\left(\theta_{Sk} + \delta\right) + \mathbf{v}_{SHE} \cdot \sin\left(\theta_{Sk} + \delta\right) \cdot \tan\left(\theta_{Sk}\right)$$

Equation 3-17

where δ is introduced as a deviation angle for the electric current, as compared to the x-axis. The first term originates from the parallel component of $\mathbf{v}_{\mathrm{SHE}}$ while the second term is the additional force granted by $\mathbf{v}_{\mathrm{R}}$.

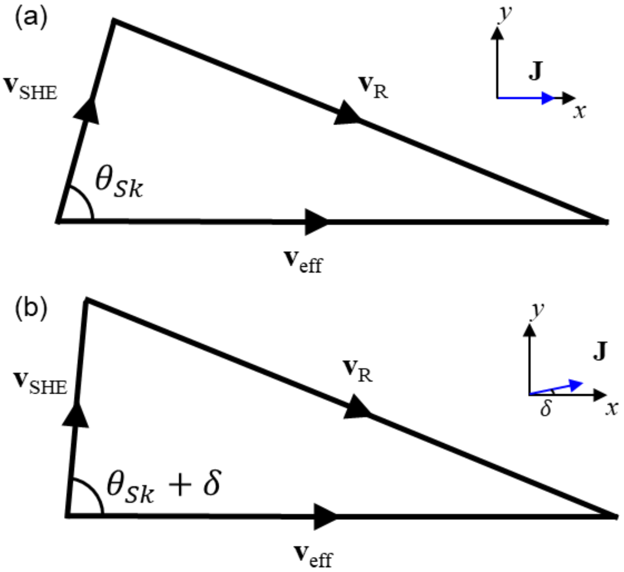

Figure 3-8 Illustration of the skyrmion velocity vectors (a) when the driving current is in the direction of the nanowire and (b) when the driving current is offset by δ.

With Equation 3-17, the x velocity of a skyrmion under different δ can be evaluated and compared to micromagnetics. While the force provided by $\mathbf{v}_{\mathrm{R}}$ is increased, the decrease in the x-component of $\mathbf{v}_{\mathrm{SHE}}$ decays even faster. Unfortunately, the velocity peak occurs at $\delta = 0$. Performing the differentiation of $\mathbf{v}_{\mathrm{eff}}$ and it to zero, we obtain:

$$\frac{d\mathbf{v}_{eff}}{d\delta} = \mathbf{v}_{SHE} \cos\left(\theta_{Sk} + \delta\right) \cdot \tan\left(\theta_{Sk}\right) - \mathbf{v}_{SHE} \sin\left(\theta_{Sk} + \delta\right)$$
$$0 = -\sin\left(\theta_{Sk} + \delta\right) - \cos\left(\theta_{Sk} + \delta\right) \cdot \tan\left(\theta_{Sk}\right)$$

Equation 3-18

It is thus clear that the maximum forward driving force occurs at $\delta = 0$ and that altering δ provides no benefit. The relation between velocity and δ is shown in Figure 3-9 where Equation 3-17 was used to plot the analytical data. The difference between the two data sets arises from the compression of the skyrmion which is not considered in Equation 3-17.

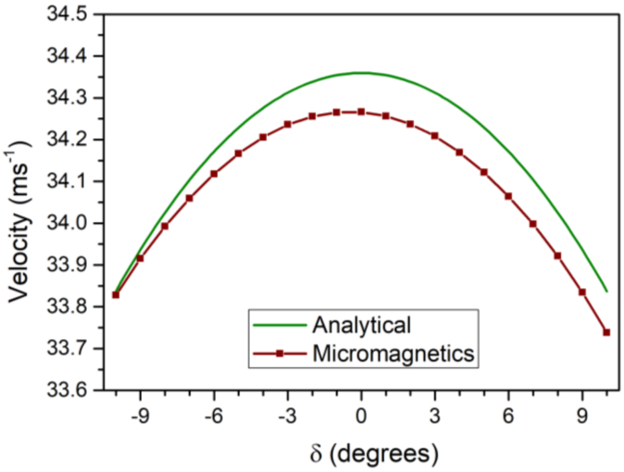

Figure 3-9 Plot of skyrmion *x*-velocity against current deviation angle.

In this chapter, we have shown that in a system where spin-orbit coupling is prevalent, only the torque from the spin Hall effect contributes to the dynamics of the skyrmion. In steady-state, the spin-orbit torque can be regarded as a force whose magnitude depends purely on the skyrmion size and whose direction depends on the skyrmion type supported by the system. While several pioneering works have modelled skyrmion dynamics under spin currents, their predictions are not always consistent, and their mathematical form can be complex [46, 47]. In contrast, our model is well-corroborated with micromagnetics over a wide range of material parameters and yields a simple mathematical form. From there, we predicted a serious scalability challenge for skyrmion-based devices, where truly atomic-scale skyrmions would barely be driven by the spin Hall effect. Not all is doom and gloom, as we further uncovered the importance of the gyrotropic force in amplifying the skyrmion Hall force. In our system, the skyrmion was able to move six times faster due to this phenomenon. Therefore, given the significant consequences, the model and analysis provided in this work serve as an important starting point for the engineering and design of skyrmion-based devices.

References

1. A. A. Thiele, *Physical Review Letters*, 1973, **30**, 230-233.
2. J. Zhang, C. Garg, T. Phung, C. Rettner, B. P. Hughes, S.-H. Yang, Y. Jiang and S. S. P. Parkin, *Nano Letters*, 2018, **18**, 4074-4080.
3. S.-h. C. Baek, V. P. Amin, Y.-W. Oh, G. Go, S.-J. Lee, G.-H. Lee, K.-J. Kim, M. D. Stiles, B.-G. Park and K.-J. Lee, *Nature materials*, 2018, **17**, 509-513.
4. C.-F. Pai, M. Mann, A. J. Tan and G. S. D. Beach, *Physical Review B*, 2016, **93**.
5. Y. C. Lau, D. Betto, K. Rode, J. M. Coey and P. Stamenov, *Nature Nanotechnology*, 2016, **11**, 758-762.
6. N. Mikuszeit, O. Boulle, I. M. Miron, K. Garello, P. Gambardella, G. Gaudin and L. D. Buda-Prejbeanu, *Physical Review B*, 2015, **92**.
7. G. Yu, P. Upadhyaya, Y. Fan, J. G. Alzate, W. Jiang, K. L. Wong, S. Takei, S. A. Bender, L. T. Chang, Y. Jiang, M. Lang, J. Tang, Y. Wang, Y. Tserkovnyak, P. K. Amiri and K. L. Wang, *Nature Nanotechnology*, 2014, **9**, 548-554.
8. M. Cubukcu, O. Boulle, M. Drouard, K. Garello, C. O. Avci, I. M. Miron, J. Langer, B. Ocker, P. Gambardella and G. Gaudin, *Applied Physics Letters*, 2014, **104**, 042406.
9. M. Hayashi, J. Kim, M. Yamanouchi and H. Ohno, *Physical Review B*, 2014, **89**, 144425.
10. E. Martinez, S. Emori and G. S. D. Beach, *Applied Physics Letters*, 2013, **103**, 072406.
11. A. V. Khvalkovskiy, V. Cros, D. Apalkov, V. Nikitin, M. Krounbi, K. A. Zvezdin, A. Anane, J. Grollier and A. Fert, *Physical Review B*, 2013, **87**, 020402.
12. J. Sinova, S. O. Valenzuela, J. Wunderlich, C. H. Back and T. Jungwirth, *Reviews of Modern Physics*, 2015, **87**, 1213-1260.
13. J. E. Hirsch, *Physical Review Letters*, 1999, **83**, 1834-1837.
14. A. Manchon, H. C. Koo, J. Nitta, S. M. Frolov and R. A. Duine, *Nature materials*, 2015, **14**, 871.
15. I. Mihai Miron, G. Gaudin, S. Auffret, B. Rodmacq, A. Schuhl, S. Pizzini, J. Vogel and P. Gambardella, *Nature materials*, 2010, **9**, 230.
16. I. M. Miron, T. Moore, H. Szambolics, L. D. Buda-Prejbeanu, S. Auffret, B. Rodmacq, S. Pizzini, J. Vogel, M. Bonfim, A. Schuhl and G. Gaudin, *Nature materials*, 2011, **10**, 419.
17. A. Fert, V. Cros and J. Sampaio, *Nature Nanotechnology*, 2013, **8**, 152-156.
18. A. Soumyanarayanan, M. Raju, A. L. Gonzalez Oyarce, A. K. C. Tan, M.-Y. Im, A. P. Petrović, P. Ho, K. H. Khoo, M. Tran, C. K. Gan, F. Ernult and C. Panagopoulos, *Nature materials*, 2017, **16**, 898.

19. B. Zeinali, J. K. Madsen, P. Raghavan and F. Moradi, 2017.

20. G. Prenat, K. Jabeur, G. Di Pendina, O. Boulle and G. Gaudin, in *Spintronics-based Computing*, eds. W. Zhao and G. Prenat, Springer International Publishing, Cham, 2015, DOI: 10.1007/978-3-319-15180-9_4, pp. 145-157.

21. F. Oboril, R. Bishnoi, M. Ebrahimi and M. B. Tahoori, *IEEE Transactions on Computer-Aided Design of Integrated Circuits and Systems*, 2015, **34**, 367-380.

22. I. Makhfudz, B. Krüger and O. Tchernyshyov, *Physical Review Letters*, 2012, **109**, 217201.

23. X. Wang, W. L. Gan, J. C. Martinez, F. N. Tan, M. B. A. Jalil and W. S. Lew, *Nanoscale*, 2018, **10**, 733-740.

24. W. Jiang, X. Zhang, G. Yu, W. Zhang, X. Wang, M. Benjamin Jungfleisch, J. E. Pearson, X. Cheng, O. Heinonen, K. L. Wang, Y. Zhou, A. Hoffmann and S. G. E. te Velthuis, *Nature Physics*, 2017, **13**, 162-169.

25. C. C. I. Ang, W. Gan and W. S. Lew, *New Journal of Physics*, 2019, **21**.

26. I. Purnama, W. L. Gan, D. W. Wong and W. S. Lew, *Scientific Reports*, 2015, **5**, 10620.

27. A. Thiaville, Y. Nakatani, J. Miltat and Y. Suzuki, *Europhysics Letters*, 2005, **69**, 990-996.

28. A. Vansteenkiste, J. Leliaert, M. Dvornik, M. Helsen, F. Garcia-Sanchez and B. Van Waeyenberge, *Aip Advances*, 2014, **4**, 107133.

29. J. Iwasaki, M. Mochizuki and N. Nagaosa, *Nature Nanotechnology*, 2013, **8**, 742-747.

30. N. Nagaosa and Y. Tokura, *Nature Nanotechnology*, 2013, **8**, 899-911.

31. C. Schütte, J. Iwasaki, A. Rosch and N. Nagaosa, *Physical Review B*, 2014, **90**, 174434.

32. S. Emori, E. Martinez, K.-J. Lee, H.-W. Lee, U. Bauer, S.-M. Ahn, P. Agrawal, D. C. Bono and G. S. D. Beach, *Physical Review B*, 2014, **90**, 184427.

33. N. Romming, A. Kubetzka, C. Hanneken, K. von Bergmann and R. Wiesendanger, *Physical Review Letters*, 2015, **114**, 177203.

34. S. Woo, K. M. Song, H.-S. Han, M.-S. Jung, M.-Y. Im, K.-S. Lee, K. S. Song, P. Fischer, J.-I. Hong, J. W. Choi, B.-C. Min, H. C. Koo and J. Chang, *Nature Communications*, 2017, **8**, 15573.

35. Q. Y. Wong, C. Murapaka, W. C. Law, W. L. Gan, G. J. Lim and W. S. Lew, *Physical Review Applied*, 2019, **11**, 024057.

36. A. Barman, S. Wang, O. Hellwig, A. Berger, E. E. Fullerton and H. Schmidt, *Journal of Applied Physics*, 2007, **101**, 09D102.

37. A. A. Donovan and B. W. Kernighan, *The Go programming language*, Addison-Wesley Professional, 2015.

38. V. Baltz, A. Manchon, M. Tsoi, T. Moriyama, T. Ono and Y. Tserkovnyak, *Reviews of Modern Physics*, 2018, **90**, 015005.
39. R. Tomasello, V. Puliafito, E. Martinez, A. Manchon, M. Ricci, M. Carpentieri and G. Finocchio, *Journal of Physics D: Applied Physics*, 2017, **50**, 325302.
40. X. Zhang, Y. Zhou and M. Ezawa, *Scientific Reports*, 2016, **6**, 24795.
41. J. Barker and O. A. Tretiakov, *Physical Review Letters*, 2016, **116**, 147203.
42. J. C. Martinez, W. S. Lew, W. L. Gan and M. B. A. Jalil, *Journal of Magnetism and Magnetic Materials*, 2018, **465**, 685-691.
43. J. Iwasaki, W. Koshibae and N. Nagaosa, *Nano Letters*, 2014, **14**, 4432-4437.
44. X. Zhang, G. P. Zhao, H. Fangohr, J. P. Liu, W. X. Xia, J. Xia and F. J. Morvan, *Scientific Reports*, 2015, **5**, 7643.
45. B. Göbel, A. Mook, J. Henk and I. Mertig, *Physical Review B*, 2019, **99**, 020405.
46. K. M. D. Hals and A. Brataas, *Physical Review B*, 2014, **89**, 064426.
47. M. E. Knoester, J. Sinova and R. A. Duine, *Physical Review B*, 2014, **89**, 064425.

Chapter 4 Skyrmion motion under voltage-controlled magnetic anisotropy gradients

Despite the inefficiencies associated with current-induced spin torques, they remain the predominant mode of skyrmion propulsion. In this chapter, we demonstrate numerically that skyrmions can be transported much more efficiently with a voltage-controlled magnetic anisotropy (VCMA) gradient. In this chapter, an analytical model was developed to understand the underlying skyrmion dynamics under a VCMA gradient. The calculations reveal that the repulsive skyrmion-edge interaction not only prevents the skyrmion from annihilating but also generates most of the skyrmion propulsion. Therefore, edge engineering will greatly improve the performance of anisotropy gradient-driven skyrmion devices.[1-3] A multiplexed array of gate electrodes can be used to create discrete anisotropy gradients over a long distance, leading to the formation of a series of translatable skyrmion potential wells. The strong confining potentials allow skyrmions to be transported at a 70% higher packing density. Lastly, we demonstrate that this form of skyrmion propulsion can be implemented on almost any 2D geometry, providing improved versatility over current-induced methods.

4.1 Introduction

Skyrmions are prime candidates as information carriers for next-generation ultra-high density non-volatile memory.[4, 5] To realize such devices, many works on skyrmion dynamics have been performed, especially on skyrmion transport via application of spin-polarized currents.[3, 6-9] However, there are still significant challenges for high-speed current-based manipulation which requires the application of high current densities on the order of 10^{11} A/m^2.[1, 3, 10-12] Under such high current densities, Joule heating significantly increases the device temperature, further leading to device instability. Besides the increased risk of skyrmion annihilation due to the higher thermal fields, works by Sug-Bong Choe *et. al.* and A. Yamaguchi *et. al.* have also shown that temperature can have a strong influence on the propagation speeds of magnetization textures.[13-15] Therefore, it is necessary to develop an energy-efficient skyrmion manipulation technique that reduces the Joule heating.

To increase the efficiency of magnetic devices, many recent scientific endeavours have turned to voltage-controlled magnetic anisotropy (VCMA). The effect relies on the electric field-induced change in the relative occupation of 3d orbitals to alter the magnetic anisotropy.[16-20] Since VCMA is a field-induced effect, they consume much lower energy as compared to the electric current-based methods. By applying a gate voltage across an insulating layer, the magnetic anisotropy of the ferromagnetic layer can be modulated. The VCMA effect has already been shown to be large enough for magnetization switching in magnetic random-access memory devices and for speeding up domain wall transport.[21-29]

In this chapter, a cell size of 1 nm × 1 nm × 0.5 nm was used for micromagnetic simulations. The material parameters are based on the experimentally measured values for Pt/Co thin films.[30, 31] A summary is shown in Table 4-1.

Parameter	Value
Saturation magnetization (M_s)	600 kA/m
Gilbert damping (α)	0.1
Exchange stiffness (A_{ex})	13 pJ/m
Interfacial DMI (D)	3 mJ/m^2
Uniaxial anisotropy (K_u)	800 kJ/m^3

Table 4-1 Summary of material parameters used for the micromagnetic simulations

4.2 Skyrmion dynamics under VCMA gradient in an infinite plane

We first consider the motion of a skyrmion on an unconfined planar skyrmion system under the influence of a magnetic anisotropy gradient. To model the infinite system, periodic boundary conditions were imposed on both *x*-axis and *y*-axis that enables the magnetization to wrap around in both directions and a Néel skyrmion typical of systems with interfacial DMI was used as the starting configuration.[32, 33] The VCMA gradient across a wedged insulating layer was modelled by a gradient in the magnetic anisotropy energy density of $\frac{dK_u}{dx} = 600$ GJ/m^4 along the x-axis. This corresponds to a percentage change of 7.5% over a length of 1 μm. Figure 4-1(a) shows a schematic of the electric field geometry. At the side with a thinner dielectric layer, the charge buildup would result in a high electric field, while at the side with a thicker dielectric layer, the electric field is weaker. The gradual change in the electric field induces a VCMA gradient. Upon the application of the anisotropy gradient, the skyrmion was observed to propagate in a single direction indefinitely.

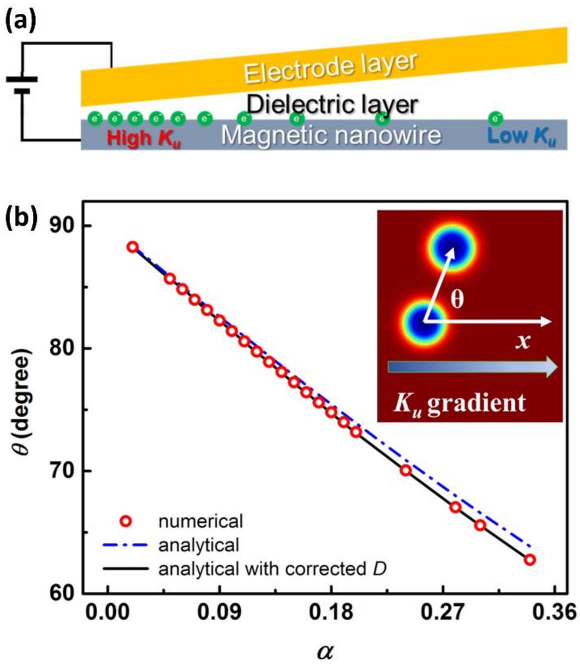

Figure 4-1 (a) Schematic of a voltage-controlled magnetic anisotropy device capable of creating an anisotropy gradient. (b)The deviation angle θ of skyrmion motion to the direction of K_u gradient $\frac{dK_u}{dx} = 600$ GJ/m^4 as a function of the Gilbert damping constant α in a wide plane, in which skyrmion moves at an angle θ with respect to the x-axis. Inset is a snapshot of a skyrmion, which drifted diagonally after a K_u gradient was applied.

Assuming that the skyrmion magnetization profile performs a translation without deformation, the isolated Néel skyrmion can be considered as a rigid point-like particle. The skyrmion dynamics can then be modelled within the framework of the Thiele equation without polarized spin current:[7, 34, 35]

$$\mathbf{G}\hat{z}\times\mathbf{v} - D\alpha\mathbf{v} + \frac{\gamma}{M_s d}\mathbf{F} = 0 \qquad \text{Equation 4-1}$$

$$\mathbf{G} = 2\pi\left[\cos\theta\right]_{\theta(r=0)}^{\theta(r=\infty)}\hat{z} \qquad \text{Equation 4-2}$$

$$\mathbf{F} = -\int_{UC} d^2 r \partial\vec{n}\cdot\frac{\delta E}{\delta n} \qquad \text{Equation 4-3}$$

where $\mathbf{v}$ is skyrmion drift velocity, $\mathbf{G}$ is gyromagnetic coupling vector that depends on the direction of the magnetization in the skyrmion core and far away from the core, D is dissipative force tensor that is dependent on the radial profile of the out-of-plane angle of the skyrmion, α is the Gilbert damping constant. The vector $\mathbf{F}$ is a force acting on skyrmion, originating from an inhomogeneous magnetostatic energy landscape.

The first term of Thiele equation describes the gyrotropic motion of a skyrmion,[6, 36-38] which gives rise to a Hall-like behaviour of magnetic skyrmions (SkHE) which causes them to deviate from the direction of applied stimulus as shown in Figure 4-1(b) inset.[39] The second term is the dissipative force originating from the Gilbert damping while the third term is the driving force from the inhomogeneous energy landscape which is attributed to the magnetic anisotropy gradient. To simplify the Thiele equation, the skyrmion motion is decomposed into the *x*-component and the *y*-component:

$$\hat{x}: \quad Gv_y + D\alpha v_x = \frac{\gamma}{M_s d} F_x \qquad \text{Equation 4-4}$$

$$\hat{y}: \quad Gv_x - D\alpha v_y = 0 \qquad \text{Equation 4-5}$$

where $G = 4\pi$ is the magnitude of the gyrocoupling vector. This leads to the expression for the ratio of v_y and v_x:

$$\tan\theta_{Sk} = \frac{v_y}{v_x} = \frac{G}{\alpha D}. \qquad \text{Equation 4-6}$$

For a Néel-type skyrmion with $\alpha = 0.1$, the calculated skyrmion Hall angle θ_{Sk} of 82° results in mostly transverse motion. Micromagnetic simulations were performed to verify the dependence of skyrmion Hall angle on α. Indeed, a linear relation in Figure 4-1(b) was observed as predicted. However, a discrepancy between the numerical results and the analytical expression (Equation 4-6) exists which increases with α. This difference can be almost completely accounted for by the change of the skyrmion magnetization profile as the skyrmion moves from a region of higher K_u to a region of lower K_u. The resulting change in D can be calculated by numerically integrating the volume magnetization. The dissipative tensor D in Thiele equation can be written as,[40]

$$D_{ij} = \int_{sk} d^2 r \partial_i \mathbf{m} \cdot \partial_j \mathbf{m} = \begin{cases} D & (i,j) = (x,x),(y,y), \\ 0 & \text{otherwise.} \end{cases} \qquad \text{Equation 4-7}$$

In the numerical simulations, D was observed to change as the skyrmions were driven to the lower K_u regions, as shown in Figure 4-2. Therefore, a small difference between the simulated and analytical trajectories will are observed.

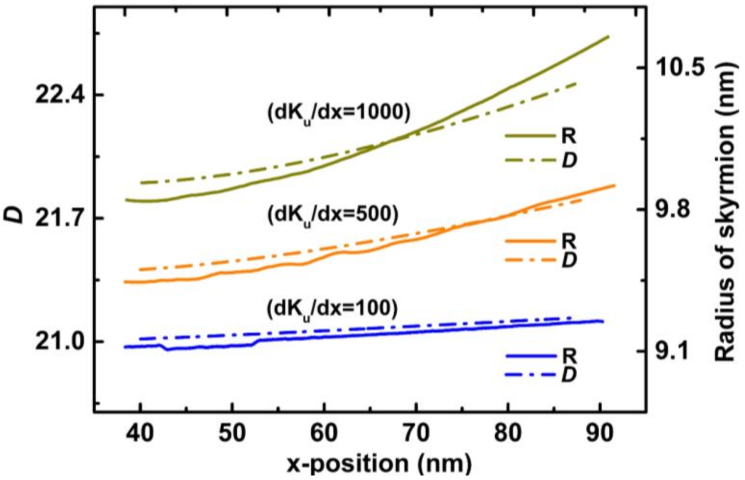

Figure 4-2 Dissipative force tensor and radius at different x-position during skyrmion motion under various Ku gradients.

Figure 4-1(b) shows the relation between the modified *D* and *α*. By introducing this modified *D* back into Equation 4-6, the theoretical calculations match almost exactly with the simulation results. Therefore, we can conclude that the skyrmion Hall angle is determined by α even in the absence of a spin current.

4.3 VCMA gradient-induced skyrmion dynamics in finite systems

Translation invariance on an infinite plane is commonly invoked to argue that a skyrmion velocity is not a function of its position. However, a skyrmion on a finite track is no longer translationally invariant. Therefore, the energy potential from the edges must be considered in a finite system. Over a large range of nanowires width values, the skyrmion is observed to drift towards the edges with an angle of 82° but starts to travel parallel to the edge close to its vicinity and does not annihilate, as shown in Figure 4-3(a). The dependence of trajectory with nanowire width, as shown in Figure 4-3(b), implies that repulsive potential plays a key role to repel a skyrmion from the edges.[41 42]

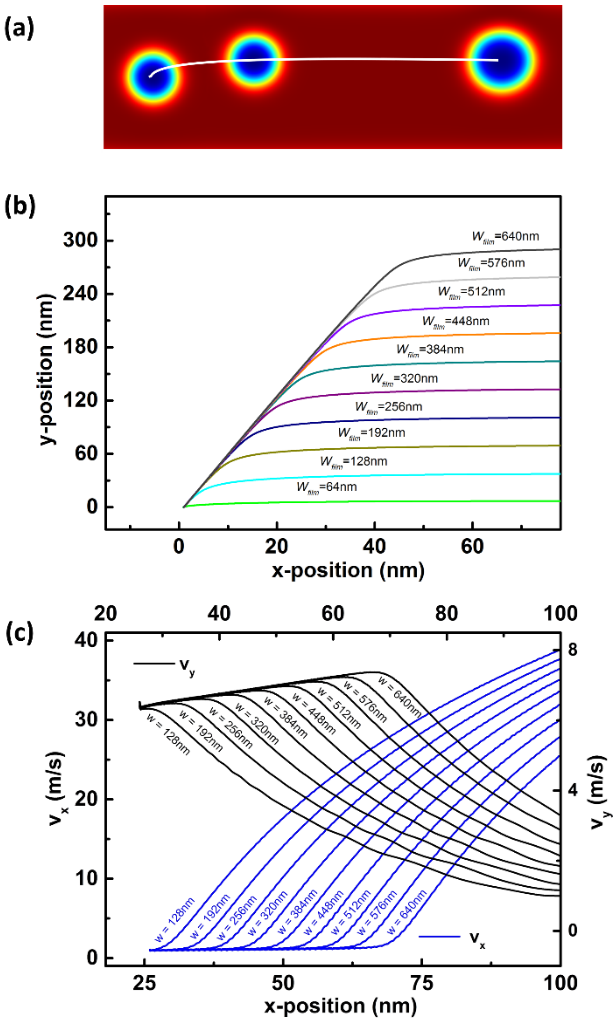

Figure 4-3 Skyrmion motion in nanowire induced by anisotropy energy gradient along the *x*-axis. (a) snapshots of skyrmion motion at 2 ns intervals in a 64 nm wide nanowire. (b) Skyrmion trajectories in nanowires of different widths, from 64 nm to 640 nm, indicating that the skyrmion trajectory is highly dependent on nanowire geometry. (c) The longitudinal and transverse velocities (v_x, v_y), at the different nanowire widths. v_y slows down to almost zero at the end of its displacement along the y-axis, meanwhile, v_x dramatically increases from several m/s to tens of m/s.

As the skyrmion approaches the edges, its motion soon becomes parallel to the nanowire. This leads us to the conclusion that $\mathbf{F}$ in Equation 4-1 must include the repulsive potential if the system is finite. The Thiele equation can be rearranged to express velocity $\mathbf{v}$ as:

$$\mathbf{v} = \frac{\gamma}{(G^2 + D^2\alpha^2)M_s d}\left(D\alpha\mathbf{F} + (\mathbf{G}\times\mathbf{F})\right) \qquad \text{Equation 4-8}$$

As discussed before, $\vec{F}_x$ originates from the inhomogeneous energy attributable to the K_u gradient and can be written as:

$$F_x = -\frac{dE_{K_u}}{dK_u}\frac{dK_u}{dx} \qquad \text{Equation 4-9}$$

$$E_{K_u} = -K_u(\vec{m}\cdot\hat{z})^2 \pi R_{sk}{}^2 d \qquad \text{Equation 4-10}$$

Here E_{K_u} is the anisotropy energy,[43] d is the thickness of the skyrmion system, R_{sk} is the radius of skyrmion. predicts that the decrease of K_u leads to the decrease of energy in the skyrmion system, which is consistent with the observation that skyrmions tend to move to a region of lower K_u. From the above, we can also see that larger anisotropy gradient will create a larger driving force which in turn leads to a higher speed, the trend confirmed by numerical results, as shown in Figure 4-4(a).

In the case of finite nanowire system, the repulsive potential exists in the edge of the skyrmion system leads to a force pushing the skyrmion back to the centre position. At the centre, where y displacement from the centre of the nanowire (Δy) is zero, this force is also zero as expected from the symmetry along the x-axis. However, when the skyrmion is displaced towards the top or bottom edge ($\Delta y \neq 0$), an increased magnetostatic energy creates a repulsive potential from the edges, keeping the skyrmion from approaching the edge.[41, 42, 44]

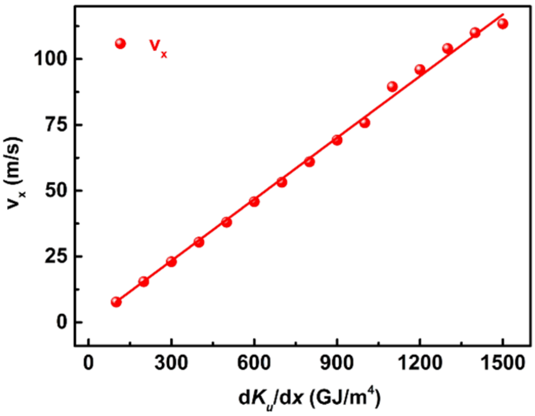

Figure 4-4 (a) Numerically calculated values of saturation velocities v_{xT} vs. $\frac{dK_u}{dx}$, indicating that v_x is directly proportional to $\frac{dK_u}{dx}$.

The change in magnetostatic energy along the y-axis was found by applying a spin-current (7×10^{11} A/m^2) along the x-axis to drive the skyrmion. Under the applied current, the skyrmion experiences a skyrmion Hall effect and drifts in the y-axis. The system's total magnetostatic energy E was then calculated at every y-position as shown in Figure 4-5(a). Since the skyrmion-edge interaction is magnetostatic in nature, E was modelled by the inverse square law:

$$E(y) = A + By^2, \qquad \text{Equation 4-11}$$

where A and B are quadratic fit coefficients. The energy gradient and in turn F_y along the y-axis of a nanowire of width w can be expressed by:

$$F_y = \frac{\partial E_y}{\partial y} = C(x)\Delta y, \qquad \frac{w}{2} - |\Delta y| \geq 20\ nm \qquad \text{Equation 4-12}$$

where $C(x)$ is the magnetostatic interaction coefficient. As F_y is assumed to be purely magnetostatic in nature, the linear relation proposed in Figure 4-5(a) is only valid for small y displacements. At larger displacements, the exchange interaction may play a significant role.[45] When the skyrmion centre is less than 20 nm from the edge, a strong attractive potential is experienced which can cause skyrmion annihilation (see Figure 1-16).

Under a $\frac{dK_u}{dx}$, the skyrmion size also changes due to the difference in K_u. Since the skyrmion is magnetically charged, a larger skyrmion experiences a larger repulsion from the edges. Hence, in a nanowire with $\frac{dK_u}{dx}$, the coefficient $C(x)$ is also a function of x, this relation is shown in Figure 4-5(b). To obtain the function $C(x)$, the change in energy ΔE versus Δy was extracted from numerically calculated data. As expected, $C(x)$ decreases with increasing K_u (decreasing size) as shown in Figure 4-4(b).

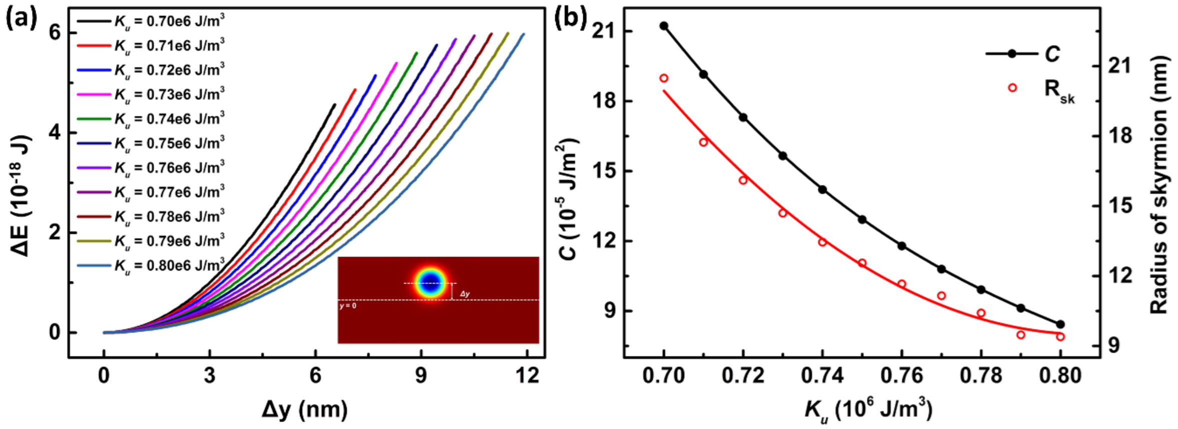

Figure 4-5 (a) Micromagnetic energy as a function of skyrmion displacement along the *y*-axis from the centre of the nanowire with various anisotropy constants. Inset is the schematic diagram of the skyrmion displacement along the *y*-axis. (b) Both *C* and radius of skyrmion depend are a function of K_u. This indicates that *C* increases with the increase of *x*-position in a system with $\frac{dK_u}{dx}$.

In our analysis thus far, we have established that the skyrmion propulsion induced by the anisotropy energy gradient is determined by the interplay between two forces. The first of which is that a driving force originating from an anisotropy energy gradient that can propel the skyrmion along the *x*-axis. Secondly, there is a repulsive force caused by an inhomogeneous magnetostatic energy landscape perpendicular to the edge. By combining the two, a two-dimensional force (F_x, F_y) vector field in the *x*-*y* plane can be generated, as shown in Figure 4-6(a). In a system without SkHE, a skyrmion will move in the +*x* direction monotonically while the edge interaction forms a potential well keeping the skyrmion at the centre of the nanowire. The situation becomes interesting when the force field is transformed into a velocity field by applying Equation 4-8. While the force field is symmetric along the *x*-axis, the SkHE destroys the symmetry in the velocity field. Figure 4-6(b) shows that the velocity field is asymmetric, and the equilibrium trajectory is shifted upwards. In this context, the equilibrium trajectory is defined as the trajectory at which the skyrmion moves in the direction along the nanowire; all other *y*-displacements result in the skyrmion returning to the equilibrium trajectory.

An important consequence of the asymmetry is that the initial skyrmion position can significantly modify the skyrmion trajectory. As shown in Figure 4-6(c), it is possible for the skyrmion to perform a boomerang manoeuvre whenever it is nucleated closer to the bottom edge. This phenomenon results from the strong repulsive potential overpowering the forward propulsion, resulting in an initial backward motion. As the skyrmion passes the centre of the nanowire (Δy = 0 nm), the edge interaction changes in sign and propels the skyrmion forward instead, thus completing the boomerang manoeuvre. However, trajectories of skyrmions at all initial positions still gradually converges towards the equilibrium trajectory. In the equilibrium trajectory, the terminal *x*-velocity v_{xT} can be expressed as:

$$v_{xT} = \frac{\gamma}{M_s d}\frac{F(x)}{D\alpha} = \frac{\gamma \pi m_z{}^2 R_{sk}{}^2}{M_s D\alpha}\frac{dK_u}{dx} \qquad \text{Equation 4-13}$$

Equation 4-13 assumes that the repulsive edge potentials are sufficient to prevent skyrmion from annihilation and shows that the terminal velocity of a skyrmion is proportional to $\frac{dK_u}{dx}$, a conclusion consistent with the numerical result in Figure 4-4(a). The equation also highlights how the material parameters such as D, α and M_s can affect the velocity of skyrmion motion. Meanwhile, the *y*-displacement at which terminal velocity is achieved can be expressed analytically as:

$$\Delta y_T = \frac{\pi R_{sk}{}^2 m_z{}^2 G d}{C(x) D\alpha}\frac{dK_u}{dx} \qquad \text{Equation 4-14}$$

It is easy to see from Equation 4-14 that with a higher $\frac{dK_u}{dx}$, the equilibrium trajectory is shifted upwards. Equation 4-14 also reveals that the maximum velocity is in fact limited by the edge interaction. For a finite system, $\Delta y_T \le (\frac{w}{2} - 20\ \text{nm})$ determines the maximum force along the *y*-axis; skyrmion annihilation would occur readily when the skyrmion centre is less than 20 nm from the edge. A dilemma results, in which a larger anisotropy gradient will increase the skyrmion transport velocity but once the maximum F_y is exceeded, skyrmion annihilation will result.

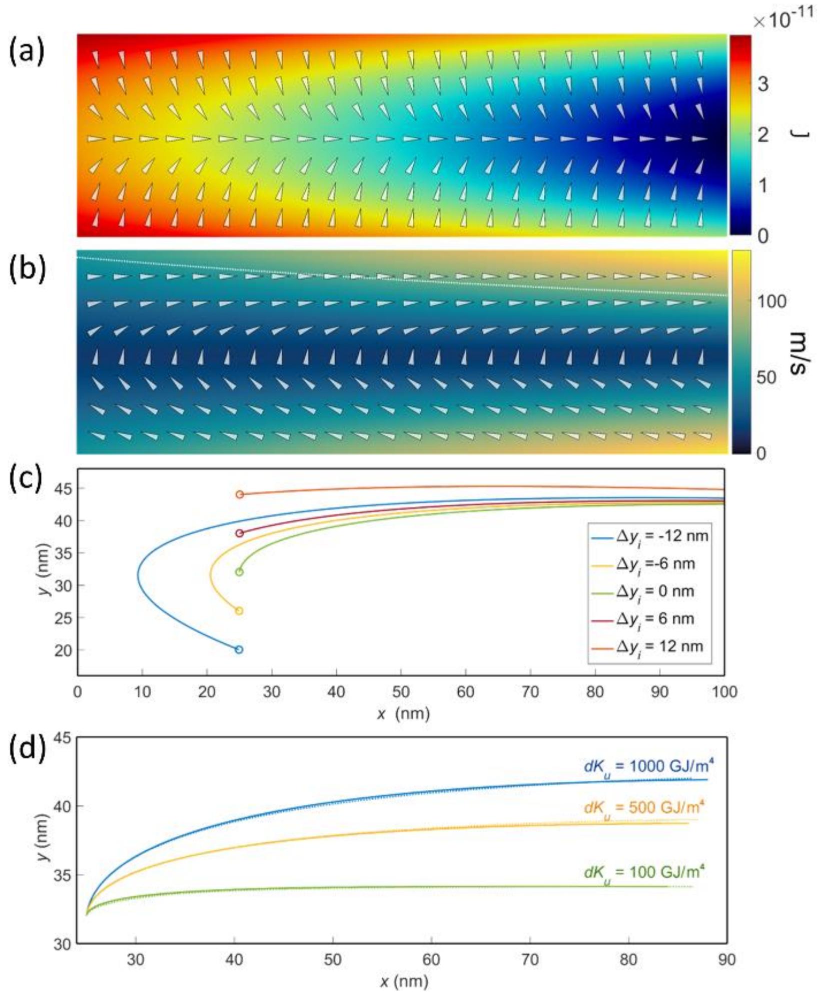

Figure 4-6 (a) 2D force field of the system as a function of skyrmion position on the nanowire (100 nm × 64 nm). (b) 2D skyrmion velocity field. The equilibrium trajectory is marked by the white dotted lines. (c) The trajectories of skyrmion motion with different initial (Δy) obtained by evolving Equation 4-8 in small time steps. (d) Skyrmion trajectory calculated from micromagnetic simulations (solid line) and analytically (dotted).

4.4 Stepped anisotropy gradient for skyrmion transport

To increase the skyrmion velocity, a larger anisotropy gradient is favoured. However, for a skyrmion to remain stable, the K_u should be kept above 0.56×10^6 Jm^{-3}. This leads to a limitation that fast-moving skyrmions can only exist in relatively short nanowires. To allow for devices of any arbitrary length, we propose the use of a discrete gate array (DGA) instead of a single gate electrode that covers the entire device. In such a scheme, an anisotropy gradient can be created when adjacent parts of the nanowire have different K_u values.

Figure 4-7(a) shows the schematic of such a DGA device. The device uses a repeated array of three gate electrodes which can modulate the magnetic anisotropy of the adjoining track region to be one of three states; +2.5 % (high), -2.5 % (low) or unchanged (off).

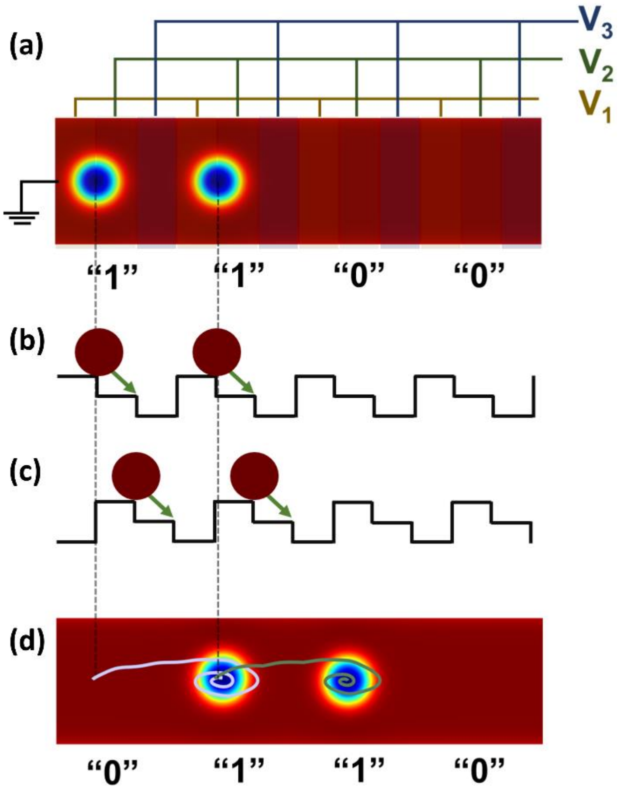

Figure 4-7 (a) Schematic diagram of a multiplexed discrete gate array architecture for controlling anisotropy gradient (b) Magnetostatic energy levels across the length of the nanowire demonstrating how the stepped voltages can create potential wells. The potential gradient-induced motion of the skyrmion is indicated by the green arrows. (c) Magnetostatic energy levels after a "shift" operation. (d) Magnetization snapshot after three consequent shift operations.

Therefore, when the states of three consecutive electrodes are set to off-low-high, a potential well is formed at the second electrode. The electrodes in each set of three electrodes are also multiplexed; since each electrode is connected to its next nearest neighbour, a series of skyrmion potential wells are formed as shown in Fig. Figure 4-7 (b-c). In this way, the skyrmion-skyrmion repulsion can be overcome and the spacing between skyrmions be kept constant. For conventional skyrmion-based devices, skyrmions should have a spacing of at least 2.6 times larger than its diameter to minimize the skyrmion-skyrmion interaction.[46] In our device, skyrmions are packed at 1.5 times their diameter, which increases the packing density by at least 70%. The strong confining potentials also traps skyrmions in discrete positions without the need for inefficient geometrical pinning sites.[1]

To propel the skyrmion, the electrode voltages are then changed to the low-high-off states which shift the potential well to the right. In the device, the use of three electrodes allows us to ensure that skyrmions are always propelled in one direction; in a device with only groups of two electrodes, a skyrmion sitting at a high state electrode has the equal likelihood to shift in either direction as both adjacent electrodes would have the same potential. The shift operation can be repeated indefinitely and with a change in K_u between the gates at ± 2.5%, an average velocity of 70 m/s was achieved. Increasing the change in K_u to above ± 2.5% leads to eventual annihilation at the edge. The change of K_u at ± 2.5% between the gates correlates to a $\frac{dK_u}{dx}$ of 1300 GJm^{-4}, which should produce a skyrmion velocity of 103 m/s according to Equation 4-14. However, as only a part of the skyrmion is on the anisotropy step at any given time, the effective $\frac{dK_u}{dx}$ acting on the skyrmion is decreased, unlike in a smooth K_u gradient which Equation 4-14 is based on.

Besides the improved energy efficiency, the use of discrete gate electrodes allows anisotropy gradient-induced skyrmion transport to be implemented on almost any arbitrary 2D geometries. Of interest is the recirculating closed loop structure which allows read/write operations to be non-destructively, as shown in Figure 4-8(a). In contrast, conventional nanotrack devices must be at least twice as long as the skyrmion chain in order for the entire skyrmion chain to traverse past the central read-write heads. In other words, at least half the nanowire must be used as a skyrmion buffer for reading. As shown in Figure 4-8, the use of a closed-loop also enables skyrmions to be returned to their original positions after read/write, thus removing the need for a skyrmion buffer area. The ability to continuously shift the entire skyrmion chain by applying the same excitation can also simplify the design of skyrmion devices.

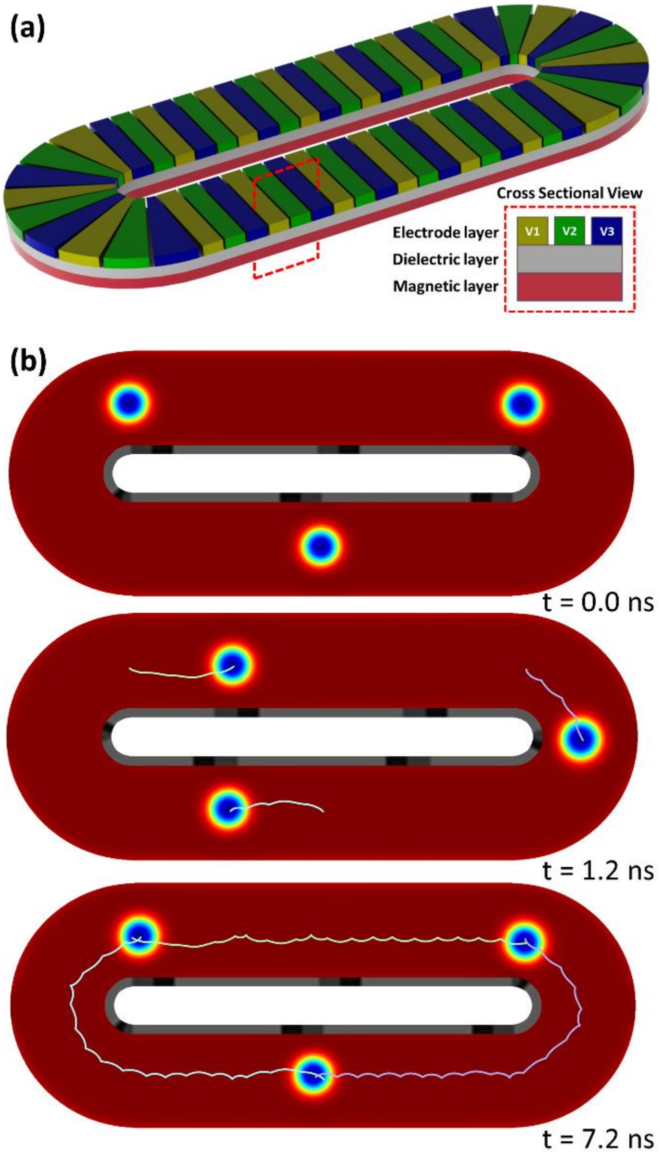

Figure 4-8 (a) 3D Schematic diagram of a stepped anisotropy for racetrack memory. The electrode layer V_1, V_2 and V_3 corresponds to those in Figure 5. (b) Magnetization snapshots at $t = 0$ ns, $t = 1.2$ ns and $t = 7.2$ ns respectively. There are 3 skyrmions in the system and 6 sets of K_u, which is represented by the grey rectangle in the centre loop and induced by a voltage gate. When the gate voltage is switching clockwise, skyrmions are driven clockwise.

4.5 Energy efficiency of VCMA vs current-based driving methods

The VCMA effect does not require a current in the magnetic layer and is therefore inherently dissipationless. However, a microscopic amount of electrical energy is needed to charge the capacitive dielectric layer. The VCMA efficiency can be expressed as a ratio between induced PMA change and applied electric field $\frac{\Delta K_u}{\Delta E}$. As reported by Y. Suzuki *et.*

al., a small electric field of 100 mV/nm can cause a 40% change in K_u with $\frac{\Delta K_u}{\Delta E} = 210$ fJ/Vm.[47] Using a more conservative estimate of $\frac{\Delta K_u}{\Delta E} = 100$ fJ/Vm, we find that for the 2×10^4 J/m^3 change in the K_u required by stepped anisotropy gradient, an electric field of 0.1 V/nm needs to be applied across a gate oxide of 1 nm. Using MgO as a gate oxide with a relative permittivity of 7 and an area of 60 nm × 20 nm, the energy required to create the electric field is 0.18 aJ. To achieve a speed of 70 m/s, the gate must be charged at a rate of 3.5 GHz. The resulting power consumption of shifting a single skyrmion at 70 m/s is then 0.65 nW.

The energy dissipation in current-driven skyrmion devices can be calculated from the resistive energy losses through Joule heating. Experimental data from Hrabec *et al.* show that a current density of 5×10^{11} Am^{-2} is required to drive a skyrmion at 70 m/s.[11] For comparison purposes, we assume that skyrmions on both systems have the same total magnetic volume. However, for current-driven devices, an additional 4 nm of heavy metal, usually Ta or Pt is added for a strong spin Hall effect required for high-speed manipulation Taking a bulk resistance value of 1×10^{-7} $\Omega\mathrm{m}$, the power consumed in current-driven skyrmion devices for shifting a single skyrmion at 70 m/s is 0.5 μW.

4.6 Challenges for the discrete gate array devices

Despite the many positive attributes about DGA devices, it faces a few challenges which need to be addressed. In this section, the disadvantages of the DGA devices are discussed in detail, before a solution to the problems is discussed.

The small feature sizes required by DGA devices create significant challenges for manufacture. Here, the discussion is based on the criteria to achieve fast skyrmion translation speeds using Equation 4-13. Assuming that the skyrmion size stays constant, *dK* should be maximized while *dx* should be minimized. While the maximum achievable *dK* has seen large improvements in recent times,[48, 49] it may not be applicable in every material system and hence, it may not be prudent to rely on increasing *dK* to improve skyrmion transport speeds. To minimize *dx*, each individual gate electrode should be made as narrow as possible such that *dx* is small. Further, to prevent shorting, each electrode must be spaced apart by at least the thickness of the gate oxide layer. Many works on VCMA have used an oxide layer thicker than 20 nm to prevent leakage currents.[50-52] This requirement has so far been too prohibitive for small skyrmions. As illustrated in Figure 4-9(a), the electrodes should be smaller than the skyrmion radius, while the gap between electrodes should be larger than 20 nm, this leads to large devices being feasible but with lower densities.

The SkHE-induced gyration of the skyrmion also adds uncertainty. In Figure 4-9(b), the practical implication of the SkHE is demonstrated. The K in the highlighted region was increased from 800 kJm^{-3} to 1000 kJm^{-3}, which then exerts a force in the x-direction. However, plotting the simulated skyrmion trajectory over 10 ns reveals that the skyrmion does not move directly to its intended position but rather gyrate around the intended position with decreasing amplitude. The gyrating motion adds an element of stochasticity in controlling DGA devices where the gate electrodes must be turned on in sync with the skyrmion position. Mistracking occurs when the skyrmion fails to keep up with the shifted VCMA. In order to prevent the mistracking of the skyrmion, a long wait time is enforced between driving skyrmions from one well to another. Such a technique was employed in Figure 4-7(d), where the gyrating motion of the skyrmion was observed, and allowed to be damped over time.

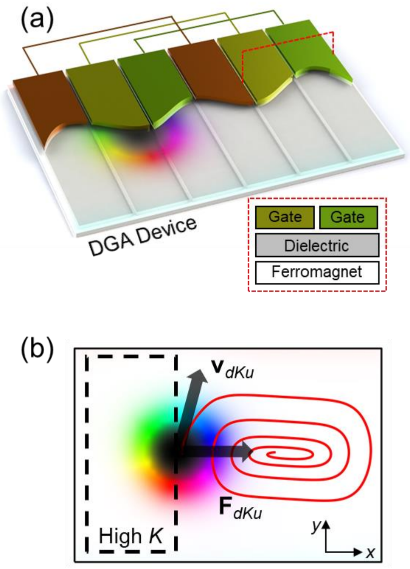

Figure 4-9 (a) 3D rendered cross-sectional image of a Discrete Gate Array (DGA) skyrmion device. The voltages on each of the electrodes are alternated between the high and low states such that between two adjacent electrodes, there exists a gradient in VCMA that drives the skyrmion. (b) Trajectory (in red) of a skyrmion 10 ns after the area highlighted (dotted line) is increased in magnetic anisotropy. The black arrow represents the initial forces and resultant velocity acting on the skyrmion.

To illustrate some of the consequences, the Thiele equation including the contribution from F_y (Equation 4-12), was evolved in time numerically. In Figure 4-10, the skyrmion is repeatedly propelled by using cycles of 1 ns of applied F_x and then followed by 1 ns of relaxation. The varying distances moved by the skyrmion under the same applied forces is made obvious by the vertical lines. This is due to the net y-displacement of the skyrmion, which according to Equation 4-12, confers additional x-velocity to the skyrmion. While the increased velocity may seem advantageous for hi-speed memory applications, it can be hard to realize the velocity gains. Under an ideal situation, the skyrmions can be assumed to be at the centre of the nanowire. Then, to account for the increasing y-displacement, the "on" duration of the gate voltage pulse should decrease with increasing pulses. However, the position of the skyrmion cannot always be determined.

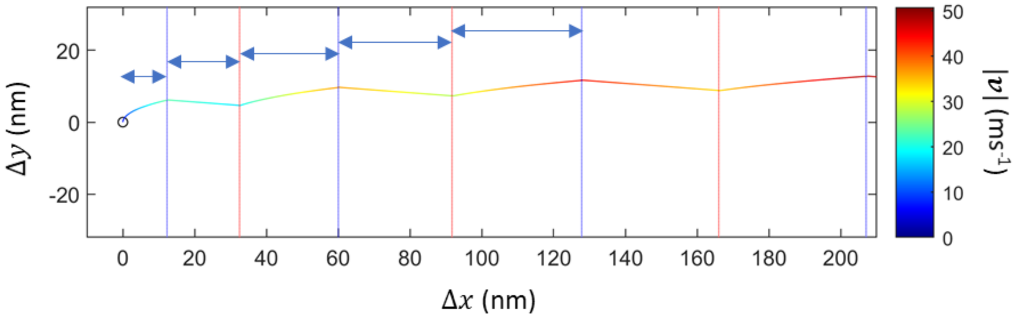

Figure 4-10 Trajectory of a skyrmion under repeated cycles of 1 ns "on" and 1 ns "off" pulses of the driving force. The trajectory was obtained from numerically evolving the Thiele equation. The blue and red vertical lines mark the start of an "off" and "on" pulse, respectively.

The motion of skyrmions under a discretely shifting potential was also calculated using the Thiele equation in a setup similar to Figure 4-7. The driving force was modelled by having a positive sign when the skyrmion is within ±20 nm of the potential well centre, and the sign turns negative everywhere else. The negative force is experienced when the skyrmion incurs onto the high K_u regions. The negative force also describes the penalties of mistracking when the skyrmion is more than 20 nm away from the centre of the potential well. The potential landscape was then shifted every 0.6 ns. In Figure 4-11(a), the optimized drive trajectory of a skyrmion is shown. Similar to Figure 4-10, a smooth trajectory was observed because the shift operation is almost perfectly in sync with the skyrmion position. In Figure 4-11(b), we observe that at the initial third and final third of the trajectory, the skyrmion does experience negative F_x due to mistracking. However, the signs of the mistracking were switched as evidenced in Figure 4-11(c). Initially, the skyrmions were too slow, but as it gains *y*-displacement, it starts to outpace the rate at which the potential wells shift.

The two other non-optimal driving conditions are when the potential wells shift too quickly or too slowly. In Figure 4-12, we show the two non-optimal situations. In the case that the potential is moved too quickly, just 0.1 ns faster than the optimal situation, it can be said that catastrophic failure has occurred. The skyrmion has completely lost track of the potential well centre and will continue to do so. When used in a skyrmionic racetrack memory device, the data is lost. While the case of being too slow does not cause data loss, the total distance travelled in 5 ns of operation results in 65 nm of translation. In contrast, the optimal shift rate achieved 175 nm of translation. For DGA devices, it is thus important for a good compromise between speed and reliability to be struck.

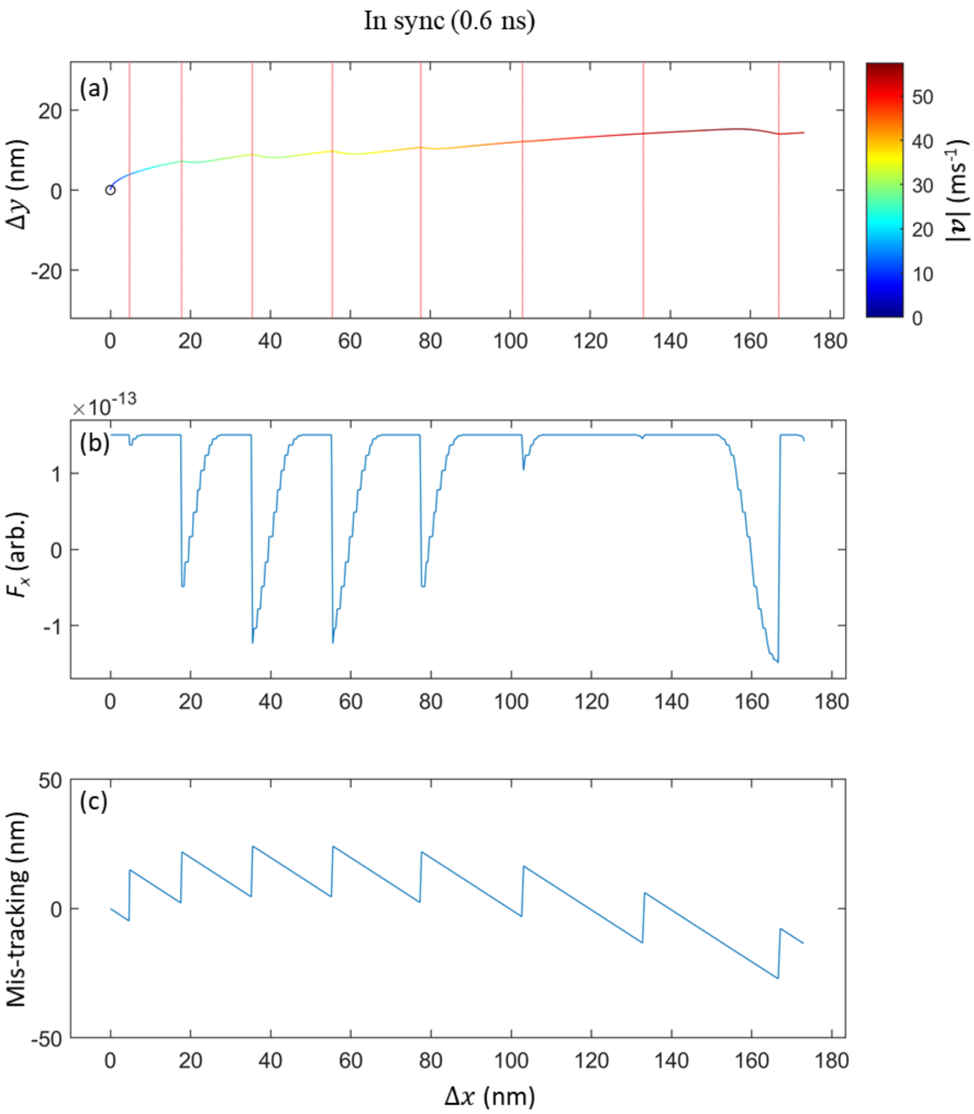

Figure 4-11 Trajectories of skyrmions under optimal drive condition of 0.6 ns/shift. (a) The trajectory of the skyrmion with its speed indicated by the line colour. (b) The plot of F_x against

position. Due to mistracking, the experienced force is not constant. (c) The mistracking of the skyrmion, which is the difference between the potential well centre and the skyrmion centre. Results are derived from numerical calculations based on Thiele equation.

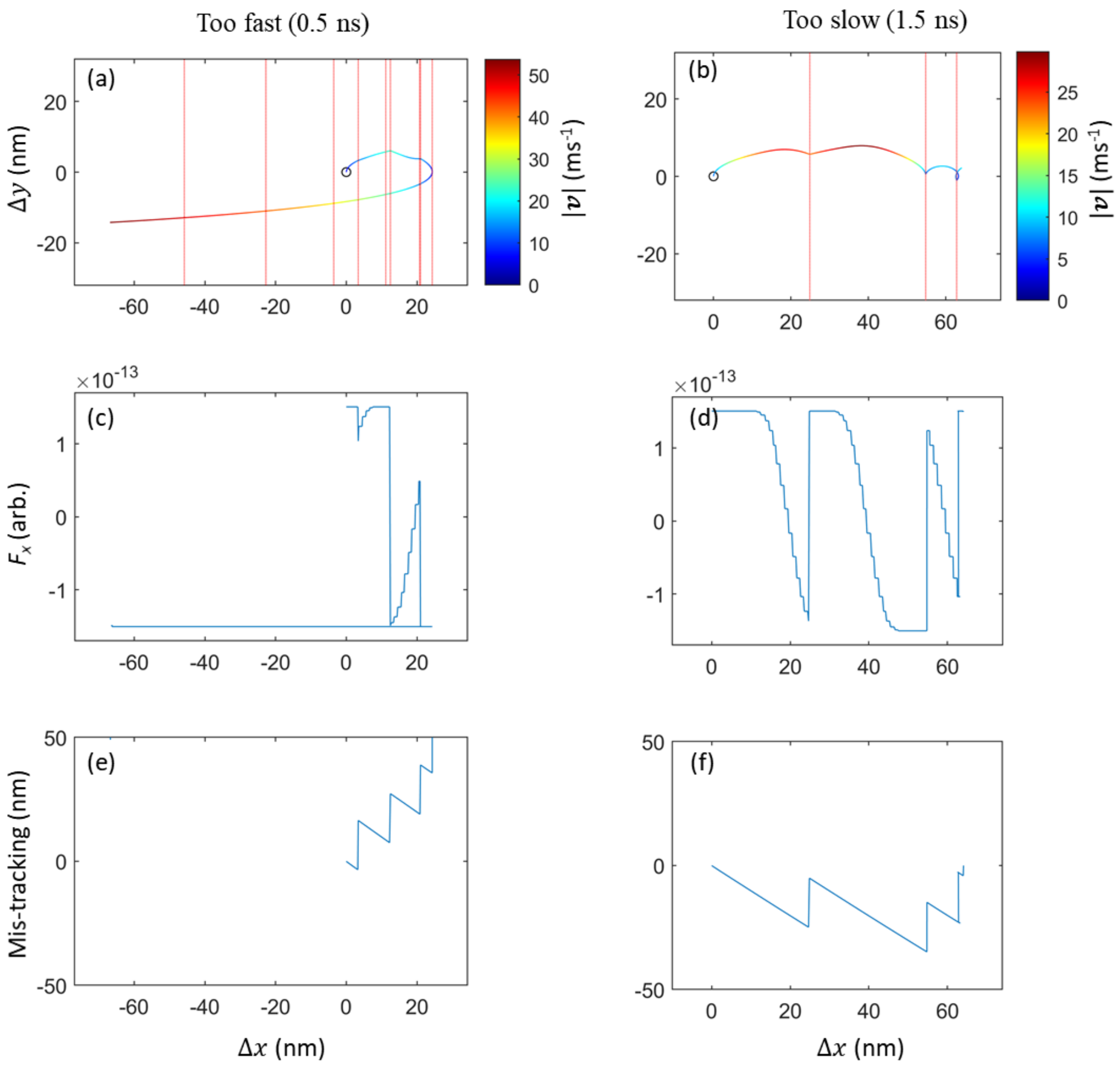

Figure 4-12 Trajectories of skyrmions under non-optimal drive conditions (0.5 ns/shift and 1.5 ns/shift). (a-b) The trajectory of the skyrmion with its speed indicated by the line colour. (c-d) The plot of F_x against position. Due to mistracking, the experienced force is not constant. (e-f) The mistracking of the skyrmion, which is the difference between the potential well centre and the skyrmion centre. Results are derived from numerical calculations based on Thiele equation.

4.7 Skyrmion ratchet device

Evidently, the SkHE greatly reduces the reliability of DGA devices. In this section, we demonstrate an improved skyrmion transport architecture also utilizing a VCMA gradient, the skyrmion ratchet. The new device overcomes many of the challenges faced by DGA devices and additionally, can use a single gate electrode to drive any number of skyrmions. To achieve the feat, a transverse driving force was used in tandem with an array of engineered potential wells that serve as a ratchet for unidirectional skyrmion motion. A key advantage of the skyrmion ratchet lies in its ability to move the skyrmion very closely to the centerline of the nanowire, thus allowing for predictable behaviour and high transport velocities. Finally, we demonstrate that, to circumvent the unidirectional operation, the skyrmion ratchet can recirculate the skyrmions in a closed-loop, thus retaining the very unique and positive characteristic of DGA devices.

Here, we propose the use of a transverse VCMA gradient scheme where $\mathbf{F}_{dK}$ is directed in the -*y*-direction as illustrated in Figure 4-13. The driving scheme relies on the SkHE to drive the skyrmion forward, instead of the driving force itself. Figure 4-14 shows the trajectories of skyrmions driven by a transverse $\mathbf{F}_{dK}$. As the skyrmion moves downwards (-*y*), the skyrmion experiences asymmetric repulsive forces from each of the nanowire edge, leading to an effective force $\mathbf{F}_{\mathrm{R}}$ that restores the skyrmion to the centre of the nanowire. By initializing a skyrmion magnetization at different *x* and *y* coordinates, an amplitude map of the system's magnetostatic energy is generated.[53] Further performing a gradient operation, $\mathbf{F}_{\mathrm{R}}$ is obtained as a function of skyrmion position and is shown as a colourmap superimposed on Figure 4-14(a). $\mathbf{F}_{\mathrm{R}}$ increases with the skyrmion *y* displacement from the nanowire centre up to about 6 nm, before abruptly changing signs and pushing the skyrmion away from the nanowire centre. In our analysis, only small displacements were considered as the large displacements would have caused skyrmion annihilation. The interplay between $\mathbf{F}_{dK}$ and $\mathbf{F}_{\mathrm{R}}$ results in the complete cancellation of the forces at a threshold *y*-position as marked in Figure 4-14(a) as a dotted line. If the applied VCMA is increased, $\mathbf{F}_{dK}$ is increased and the threshold *y*-position would be shifted further downwards so that $\mathbf{F}_{\mathrm{R}}$ becomes as strong as $\mathbf{F}_{dK}$.

Figure 4-13 Schematic illustration of the transverse driving scheme. The driving force is oriented transversely to the direction of intended motion.

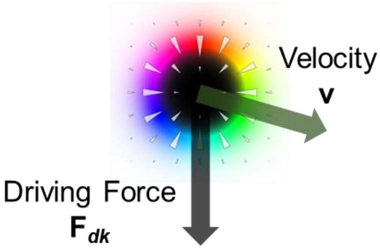

The naïve approach of using a transverse $\mathbf{F}_{dK}$ to propel skyrmions backfires when the VCMA modulation is turned off. Without $\mathbf{F}_{dK}$ to oppose $\mathbf{F}_{\mathrm{R}}$ the skyrmion experiences an upward force which leads to the SkHE driving the skyrmion backwards to its starting point. As α affects the SkHE angle, the total *x*-displacement allowed was observed to be very dependent on α. The ratio between the *x*- and *y*-velocity is given by $\frac{v_x}{v_y}=\frac{G}{\alpha D}$ (Equation 4-6). Since the final *y*-displacement is fixed, the SkHE angle determines the maximum *x*-displacement that the skyrmion can reach in one voltage pulse.

In Figure 4-14(b), the displacement Δx over time due to an applied transverse $\mathbf{F}_{dK}$ is shown. Immediately after the transverse $\mathbf{F}_{dK}$ is applied, the skyrmions move forward with very similar velocities. However, with time, the larger downwards displacements of the higher α skyrmions result in rapidly increasing $\mathbf{F}_{\mathrm{R}}$ and reduces the net downwards force acting on the skyrmion. Consequently, the *x*-velocity decays quickly. Therefore, it is important to capitalize on the first nanosecond of applied $\mathbf{F}_{dK}$ for fast skyrmion transport, especially in materials with a high α.

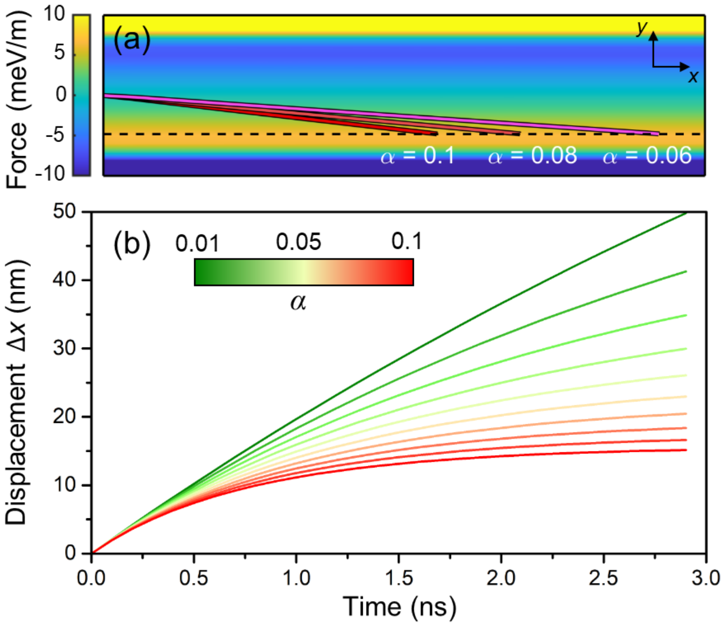

Figure 4-14 (a) Skyrmion trajectories driven by a transverse VCMA gradient in a nanowire. To observe the small *y* displacements, the image is zoomed in such that only the middle 20 nm out of the total 36 nm width is shown. The length is 76 nm. The nanowire background colour shows the transverse forces acting on the skyrmion due to the edge repulsion. The black dotted line indicates the position where the VCMA driving force equals to the edge repulsion force. (b) The skyrmion *x*-displacement over time as a function of Gilbert damping α.

To summarize, there are two main challenges for using a transverse $\mathbf{F}_{dK}$. Firstly, the skyrmion *x*-displacement is strongly tied to the interplay between $\mathbf{F}_{dK}$ and $\mathbf{F}_{\mathrm{R}}$; as soon as the driving $\mathbf{F}_{dK}$ is removed, $\mathbf{F}_{\mathrm{R}}$ takes over and moves the skyrmion backwards. Secondly, the maximum *x*-displacement that can be achieved by the transverse driving mechanism is limited by α. To overcome these challenges, we propose the addition of a series of potential wells along the nanowire axis. The potential wells create an attractive force that prevents the skyrmion from moving backwards once the skyrmion moves into the next potential well's radius of influence.[54-56] Also, by spacing the potential wells closely, a single gate pulse is able to propel the skyrmion to the next potential well. In Figure 4-15(a), such a skyrmion ratchet is shown, with the potential wells created in between geometrical notches. The operation is simple; by applying a gate voltage to the upper half of the nanowire, *K* is locally increased and the $\frac{dK}{dy}$ induces a $\mathbf{F}_{dK}$ which drives the skyrmion rightwards.

In Figure 4-15(b-c), the force map of $\mathbf{F}_\mathrm{R}$ acting on the skyrmion ratchet is shown for the *y* and *x* directions, respectively. The force landscape has transformed significantly as compared to Figure 4-14(a) due to the addition of the geometrical notches. Three main events occur during the process and are circled in Figure 4-15(b). In the first event, the skyrmion is at rest and resides at the centre of the potential well due to energy minimization. The gate voltage is turned on and the skyrmion is propelled forward with a slight downward velocity. At the second event, the skyrmion is close enough to the next potential well, and the gate voltage is switched off. The attractive force of the next potential well is used to pull the skyrmion forward, i.e. $\mathbf{F}_\mathrm{R}$ is in the positive *x*-direction. In doing so, the SkHE also generates a +*y* displacement due to the SkHE, which allows the skyrmion to quickly reach the potential well centre. At the third event, the skyrmion once again resides at the centre of the potential well and the voltage pulse sequence can be repeated at any time.

In Figure 4-15(b), the *y*-displacements in the skyrmion trajectory was observed to match very well with the line where $\mathbf{F}_R^y = 0$. In fact, the skyrmion ratchet is operated such that the VCMA gate should be turned on/off to minimize the deviation from $\mathbf{F}_R^y = 0$. When the skyrmion is driven too low $\left(\mathbf{F}_R^y > 0\right)$, $\mathbf{F}_R^y$ starts to oppose $\mathbf{F}_{dK}$ which results in inefficient operation. Figure 4-15(c) shows that at the midway point of two potential wells, $\mathbf{F}_R^x$ also switches direction (-*x* to +*x*) and propagate the skyrmion forward instead.

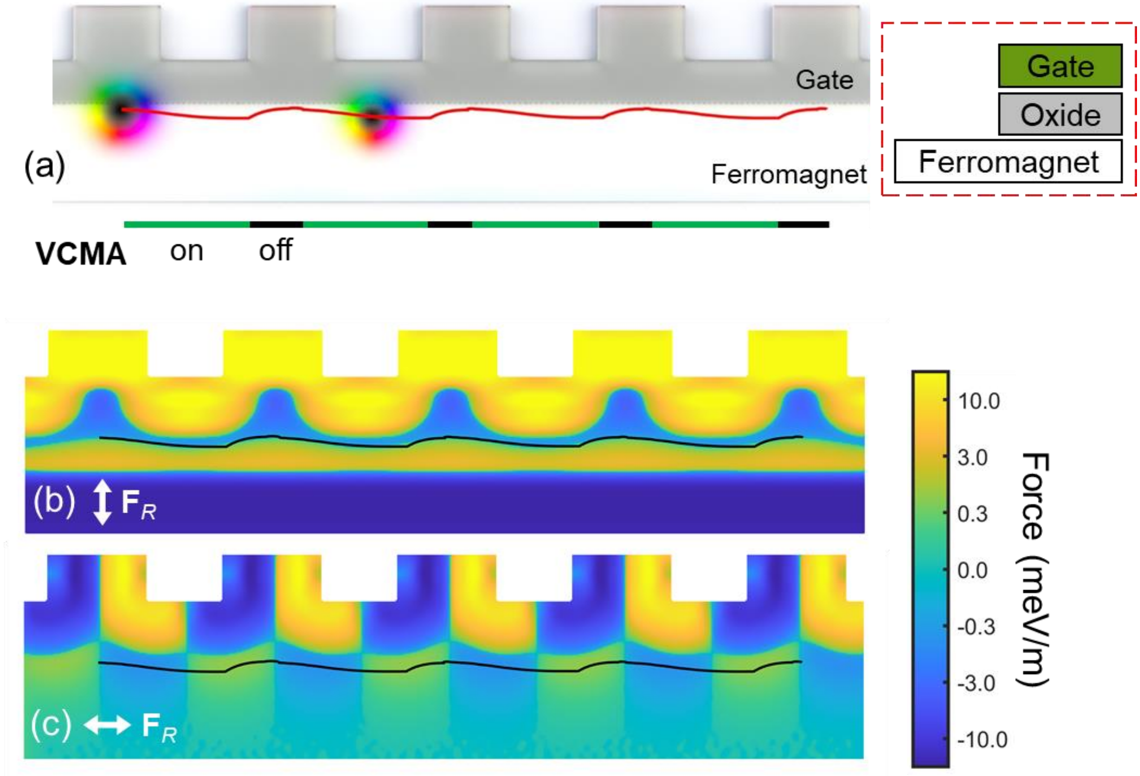

Figure 4-15 (a) Image of a 192 nm long skyrmion ratchet device with 12 nm × 8 nm notches. The red line represents the skyrmion's trajectory across the device. To shift the skyrmion, a series of four voltage pulses were applied and the on/off state of the gate electrode is represented by the green/black bars underneath the image. The inset on the right shows the cross-sectional image of the nanowire. (b-c) Force map of nanowire edge repulsion force $\mathbf{F}_R$ acting on the skyrmion where (b) and (c) shows the y and x magnitude, respectively.

Due to the nanowire geometry, there can be two different placements of the gate electrode (top or bottom) and two dK polarities ($dK < 0$ or $dK > 0$) that can be used to propagate the skyrmion. The design used for the device in Figure 4-15 was subjected to two design considerations. First, to propagate the skyrmion past the notches, the pinning forces should be reduced. A study by Fook et. al. has shown that when propagating a skyrmion across a geometrical pinning site, most of the energy is expended to compress the skyrmion to the threshold size. To reduce the skyrmion size, a positive dK is used, such that the skyrmion is shrunk rather than enlarged. With the dK polarity fixed, the placement of the gate electrode determines whether the skyrmion is driven upwards or downwards ($+y$ or $-y$). Keeping in mind that the notches are positioned on top, the gate electrode should also be on top, to drive the skyrmion downwards away from the notch.

An important performance characteristic for skyrmion devices is the skyrmion transport velocity. In Figure 4-16, the skyrmion velocity versus dK is shown. The velocity was calculated based on the gate voltage on duration versus the inter-notch distance. The results indicate that despite requiring only a single gate electrode, the skyrmion ratchet can achieve similar performance to DGA devices. However, at a low *dK* (175 kJm^{-3}), $\mathbf{F}_{dK}$ is insufficient to overcome the attraction of the potential wells. To reduce the attractive potential, the notch depth can be reduced, as shown on the bottom right inset of Figure 4-16. However, the skyrmion velocity is also reduced, due to the reduced $\mathbf{F}_{\mathrm{R}}$ that also helps to propagate the skyrmion. Therefore, in reducing the threshold *dK*, the skyrmion velocity is traded-off.

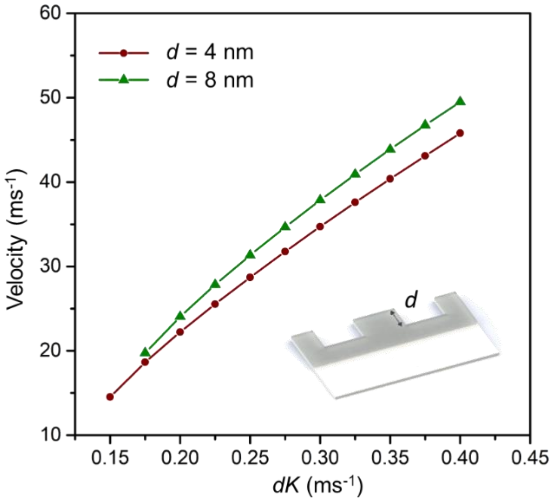

Figure 4-16 Plot of skyrmion velocity versus the amplitude of the high state anisotropy. The pinning depth *d*, illustrated in the top right inset, was also varied.

The skyrmion ratchet also offers new possibilities as compared to the well-studied spin torque-induced skyrmion transport techniques. In the latter type of skyrmion transport, an electron current is needed, either for spin-transfer torque or for generating spin-orbit torques. Therefore, in having a current source and sink, the skyrmions on such a device are limited to travelling between the source and sink. The disadvantage is that the skyrmion read/write operation must be placed midway between the source and sink and that a maximum of half the device can be occupied at any time, to allow the entire skyrmion chain to pass under the read/write head. On the other hand, the skyrmion ratchet can reliably drive skyrmions in a recirculating manner, thus allowing for high storage density and continuous operation.

Figure 4-17 shows a skyrmion ratchet racetrack where, using the same driving scheme as in Figure 4-15, a skyrmion is shifted across 18 potential wells before returning to its original position. The skyrmion trajectory appears to be irregular close to the bend as the distance between notches was not modified to account for the curvature. However, since the skyrmion is maintained at the position of lowest energy, the skyrmion can still be driven reliably across. The first enabling factor is attributed to the predictability is the skyrmion's small deviation from the racetrack centerline. In contrast, DGA devices suffer from excessive gyrations due to their significant distance away from the centre of the nanowire, as shown in Figure 4-9(b). The second enabling factor lies in having the attractive potentials that ensure that the skyrmion is always close to the potential well centre at the end of an operation, even if the voltage pulse duration was suboptimal. Other than providing certainty in skyrmion position, the potential wells also serve as a passive trap for the skyrmion to resist thermal fluctuations, thus allowing for long term data storage even when the gate voltage is turned off. In other words, the skyrmion ratchet is a truly non-volatile memory.

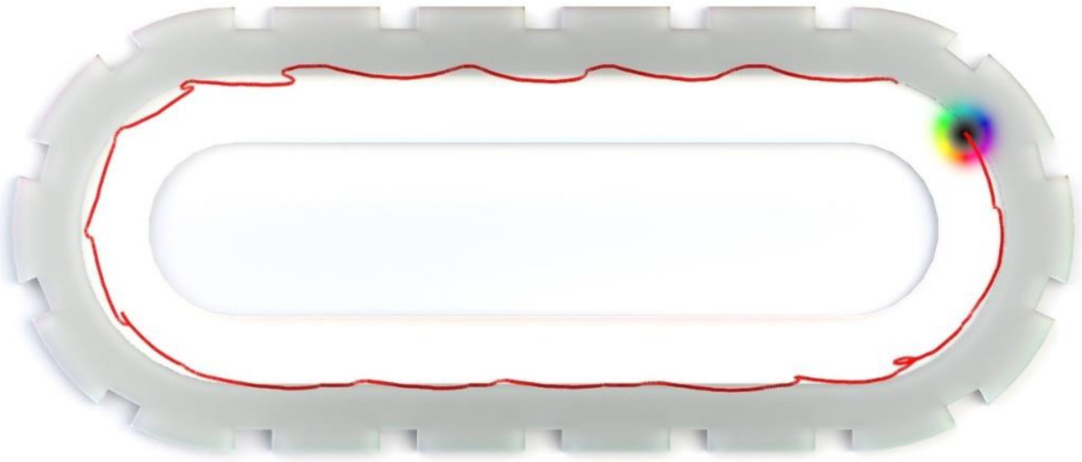

Figure 4-17 Image of a recirculating skyrmion ratchet where the red line represents the skyrmion trajectory. To shift the skyrmion by a step, a voltage pulse of 0.8 ns was applied followed by a 1 ns interval for the skyrmion to relax into the potential well.

In this section, a skyrmion ratchet was conceived to prevent the backwards motion by introducing a series of potential wells. The attractive potentials prevent the skyrmion from moving backwards, resulting in a unidirectional, ratchet-like motion. The performance of the skyrmion ratchet devices was also demonstrated to be fairly similar to DGA devices, despite requiring only a single gate electrode to operate. The simplicity of the skyrmion ratchet is its greatest advantage over DGA devices. Finally, to allow for read/write operations to be performed on the entire skyrmion chain, a recirculating skyrmion ratchet was demonstrated. The device was able to recirculate the skyrmions, thus allowing for a skyrmion chain the length of the nanowire to be stored and achieving a high skyrmion density. Therefore, our work here has demonstrated a new class of VCMA-gradient devices that has better performance characteristics as compared to previous device architectures.

4.8 Skyrmion Hall effect-assisted depinning

In the skyrmion ratchet device, the maximum velocity is limited by the pinning potential. As the skyrmion is initially pushed against the pinning notch, a significant amount of propulsive force is used to counter the pinning potentials. In this section, we briefly show that the VCMA-gradient devices can easily be tweaked to alter the skyrmion trajectory. This is enabled by using the theoretical understanding developed in Section 4.2 and 4.3. To avoid the pinning potentials, the skyrmions should be initially driven away from the pinning notches, before being sent in the forward direction.

In Figure 4-18(a), a modified skyrmion ratchet design is shown. The skyrmion is driven with 0.2 ns of an “on” state followed by 0.7 ns of “off”. By having vertical strips of gate electrodes, a rightwards force can be exerted on the skyrmion, which due to the skyrmion Hall effect, drives the skyrmion upwards. The additional vertical segments are highlighted by the red dashed line in Figure 4-18(a). The red trajectory shows the initial upwards displacement. The notches are also moved downwards so that the skyrmion is initially pushed away from the notches. A benefit of this modification is that the $\mathbf{F}_R$ of the edges gives the skyrmion a rightwards velocity. As evidenced in the velocity profile in Figure 4-18(b), the skyrmion accelerates quickly in the “on” state and maintains a respectable velocity of 20 to 40 ms^{-1} even during the “off” state. In this demonstration, a dK of 0.2 MJm^{-4} is used, which allows the skyrmion to achieve a maximum speed of 85 ms^{-1}, which after accounting for dK, is several times faster than the original skyrmion ratchet.

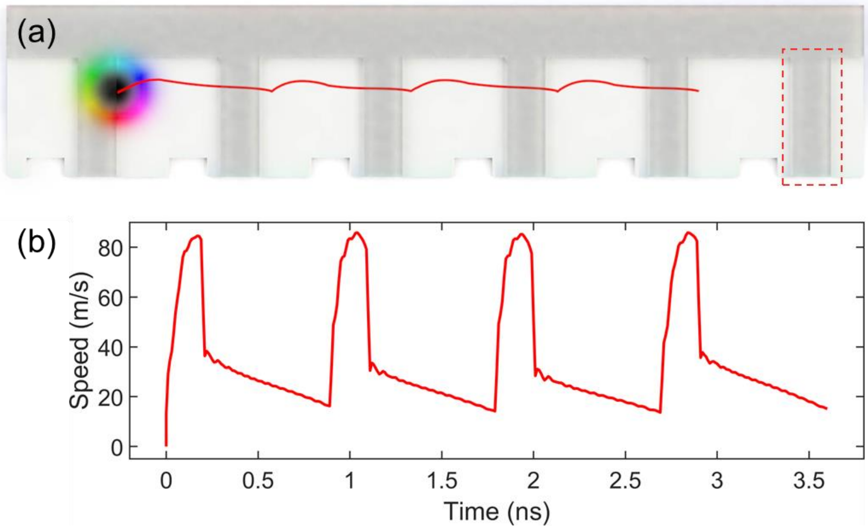

Figure 4-18 (a) Rendered image of a modified skyrmion ratchet device, with an additional vertical gate to give the skyrmion a slight initial upwards boost. (b) Skyrmion velocity profile during the operation of the modified skyrmion ratchet device.

The forces acting on the skyrmion are plotted in Figure 4-19. In the “off” state, the skyrmion experiences a force landscape that is due to the pinning potentials. During the “on” state, what was previously the energy minima turns repulsive. Due to the leftwards placement of the vertical gate electrode sections, the skyrmion is pushed rightwards. Also noticeable is the increased downwards force. When transitioning into the “on” state, the horizontal gate electrode performs the function of shifting the repulsive force $\mathbf{F}_R$ downwards. As discussed in Section 4-3, $\mathbf{F}_\mathrm{R}$ is responsible for greatly increasing the rightwards speed. By shifting the repulsive force $\mathbf{F}_\mathrm{R}$ downwards, the skyrmion does not have to travel closer to the edge in order to experience a strong $\mathbf{F}_\mathrm{R}$. Therefore, the skyrmion speed is greatly enhanced without too much deviation from a purely rightwards trajectory. In using such a scheme, the pulse timings are once again important. As the skyrmion moves across the geometrical notch, it comes into contact with the next vertical gate electrode. If at this moment, the device is still in the “on” state, the skyrmion experiences a backwards force.

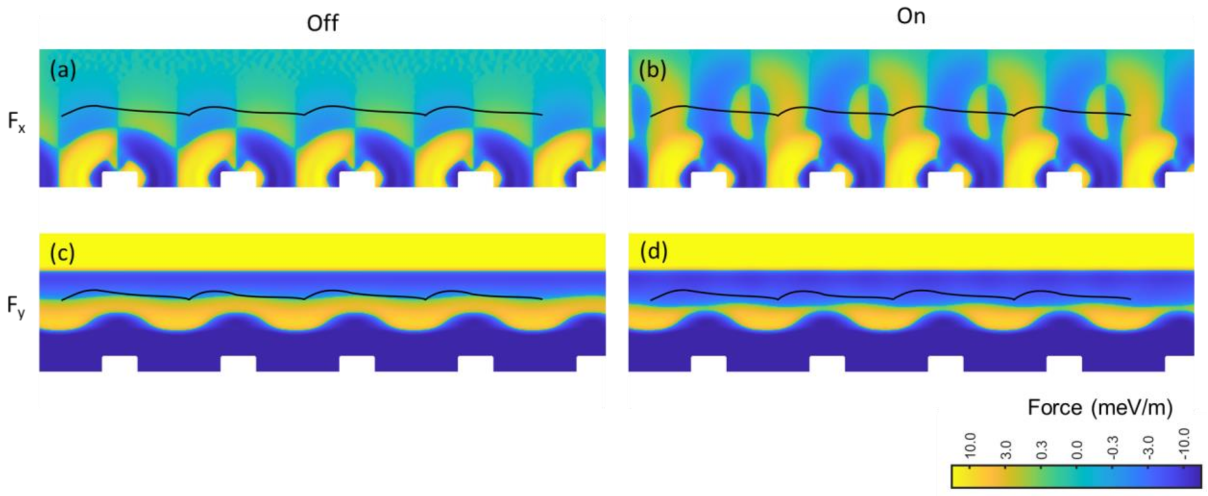

Figure 4-19 The force landscape acting on a skyrmion. The horizontal forces acting on the skyrmions during the “off” (a) and “on” (b) states. The vertical forces acting on the skyrmions during the “off” (c) and “on” (d) states

In Figure 4-20, the skyrmion trajectories on fast and slow operating conditions are shown. Even though an upper speed limit of 0.9 ns per shift operation still applies, the modified skyrmion device can operate at lower speeds without risk of losing track of the potential profile. This behavior is attributed to the good control of the skyrmion trajectory, which minimized gyrations like those seen in Figure 4-10(b).

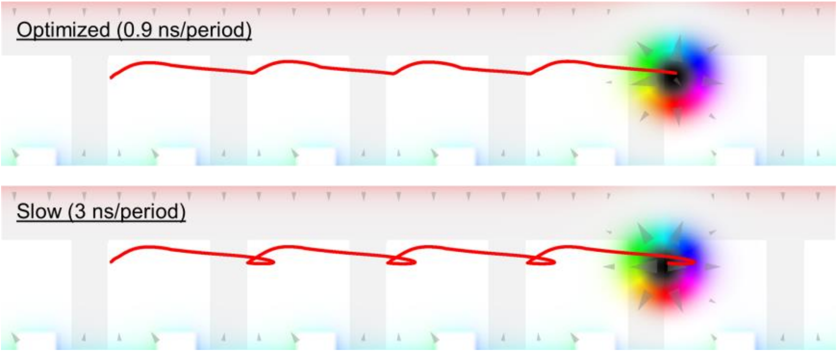

Figure 4-20 Skyrmion trajectories when operating at different speeds. The optimized configuration is determined to be the fastest that the skyrmion can be shifted without losing steps.

4.9 Summary

In conclusion, we have shown that skyrmions can be driven by an anisotropy gradient created via applying a gate voltage in the absence of spin current. A model was developed to understand the forces acting on a skyrmion under an anisotropy gradient. Using the model, the skyrmion’s speed and trajectory can be accurately predicted. To create anisotropy gradients of any arbitrary length without a large variation in anisotropy, three schemes of using a stepped magnetic anisotropy was demonstrated:

1. In the first scheme, the gate electrodes create a rightwards force, which results in the skyrmion moving upwards and experiencing significant gyrations.
2. The gate electrodes create a downwards force, which drives the skyrmions rightwards. Geometrical pinning sites were used to prevent the skyrmions from shifting back due to an upwards $\mathbf{F}_R$. However, the pinning sites also results in strong pinning and lower velocities.
3. The gate electrodes were used to create spatially non-uniform forces; an initial upwards push so as to avoid the pinning site and then later, a rightwards push for high-velocity translation.

The anisotropy gradient-driven skyrmion devices were found to be very flexible in terms of design. With the theoretical understanding, it is possible to manipulate skyrmions in a precise manner. As compared to conventional spin torque-driven skyrmion devices, the use of discrete anisotropy steps in both a nanowire and closed-loop geometry is three orders of magnitude more energy-efficient. Our work here provides insights into the development of anisotropy gradient-driven skyrmion devices and paves the way for its realization.

References

1. H. T. Fook, W. L. Gan and W. S. Lew, *Sci. Rep.*, 2016, **6**, 21099.
2. C. Navau, N. Del-Valle and A. Sanchez, *Phys. Rev. B*, 2016, **94**, 184104.
3. I. Purnama, W. Gan, D. Wong and W. Lew, *Sci. Rep.*, 2015, **5**.
4. A. Fert, V. Cros and J. Sampaio, *Nat. Nanotechnol.*, 2013, **8**, 152-156.
5. X. Zhang, M. Ezawa and Y. Zhou, *Sci. Rep.*, 2015, **5**, 9400.
6. F. Jonietz, S. Mühlbauer, C. Pfleiderer, A. Neubauer, W. Münzer, A. Bauer, T. Adams, R. Georgii, P. Böni and R. Duine, *science*, 2010, **330**, 1648-1651.
7. J. Sampaio, V. Cros, S. Rohart, A. Thiaville and A. Fert, *Nat. Nanotechnol.*, 2013, **8**, 839-844.
8. H. T. Fook, W. L. Gan, I. Purnama and W. S. Lew, *IEEE Trans. Magn*, 2015, **51**, 1-4.
9. X. Yu, N. Kanazawa, W. Zhang, T. Nagai, T. Hara, K. Kimoto, Y. Matsui, Y. Onose and Y. Tokura, *Nat. Commun.*, 2012, **3**, 988.
10. S. Woo, K. Litzius, B. Krüger, M.-Y. Im, L. Caretta, K. Richter, M. Mann, A. Krone, R. M. Reeve, M. Weigand, P. Agrawal, I. Lemesh, M.-A. Mawass, P. Fischer, M. Kläui and G. S. D. Beach, *Nature materials*, 2016, **15**, 501.
11. A. Hrabec, J. Sampaio, M. Belmeguenai, I. Gross, R. Weil, S. M. Chérif, A. Stashkevich, V. Jacques, A. Thiaville and S. Rohart, *Nature Communications*, 2017, **8**, 15765.
12. O. Boulle, J. Vogel, H. Yang, S. Pizzini, D. de Souza Chaves, A. Locatelli, T. O. Menteş, A. Sala, L. D. Buda-Prejbeanu, O. Klein, M. Belmeguenai, Y. Roussigné, A. Stashkevich, S. M. Chérif, L. Aballe, M. Foerster, M. Chshiev, S. Auffret, I. M. Miron and G. Gaudin, *Nature Nanotechnology*, 2016, **11**, 449-454.
13. J. Kim, K.-J. Kim and S.-B. Choe, *IEEE Trans. Magn.*, 2009, **45**, 3909-3911.
14. K.-J. Kim, J.-C. Lee, S.-B. Choe and K.-H. Shin, *Appl. Phys. Lett.*, 2008, **92**, 192509.
15. A. Yamaguchi, S. Nasu, H. Tanigawa, T. Ono, K. Miyake, K. Mibu and T. Shinjo, *Appl. Phys. Lett.*, 2005, **86**, 012511.
16. S. Kanai, M. Yamanouchi, S. Ikeda, Y. Nakatani, F. Matsukura and H. Ohno, *Appl. Phys. Lett.*, 2012, **101**, 122403.
17. Y. Shiota, T. Nozaki, F. Bonell, S. Murakami, T. Shinjo and Y. Suzuki, *Nat. Mater.*, 2012, **11**, 39.
18. H. Kakizakai, K. Yamada, M. Kawaguchi, K. Shimamura, S. Fukami, N. Ishiwata, D. Chiba and T. Ono, *Jpn. J. Appl. Phys.*, 2013, **52**, 070206.
19. G. Yu, P. Upadhyaya, X. Li, W. Li, S. K. Kim, Y. Fan, K. L. Wong, Y. Tserkovnyak, P. K. Amiri and K. L. Wang, *Nano letters*, 2016, **16**, 1981-1988.

20. P.-J. Hsu, A. Kubetzka, A. Finco, N. Romming, K. von Bergmann and R. Wiesendanger, *Nat. Nanotechnol.*, 2016.
21. D. Chiba, M. Sawicki, Y. Nishitani, Y. Nakatani, F. Matsukura and H. Ohno, *Nature*, 2008, **455**, 515.
22. T. Maruyama, Y. Shiota, T. Nozaki, K. Ohta, N. Toda, M. Mizuguchi, A. Tulapurkar, T. Shinjo, M. Shiraishi and S. Mizukami, *Nat. Nanotechnol.*, 2009, **4**, 158-161.
23. F. Ando, H. Kakizakai, T. Koyama, K. Yamada, M. Kawaguchi, S. Kim, K.-J. Kim, T. Moriyama, D. Chiba and T. Ono, *Appl. Phys. Lett.*, 2016, **109**, 022401.
24. H. Kakizakai, F. Ando, T. Koyama, K. Yamada, M. Kawaguchi, S. Kim, K.-J. Kim, T. Moriyama, D. Chiba and T. Ono, *Appl. Phys. Express*, 2016, **9**, 063004.
25. D. Chiba, M. Kawaguchi, S. Fukami, N. Ishiwata, K. Shimamura, K. Kobayashi and T. Ono, *Nat Commun*, 2012, **3**, 888.
26. W. Kang, Y. Huang, C. Zheng, W. Lv, N. Lei, Y. Zhang, X. Zhang, Y. Zhou and W. Zhao, *Sci Rep*, 2016, **6**, 23164.
27. J. Wang, J. Xia, X. Zhang, G. Zhao, J. Wu, Y. Xu, Z. Zou and Y. Zhou, *arXiv preprint arXiv:1709.03733*, 2017.
28. P. Upadhyaya, G. Yu, P. K. Amiri and K. L. Wang, *Phys. Rev. B*, 2015, **92**, 134411.
29. W. Kang, C. Zheng, Y. Huang, X. Zhang, Y. Zhou, W. Lv and W. Zhao, *IEEE Electron Device Letters*, 2016, **37**, 924-927.
30. A. Barman, S. Wang, O. Hellwig, A. Berger, E. E. Fullerton and H. Schmidt, *Journal of Applied Physics*, 2007, **101**, 09D102.
31. P. J. Metaxas, J. P. Jamet, A. Mougin, M. Cormier, J. Ferre, V. Baltz, B. Rodmacq, B. Dieny and R. L. Stamps, *Physical Review Letters*, 2007, **99**, 217208.
32. R. Wiesendanger, *Nat Rev Mater.*, 2016, **1**, 16044.
33. A. Soumyanarayanan, N. Reyren, A. Fert and C. Panagopoulos, *arXiv preprint arXiv:1611.09521*, 2016.
34. B. Krüger, PhD Thesis, Staats- und Universitätsbibliothek Hamburg, 2012.
35. N. Nagaosa and Y. Tokura, *Nat. Nanotechnol.*, 2013, **8**, 899-911.
36. K. Everschor-Sitte and M. Sitte, *J. Appl. Phys.*, 2014, **115**, 172602.
37. R. Tomasello, E. Martinez, R. Zivieri, L. Torres, M. Carpentieri and G. Finocchio, *Sci. Rep.*, 2014, **4**.
38. X. Zhang, Y. Zhou and M. Ezawa, *Nat. Commun.*, 2016, **7**, 10293.
39. W. Jiang, X. Zhang, G. Yu, W. Zhang, X. Wang, M. B. Jungfleisch, J. E. Pearson, X. Cheng, O. Heinonen and K. L. Wang, *Nature Physics*, 2017, **13**, 162-169.

40. S. Seki and M. Mochizuki, *Skyrmions in Magnetic Materials*, Springer, 2016.

41. K. Y. Guslienko, V. Novosad, Y. Otani, H. Shima and K. Fukamichi, *Phys. Rev. B*, 2001, **65**, 024414.

42. J. Iwasaki, M. Mochizuki and N. Nagaosa, *Nat Nanotechnol*, 2013, **8**, 742-747.

43. S. Rohart and A. Thiaville, *Phys. Rev. B*, 2013, **88**, 184422.

44. R. Skomski, H.-P. Oepen and J. Kirschner, *Phys. Rev. B*, 1998, **58**, 3223.

45. S.-Z. Lin, C. Reichhardt, C. D. Batista and A. Saxena, *Physical Review B*, 2013, **87**.

46. X. Zhang, G. Zhao, H. Fangohr, J. P. Liu, W. Xia, J. Xia and F. Morvan, *Sci. Rep.*, 2015, **5**.

47. T. Maruyama, Y. Shiota, T. Nozaki, K. Ohta, N. Toda, M. Mizuguchi, A. A. Tulapurkar, T. Shinjo, M. Shiraishi, S. Mizukami, Y. Ando and Y. Suzuki, *Nature Nanotechnology*, 2009, **4**, 158.

48. A. J. Tan, M. Huang, C. O. Avci, F. Büttner, M. Mann, W. Hu, C. Mazzoli, S. Wilkins, H. L. Tuller and G. S. D. Beach, *Nature materials*, 2019, **18**, 35-41.

49. T. Nozaki, A. Kozioł-Rachwał, W. Skowroński, V. Zayets, Y. Shiota, S. Tamaru, H. Kubota, A. Fukushima, S. Yuasa and Y. Suzuki, *Physical Review Applied*, 2016, **5**, 044006.

50. Y.-C. Lau, P. Sheng, S. Mitani, D. Chiba and M. Hayashi, *Applied Physics Letters*, 2017, **110**, 022405.

51. F. N. Tan, Q. Y. Wong, W. L. Gan, S. H. Li, H. X. Liu, F. Poh and W. S. Lew, *Journal of Magnetism and Magnetic Materials*, 2019, **485**, 174-179.

52. H. Kakizakai, K. Yamada, F. Ando, M. Kawaguchi, T. Koyama, S. Kim, T. Moriyama, D. Chiba and T. Ono, *Japanese Journal of Applied Physics*, 2017, **56**, 050305.

53. H. T. Fook, W. L. Gan and W. S. Lew, *Scientific Reports*, 2016, **6**, 21099.

54. W. Kang, Y. Huang, C. Zheng, W. Lv, N. Lei, Y. Zhang, X. Zhang, Y. Zhou and W. Zhao, *Scientific Reports*, 2016, **6**, 23164.

55. L. Sánchez-Tejerina, Ó. Alejos, E. Martínez and V. Raposo, *arXiv preprint arXiv:1705.00905*, 2017.

56. J. H. Franken, H. J. M. Swagten and B. Koopmans, *Nature Nanotechnology*, 2012, **7**, 499-503.

Chapter 5 Highly-efficient injection of antiferromagnetically-coupled skyrmions

Although it has been proposed that antiferromagnetically-coupled skyrmions can be driven at extremely high speeds,[1, 2] such skyrmions are near impossible to inject with conventional methods used for similar domain-wall devices.[3, 4] In this section, we first discuss the characteristics and various advantages of using antiferromagnetically-coupled skyrmions. Then, we propose an in-line skyrmion injection method using the DMI-induced edge magnetization tilting on a synthetic antiferromagnetic branched nanostructure. For skyrmion injection, the energy consumption could be considered an important factor; the proposed method lowers the required current density by circumventing the skyrmion topological protection. Further, it was found that, by allowing additional domain walls to form on the branch, the threshold injection current density was further reduced by 59%. The increased efficiency was attributed to inter-domain wall repulsion and domain wall compression. The former acts as a multiplier to the effective field experienced by the pinned domain wall while the latter allows domain walls to accumulate enough energy for depinning. The branch geometry also enables skyrmions to be shifted and deleted with the use of only three terminals, thus acting as a highly scalable skyrmion memory block.

5.1 Dynamics of antiferromagnetically-coupled skyrmions

Despite the skyrmion's attractive attributes as a candidate for a universal memory, they have been at the centre of much scientific endeavors[5-11]. However, a few persistent challenges hinder the realization of the skyrmionic memory. Secondly, as skyrmions are magnetically charged, they experience significant repulsion with each other[10]. This limits the skyrmion packing density and imposes a data density limit on any skyrmion-based memory device.

Although several solutions have been proposed to overcome these challenges, the switch to the use of a synthetic antiferromagnetic medium for skyrmions has been shown to be more promising[1, 12]. In such a system, two skyrmions with opposite polarity but similar chirality are antiferromagnetically coupled across a heavy metal layer, as shown in Figure 5-1(a). Typically, the spacer heavy metal of choice is Ru, at specific thicknesses of 0.4 nm or 0.9 nm.[13] The antiferromagnetic coupling energy density which can be described by:

$$\varepsilon_{AFC} = \frac{-2A_{ie}}{d^2}\left(\mathbf{m}_1 \cdot \mathbf{m}_2\right) \qquad \text{Equation 5-1}$$

where A_{ie} is the interlayer exchange stiffness and describes the strength of the interlayer exchange coupling, d is the separation between the two skyrmion layers, and $\mathbf{m}_\mathrm{i}$ is the normalized magnetization vector on each of the layer i. The variation in **m** can be considered as a continuum by expanding **m**:

$$\mathbf{m}(z+d) = \mathbf{m}(z) + \frac{\partial \mathbf{m}}{\partial z} d + \frac{\partial^2 \mathbf{m}}{\partial z^2} d^2 + \ldots \qquad \text{Equation 5-2}$$

and substituting the expanded **m** into Equation 5-1:

$$\varepsilon_{AFC} = -2A_{ie}\left(\frac{\partial \mathbf{m}}{\partial z}\right)^2 \qquad \text{Equation 5-3}$$

The linear expansion term is neglected as the exchange energy is symmetric; $\mathbf{m}_1$ experiences the opposite effective fields compared to $\mathbf{m}_2$. The term $\mathbf{m}_1 \cdot \mathbf{m}_1$ was also neglected due to its constant value which is insignificant in the energy considerations. Finally, to solve equation in a discretized form, small angle approximations can be applied:[14]

$$\varepsilon_{AFC} = -2A_{ie}\left(\mathbf{m}_1 - \mathbf{m}_2\right) \qquad \text{Equation 5-4}$$

The effective field ($\mathbf{B}_{AFC}$) due to ε_{AFC} can be quite significant, reaching fields of up to 1 T.[15] The strong $\mathbf{B}_{AFC}$ creates a strong coupling between the two antiferromagnetically-coupled (AFC) skyrmions of opposite polarity. Recalling from Equation 3-10, the direction of the spin Hall torque is in part determined from the skyrmion polarity. Hence, the opposite skyrmion polarities in an AFC skyrmion pair results in the cancellation of the skyrmion Hall effect (SkHE). In Figure 5-1(b), the exerted forces on each skyrmion are illustrated.

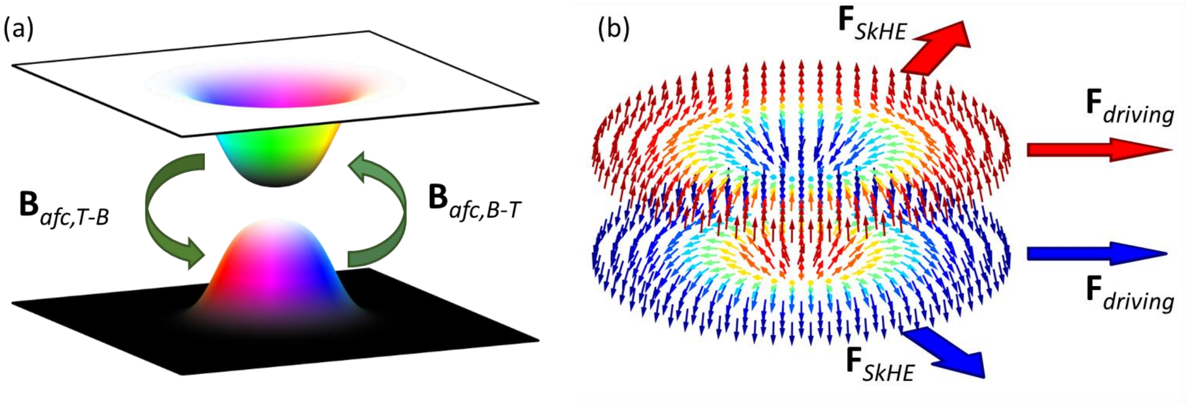

Figure 5-1 (a) Schematic illustration of two antiferromagnetically-coupled skyrmions. The antiferromagnetic exchange field $\mathbf{B}_{afc}$ act mutually on the top and bottom skyrmions. (b) Illustration of the forces acting on both skyrmions. Under the influence of the same driving force, the two skyrmions experience opposite skyrmion Hall effects.

The elimination of the SkHE is only the tip of the iceberg when it comes to the advantages of AFC skyrmion devices. The driving speed, which is one of the key performance characteristics for skyrmion devices, is also greatly enhanced. In the ferromagnetic case, the skyrmion can experience a large speed increase due to the additive edge repulsion force. This is when the SkHE from the transverse force translates into the desired horizontal rightwards motion. In the AFC case, the skyrmion does not need to travel to the edges to experience a transverse force; the skyrmions exert a mutual transverse force on each other. In other words, AFC skyrmions always enjoy the full acceleration from the transverse forces. The amplification factor is given in Equation 3-16 and for the material parameters used, is about six times. The tremendous improvement in speed is evident in Figure 5-2. A pure spin current polarized in the *y*-direction and flowing in the out-of-plane direction and of magnitude 5×10^{10} Am^{-2} was applied. Over 3 ns, the AFC skyrmion evidently travelled a much longer distance.

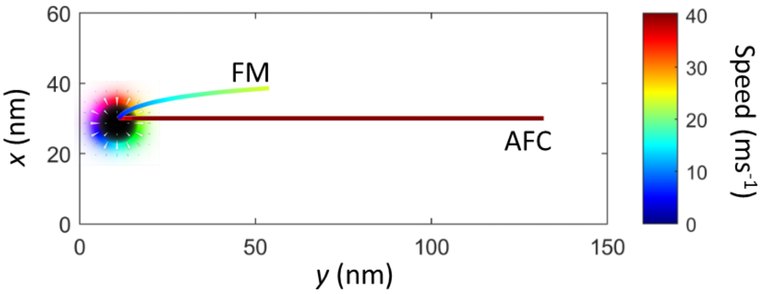

Figure 5-2 Skyrmion trajectories of the ferromagnetic and antiferromagnetically-coupled skyrmion when driven by the same rightwards force for 3 ns. Results were calculated using micromagnetics.

The next advantage of AFC skyrmions is that they can easily be sustained in thin films with the same material parameters. In Figure 5-3, the magnetic ordering of thin films as a function of DMI and magnetic anisotropy is shown. AFC skyrmions can form in a wider range of parameters and are generally smaller. The smaller sizes are advantageous for memory applications and can be attributed to the lower stray magnetic fields.

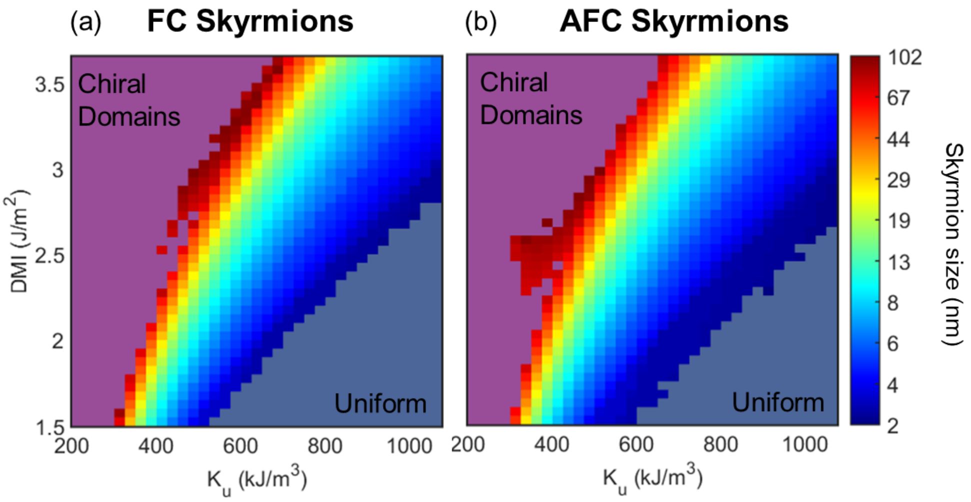

Figure 5-3 Magnetic ordering of thin films as a function of DMI and magnetic anisotropy. In the skyrmion phase (middle portion), the size of the skyrmion is indicated by the rainbow colour with its scale bar given on the right. Results were calculated using micromagnetics.

Due to the lack of a net magnetic moment, AFC skyrmions do not repel each other as significantly as ferromagnetic skyrmions. In Figure 5-4, two skyrmions are pushed together by a driving force as shown in the figure inset. At 2 ns, the converging driving force is removed and the skyrmions are allowed to drift apart. The AFC skyrmions were separated by 75 nm, while the ferromagnetic pair was separated by 175 nm. For memory applications, the more than twice higher packing density is a significant advantage.

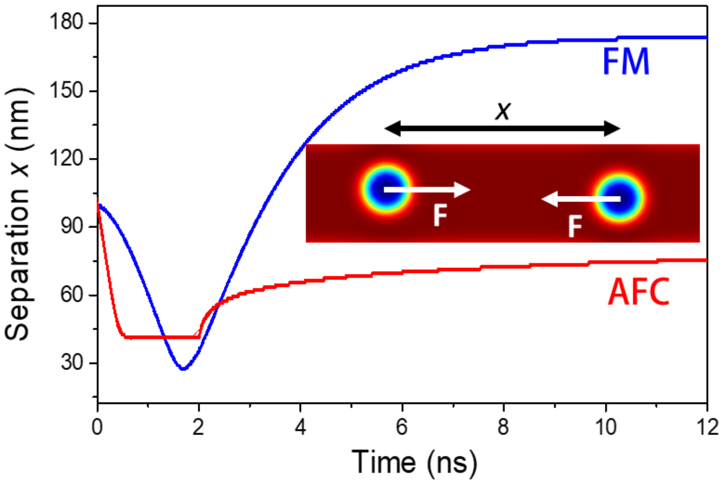

Figure 5-4 Plot of skyrmion separation distance versus time. A converging current was first applied to push the skyrmions inwards for 2 ns, before being allowed to relax.

Despite the many advantages of AFC skyrmions, there exist a few challenges for their use in skyrmionics. In a synthetic antiferromagnetic (SAF) medium, the compensating magnetic moments of the top and bottom layers are insensitive to externally applied magnetic fields, resulting in single skyrmion injection becoming an almost impossible task. Research by Zhou Yan *et. al.* has shown that the vertical injection of spin-polarized current can create skyrmions[1]. However, even with a low interlayer exchange of -2 pJ/m, spin current densities of at least 700 MA/cm^2 are needed. The resulting Joule heating imposes a large thermal stress of the magnetic material, affecting both its spin configuration and its magnetic properties[16-19]. Consequently, the lack of a reliable method to inject single skyrmions remains a key challenge for the development of skyrmionic memory devices.

In the following sections, we will demonstrate a highly efficient, in-line and on-demand injection scheme for SAF-coupled skyrmions on a branched magnetic nanostructure. At the branch edges, the DMI-induced magnetization tilting at the film boundary was harnessed to create a chiral in-plane magnetization that allows spin-orbit torques to efficiently nucleate domains. The domains are then ejected from the branch and propelled into the nanowire to form a skyrmion. The energy-intensive depinning processes were found to be governed by inter-domain wall repulsion and compression which, in a SAF material, exhibits a spring-like behaviour. The effect was exploited by the injection of an additional domain wall into the branch to further reduce the threshold injection current density by a third. Reversing the applied current, we show that the skyrmions are drawn towards the branch and deleted. Therefore, the branched nanostructure can inject, shift and delete skyrmions efficiently.

5.2 Numerical methods

To calculate the effective field, material parameters of Co/Pt multilayers are used as shown in Table 1.[9, 10] The synthetic ferromagnetic coupling models the use of a 0.4 nm Ruthenium spacer layer between the top and bottom magnetic layers with an interlayer exchange strength corresponding to 0.2 pJ/m.[2] However, the magnetization dynamics was found to be insensitive to changes in the SAF coupling strength as long as the skyrmions remained coupled. In all simulations, cell sizes of 1 × 1 × 0.4 nm^3 were used. The material parameters used for the micromagnetic calculations are listed in Table 1. For the synthetic antiferromagnet stack, the Ru layer is assumed to not contribute to either DMI or SOT experienced by the magnetic layers as Ru/Co interfaces show a low spin-orbit coupling.[20]

Symbol	Quantity	Value
M_{sat}	Saturation magnetization	580 kA/m
K_u	Uniaxial anisotropy	500 kJ/m^3
D	Dzyaloshinskii-Moriya interaction strength	2 mJ/m^2
A	Exchange Stiffness	15 pJ/m
α	Damping parameter	0.1
ξ	Degree of non-adiabaticity	0.35
θ_{SH}	Spin Hall angle	0.15

Table 5-1 List of micromagnetic parameters used for numerical and analytical calculations.

Current density modelling

The current density for the branched nanostructures was calculated using the DC current module in the COMSOL multiphysics software. All stated current densities refer to the average current density in the branch.

Domain wall length calculation

To calculate the domain wall length in Section 5-6, the following magnetization profile for the Néel wall was assumed:[21]

$$\theta(x) = 2\tan^{-1}\left(\frac{e^{x/L}-1}{e^{x/L}+1}\right), \qquad \text{Equation 5-5}$$

where θ is the magnetization angle in the *xz*-plane and *L* is the domain wall length. In this case, *x* is taken to be zero at the centre of the DW. The expression can be rearranged to show the out-of-plane magnetization component:

$$m_z(x) = \tanh\left(\frac{x}{L}\right) . \qquad \text{Equation 5-6}$$

The equation was then fitted to the simulated domain wall profile to obtain the domain wall length *L*.

5.3 Spin-orbit torque-induced in-line domain injection

Spin-orbit torques (SOT) have been the subject of many recent research endeavours due to their potential for efficient magnetization switching[22-26]. In particular, the spin accumulation at the heavy metal-ferromagnet interface due to the spin Hall effect has been found to be useful for driving chiral magnetization and switching magnetization. For an electric current applied in the *x*-direction, the effective field from the spin Hall effect is given by:

$$\mathbf{H}_{SH} = -\frac{\hbar\theta_{SH} j_a}{2\mu_0 \left|e^-\right| M_s t}\mathbf{m}\times y \qquad \text{Equation 5-7}$$

where **m** is the magnetization, θ_{SH} is the spin Hall angle, j_a is the applied current density and t is the thickness of the magnetic material[27]. To enable efficient SOT-induced magnetization switching in perpendicular magnetic anisotropy (PMA) materials, the *z*-component in $\mathbf{H}_{SH}$ should be maximized by having large *x*-magnetization (m_x)[28-30]. It is then convenient to take advantage of the inherent edge magnetization tilting effect due to the DMI to produce a m_x.

In PMA ferromagnets with DMI, the magnetization at the edges experiences an in-plane tilt due to the boundary conditions imposed by the DMI. In the case of a nanowire along the *x*-axis, the magnitude of m_x due to edge magnetization tilting is given by:

$$m_x = L\frac{D}{2A} \qquad \text{Equation 5-8}$$

where L is the domain wall (DW) length, D is the DMI energy per unit area and A is the exchange stiffness[31-33]. By lowering the perpendicular magnetic anisotropy, thus increasing L, m_x is increased even further. More importantly, the DMI-induced edge tilting has a chirality and produces a m_x that is opposite in direction for the two SAF-coupled magnetic layers. This conveniently enables the magnetization of both SAF-coupled layers to be switched simultaneously using SOT, without requiring any bias field.

Figure 5-5(a) shows a SAF nanowire with the left and right halves having an anisotropy energy density of 300 and 600 kJ/m^3, respectively. Such localized reduction in PMA can be achieved experimentally by using a combination of ion implantation and lithography processes[34, 35]. Even though the magnetization of the top and bottom layers is opposite, the effective field from the spin Hall effect $(\mathbf{H}_{SH})$ always acts to reverse the magnetization at the edges. Furthermore, the lowered PMA allows $\mathbf{H}_{SH}$ to switch the magnetization without needing a high current density. Figure 5-5(b) shows that after nucleation of the first DW, it is driven to the right into the region of higher PMA by the spin Hall effective field. The magnetization at the left edge will tilt again when the DW is driven sufficiently far, and the cycle can be repeated indefinitely for continuous domain nucleation.

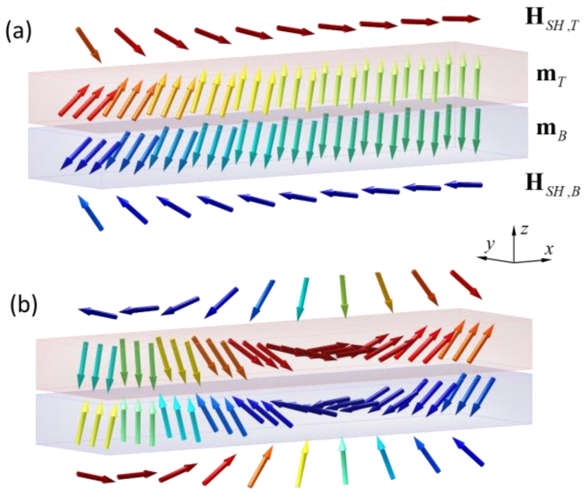

Figure 5-5 Schematic representations of the top $(\mathbf{m}_T)$ and bottom $(\mathbf{m}_B)$ magnetization of the synthetic antiferromagnet nanowire along with the spin Hall effective field $\mathbf{H}_{SH}$ acting on magnetizations. The colour of the arrows represents the m_z component. (a) Initial magnetization before application of current. Due to the lower K_u on the left, a significant magnetization edge tilting is observed while the high K_u on the right resists the edge tilting (b) Magnetization at 19 ps after application of current. The injected DW is driven along the +*x* direction.

5.4 Three terminal skyrmion device

To circumvent the topological protection of a skyrmion, the magnetization reversal process should be initiated at the edges where topological charge can be added without much energy costs.[36] In Figure 5-6(a), we show such a device where skyrmions can be injected via a 20 nm wide branch protruding from the 60 nm wide main nanowire. Positioned in the middle, the branch allows skyrmions to be injected in between skyrmions in a skyrmion chain. The limitations of standard fabrication techniques were also taken into consideration by rounding the inner corners of the device. In the branch, the PMA is reduced to take advantage of SOT for efficient in-line domain injection as described earlier. The device is operated by the application of pulsed current at each of the three terminals. To write a skyrmion, a positive voltage is applied to V_2 and V_3 while keeping V_1 grounded. Due to the small width (20 nm) of the nanowire branch, a high current density is experienced within the branch which conveniently allows rapid domain nucleation and thus skyrmion injection.

The skyrmion injection process can be summarized as the nucleation of two DWs, followed by their depinning at the branch junction, during which, the two DWs wrap around to combine and form a single skyrmion. Under a current density of 67 MA/cm^2, skyrmions are nucleated in less than 100 ps. To analyze the nucleation process, the current density is increased in small steps, allowing the individual depinning mechanisms to be observed. The simulation snapshots at various times of interest are shown in Figure 5-6 (b). Applying a current density of 36 MA/cm^2, the DMI-induced edge magnetization tilting allows the SOT to nucleate a DW, in the same way as shown in Figure 5-5. However, at the junction, there is a strong pinning field attributable to two sources. Firstly, the higher PMA in the nanowire, and secondly, the energy needed for DW bending and stretching. The latter can be seen from the crescent DW shape in the magnetization profile at the 15 ps snapshot. Without a higher current density, the DW remains pinned.

Since the skyrmion injection process involves the nucleation and propulsion of DWs, the magnetostatic energy of the system can be understood from the DW areal energy density given by,[21, 37]

$$\sigma = \frac{2A}{L} + 2K_{eff}L - D\pi \qquad \text{Equation 5-9}$$

where K_{eff} is the effective anisotropy considering the demagnetizing fields. When the DW is compressed, the exchange energy is increased at the expense of the anisotropy. The interplay between the two energies therefore signals any change in DW length. The magnetostatic energy of the system with respect to time is shown in Figure 5-6(c).

At 70 ps, the current density is increased to 49 MA/cm^2 to provide sufficient spin-torque for the nucleation of the second DW. As the second DW is pushed downwards, it interacts repulsively with the first DW which is apparent from the spike in the exchange energy and the fall in anisotropy energy. However, the pinning potential experienced by the first DW is still stronger than sum of the SOT force and repulsive interaction force received. With the final increase of current density to 67 MA/cm^2, an immediate spike in exchange energy is observed which is explained by the second DW exerting additional pressure on the first, due to the second DW experiencing the increased push from the SOT. At 275 ps, a third DW is nucleated which provides the last push required to depin the first two DWs from the junction and a skyrmion is expelled.

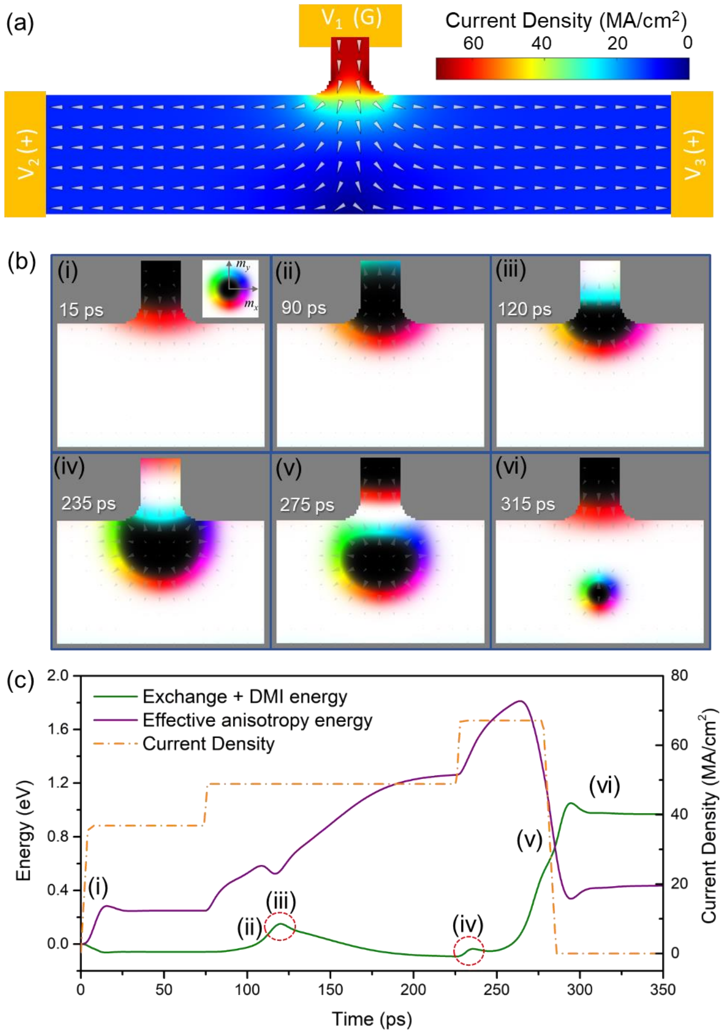

Figure 5-6 (a) Vector map of threshold current density applied for skyrmion injection. The arrows represent the electron flow direction. The main nanowire has a width of 60 nm and a length of 312 nm. (b) Simulation snapshots at the branch junction at various times during the injection process. (c) Magnetostatic energy and applied current density of the skyrmion device as a function of time during injection. Snapshots of interest from (b) are highlighted in roman numerals. The dotted red circles highlight the spike in exchange energy that is due to DW compression.

While the DWs must overcome multiple energy barriers to form a skyrmion, the threshold current density for skyrmion nucleation only depends on the amplitude of the highest barrier. Therefore, a single pulse with current density greater than 67 MA/cm^2 can also nucleate a skyrmion. The system energies over time is shown in Figure 5-7 below. The magnetization dynamics are very similar to in Figure 5-6 with the exception that the processes evolve in a much smoother fashion. As compared when a stepped current density is applied, the features in the energies are less visible as the DWs are only momentarily pinned. The possibility of using a single pulse for nucleation greatly reduces the complexity of operating the device.

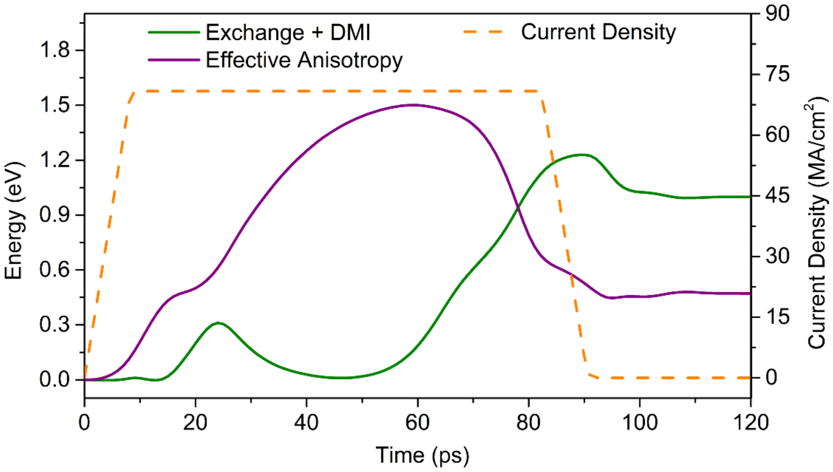

Figure 5-7 The different magnetostatic energies versus time in the skyrmion nucleation process. The applied current density (orange dashed line) has a rise/fall time of 10 ps.

5.5 Role of domain wall chain pressure in skyrmion nucleation

From the skyrmion injection process, it is apparent that the cumulative DW pressure helps to reduce the threshold injection current. The effect of having additional domain walls (n) in the branch was also studied. To prevent the nucleation of additional domain walls, a line of spins on the top of the branch were fixed to stop the SOT-induced domain wall nucleation. By doing so, the DMI-induced edge tilting is suppressed and nucleation of domain walls beyond what is needed is suppressed. The SOT is then unable to nucleate the third DW. With only two DWs (n = 0), the minimum required for skyrmion formation, the threshold injection current density was found to nearly triple to 163 MA/cm^2 as compared to the case of one additional DW (n = 1). Although more DWs can be added to the DW chain to further reduce the threshold skyrmion nucleation current density, it is necessary to increase the length of the branch to accommodate additional DWs which would increase the Joule heating losses and offset the gains in efficiency from the reduced threshold current density.

The dependence of the threshold injection current density on the branch width was also investigated. Increasing the branch width while keeping the main nanowire width constant, the threshold injection current density was found to decrease, as shown in Figure 5-8(a). However, there exists a limit for the maximum branch width. At widths of more than 40 nm, the first DW (DW1) depins much earlier than the second DW (DW2). Consequently, the two DWs do not join to form a skyrmion as shown in Figure 5-9(a, c). The phenomenon can be understood from the current density distribution where most of the current is concentrated at the branch corners as highlighted in Figure 5-9(d). Therefore, in wide branches, DWs are depinned more easily. On the other hand, branches that are narrower than 16 nm have a relatively uniform current density and do not suffer from this mode of failure. Instead, the narrower branches cause the main nanowire to receive a relatively low amount of current. Therefore, when the first domain wall is pushed into the main nanowire, the first DW does not receive much propagation force. As a result, the DWs in a narrow branch require an unrealistically high current density to depin.

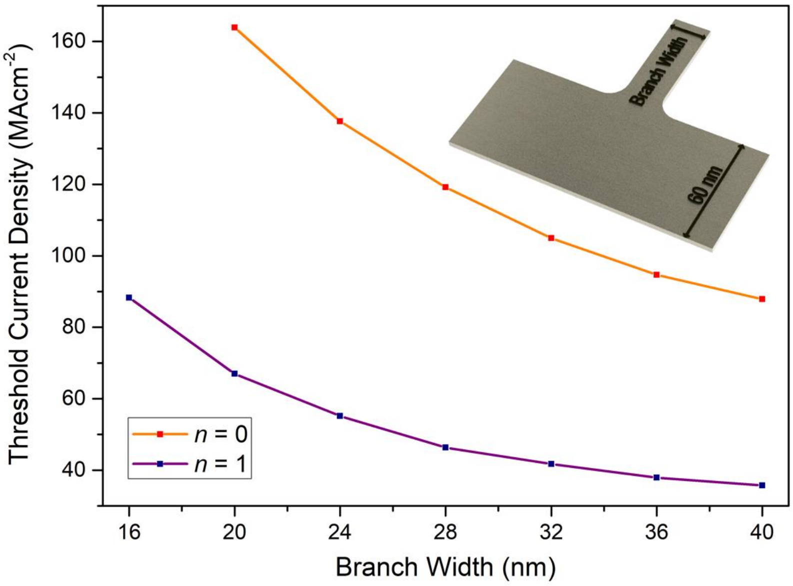

Figure 5-8 Graph of threshold current density required for skyrmion injection as a function of branch width. *n* is the number of additional domain walls injected. Inset shows the dimensions of the nanostructure studied.

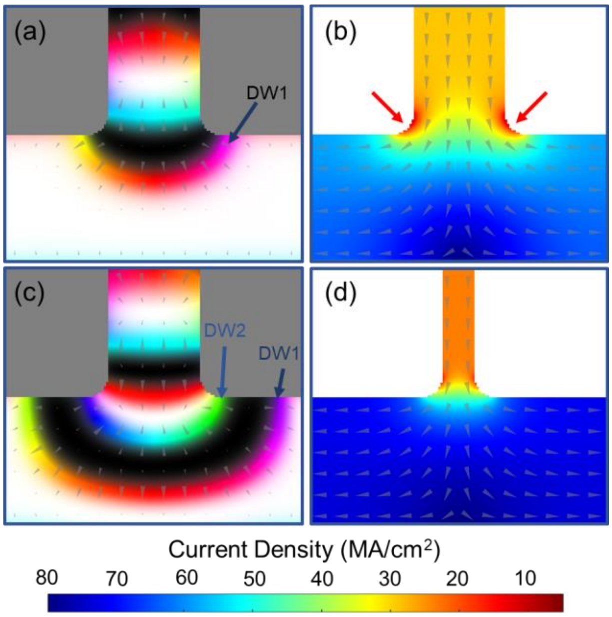

Figure 5-9 (a-b) Simulation snapshots of a failed injection attempt in the 44 nm wide branch nanostructure. Current density distribution in (c) 44 nm wide and (d) 16 nm wide nanostructure. The same colourmap is used for both.

The branched nanowire geometry is not only able to achieve efficient skyrmion injection, but it also allows for bit shift and delete operations. By changing the pulse amplitudes of $V_{1\text{-}3}$, the write, shift, and delete operations can be performed. In

Figure 5-10, we demonstrate the writing of two skyrmions (i-iv) followed by a shift operation (v) and finally the deletion of the first skyrmion (vi). Skyrmion shifting is achieved by the application of a current density along the axis of the nanowire. Due to the right-handed skyrmion chirality induced by the DMI and also the positive spin Hall angle, the skyrmion moves in the direction of the electron flow[1].

The delete operation is the reverse of the write operation; the skyrmion is instead drawn towards the branch where it eventually annihilates. The magnetostatic energy during the process is shown in Figure 5-11. For reference, the magnetization snapshot at Figure 5-10(vi) is taken at 412 ps. For the shift and delete operations, the threshold current density is less than 20 MA/cm^2 which is significantly less than the threshold skyrmion injection current. The difference is due to the reduced pinning force; moving from the high PMA nanowire into the low PMA branch is energetically more favourable. While the nucleation and manipulation of only two skyrmions were demonstrated, the proposed device has a storage capacity that is similar to the well-studied skyrmion racetrack memory devices[5, 8, 11].

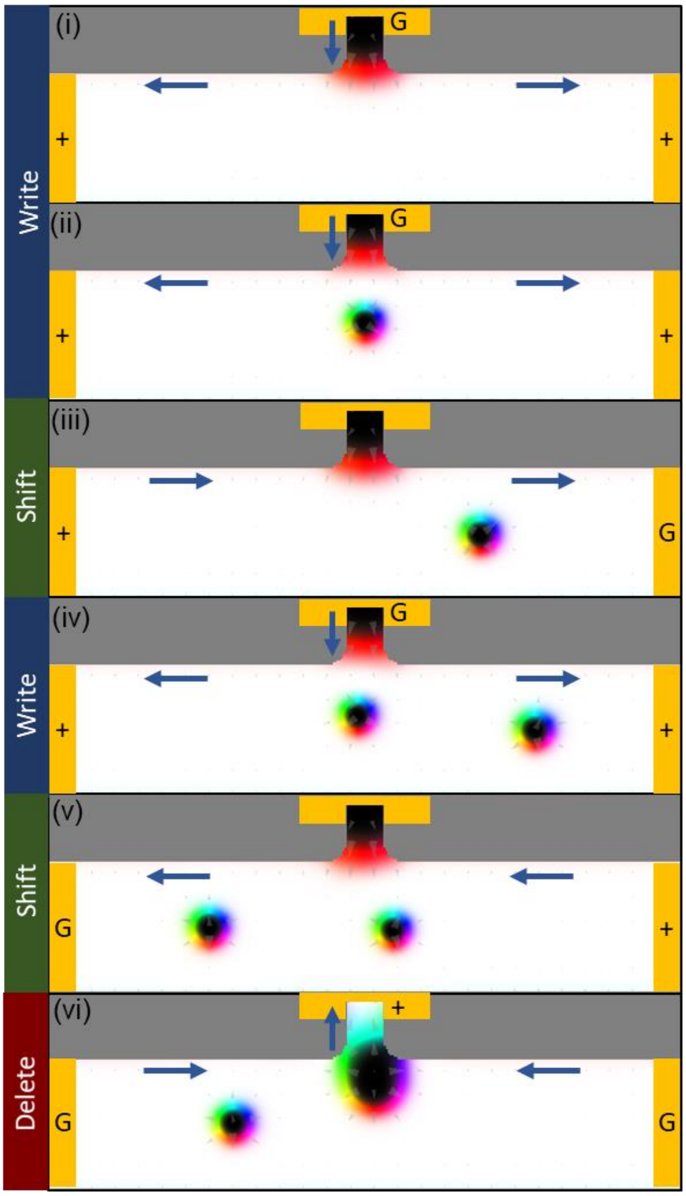

Figure 5-10 Demonstration of write/shift/delete operations of the branched nanowire device. Each operation is accomplished by changing the voltage at each of the three terminals (gold). The blue arrows indicate the direction of the current flow.

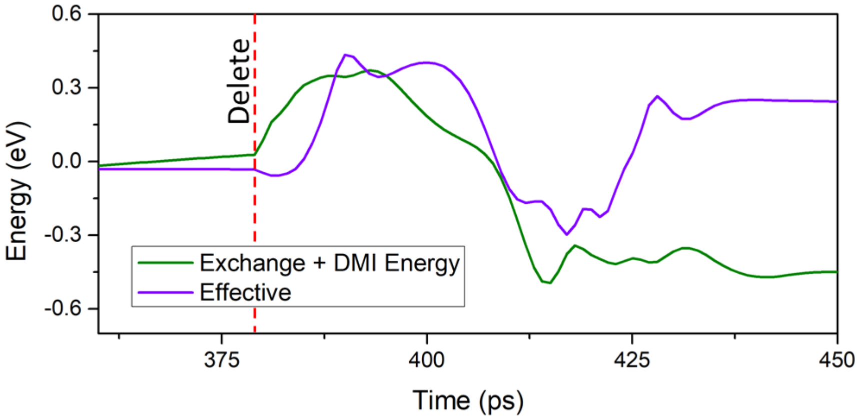

Figure 5-11 Magnetostatic energy profile during delete operation. The start of the delete pulse was applied at 380 ps and marked with red dotted lines.

5.6 Domain walls as magnetic springs

The DW magnetization profile was studied as a function of the number of DWs in the chain. A SAF nanowire with an anisotropy step was considered as shown in Figure 5-12. The anisotropy step represents an energy barrier that pins the leading DW if insufficient spin-orbit torque is supplied. Under a current density of 30 MA/cm^2, the number of DWs in the chain was gradually incremented. Figure 5-12 shows the equilibrium magnetization configuration. As more DWs were added, the leading DWs becomes increasingly compressed. Unsurprisingly, when increasing the current density to 40 and 50 MA/cm^2, the DW chain compression also increases. It can be concluded that the compression arises from the spin-orbit torques experienced by the DWs.

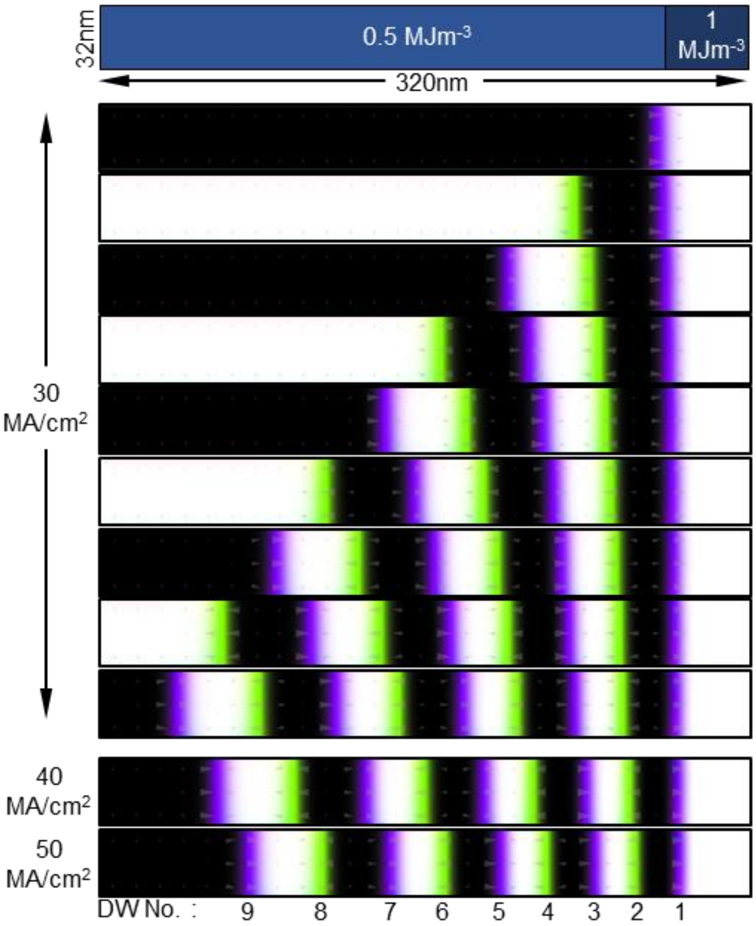

Figure 5-12 Magnetization snapshots of nanowires containing varying numbers of DWs at 30 MA/cm^2 and nine DWs at 40 and 50 MA/cm^2.

By calculating the DW length from micromagnetic simulations, the DW compression can be quantified. In Figure 5-12(b), an increase in current density compresses each DW in the chain non-uniformly, with the first DW experiencing the most compression and slightly less for each DW that follows. This suggests that each DW up the chain experiences the cumulative force that acts on the previous DWs. Figure 5-12(c) shows the magnetostatic energy of each DW in the system. As the DWs become increasingly compressed, anisotropy energy is decreased. However, the energy change is offset by the increase in exchange energy, resulting in a net linear increase of energy in the system. The change in magnetostatic energy is consistent with the DW areal energy density given by Equation 5-9.

Néel DWs are known to tilt when a spin-orbit torque effective field is applied. However, in a SAF nanowire, the tilt of the top and bottom DWs cancels out and results in a DW with no tilt. Therefore, the SAF DW chain system is reminiscent of a vertical stack of mechanical springs; each spring experiences a gravitational force F_1 and the gravitational force from all the springs above, culminating in the bottom-most spring acquiring the most compression energy. Substituting the equilibrium DW length $L_{eq} = \sqrt{\frac{A}{K_{eff}}}$ into Equation 5-9, the Maclaurin's series read:

$$\sigma(\Delta L) = \sigma_{eq} + 2\sqrt{\frac{K^3}{A}}\Delta L^2 + O\left(\Delta L^3\right) \qquad \text{Equation 5-10}$$

where ΔL is the change in DW length caused by the compression and σ_{eq} is the DW energy at equilibrium which is calculated to be 0.317 eV for the geometry and material parameters used in our study.

In Figure 5-13(a), we show that the spin torque-induced DW compression can indeed be modelled like the compression of a mechanical spring; in the form of a quadratic relation between energy stored and compression length using Equation 5-10. The slight y offset between the analytical and numerical data can be explained by the DWs experiencing a DMI-induced edge tilting along the y-axis which results in increased anisotropy energy. Nonetheless, the energy offset is less than 5%. The coefficient of the quadratic term was also found to be different by no more than 1%. The surprisingly good fit between the numerical data and our spring model demonstrates that the energy changes due to the application of spin torques can be completely accounted for by DW compression.

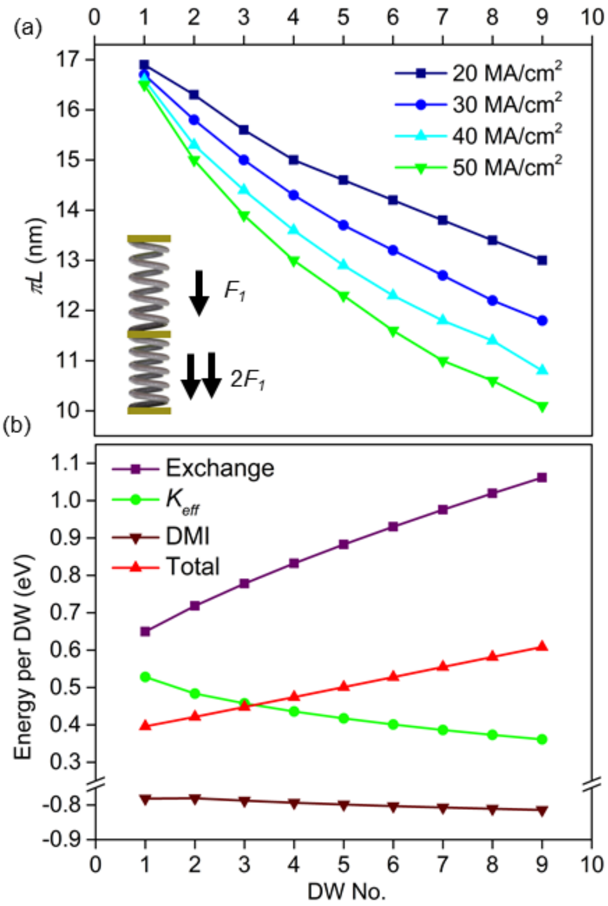

Figure 5-13 (a) Characteristic DW length as a function of current density and number of DWs. Bottom inset shows a similar mechanical spring analogue of the DW system. (b) Energy per DW for each additional DW added to a nanowire at 30 MA/cm^2.

Under a spin torque compression, the DWs accumulate energy which is then used to overcome pinning potentials. With a quadratic spring model, it becomes possible to obtain the compression energy of the DWs using only the changes in DW lengths. The compression energy of the leading DW was obtained as a function of applied current density and number of DW in the chain, as shown in Figure 5-14(b). The compression energy was found to scale linearly with both the current density and number of DWs. The number of DWs therefore acts as a multiplier to the amount of spin-torque experienced by the leading DW. As a result, the combination of a high current density and a long DW chain can produce a compression energy that is equal or more than the DW equilibrium energy.

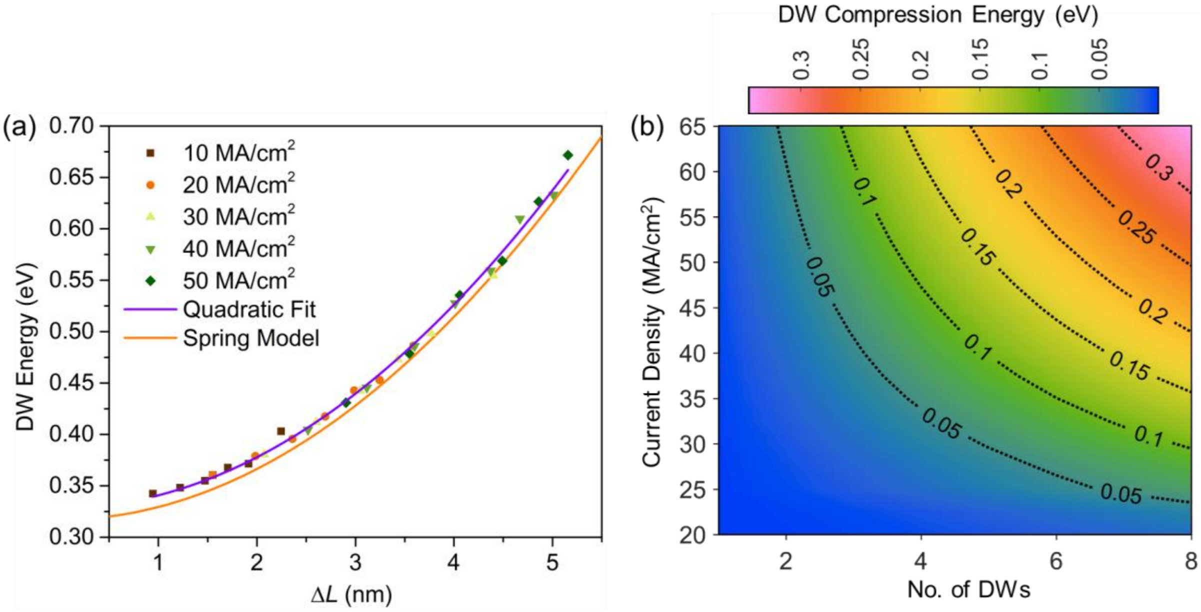

Figure 5-14 (a) DW energy extracted from micromagnetic simulations at various current densities versus the DW compression length ΔL. The spring model is the analytic function plotted from Equation 5-10. (b) 2D map of DW compression energy stored in the leading DW as a function of current density and number of DWs.

5.7 Summary

In this chapter, we have demonstrated a highly efficient in-line skyrmion injection method using a branched nanowire geometry in a synthetic antiferromagnet system. The exploitation of DMI-induced edge tilting and efficient SOTs allowed DWs to be injected efficiently into the branch. Further accumulating DWs in the branch created a compression of the leading DW, which provides the required energy to depin at the branch junction. The compression mechanism resulted in the reduction of the threshold injection current density by a third. The branched device can also function as a skyrmion memory cell that uses only three terminals to accomplish the shift/delete/write operations. Lastly, we have also investigated the DW compression and found that the DW chain acts as a mechanical spring when compressed, storing energy. This discovery can reduce the depinning current density in DW logic and memory devices, thus improving energy efficiency.

References

1. X. Zhang, Y. Zhou and M. Ezawa, *Nature Communications*, 2016, **7**, 10293.
2. R. Tomasello, V. Puliafito, E. Martinez, A. Manchon, M. Ricci, M. Carpentieri and G. Finocchio, *Journal of Physics D: Applied Physics*, 2017, **50**, 325302.
3. S. F. Zhang, W. L. Gan, J. Kwon, F. L. Luo, G. J. Lim, J. B. Wang and W. S. Lew, *Scientific Reports*, 2016, **6**, 24804.
4. C. Guite, I. S. Kerk, M. C. Sekhar, M. Ramu, S. Goolaup and W. S. Lew, *Scientific Reports*, 2014, **4**, 7459.
5. Y. Zhang, S. Luo, B. Yan, J. Ou-Yang, X. Yang, S. Chen, B. Zhu and L. You, *Nanoscale*, 2017, DOI: 10.1039/C7NR01980G.
6. G. Yu, P. Upadhyaya, Q. Shao, H. Wu, G. Yin, X. Li, C. He, W. Jiang, X. Han, P. K. Amiri and K. L. Wang, *Nano Letters*, 2017, **17**, 261-268.
7. A. Fert, N. Reyren and V. Cros, *Nature Reviews Materials*, 2017, **2**, 17031.
8. S. Woo, K. Litzius, B. Kruger, M.-Y. Im, L. Caretta, K. Richter, M. Mann, A. Krone, R. M. Reeve, M. Weigand, P. Agrawal, I. Lemesh, M.-A. Mawass, P. Fischer, M. Klaui and G. S. D. Beach, *Nat Mater*, 2016, **15**, 501-506.
9. H. T. Fook, W. L. Gan and W. S. Lew, *Scientific Reports*, 2016, **6**, 21099.
10. I. Purnama, W. L. Gan, D. W. Wong and W. S. Lew, *Scientific Reports*, 2015, **5**, 10620.
11. J. Sampaio, V. Cros, S. Rohart, A. Thiaville and A. Fert, *Nature Nanotechnology*, 2013, **8**, 839-844.
12. W. Koshibae and N. Nagaosa, *Scientific Reports*, 2017, **7**.
13. S.-H. Yang, K.-S. Ryu and S. Parkin, *Nature Nanotechnology*, 2015, **10**, 221-226.
14. M. J. Donahue, *Journal of Applied Physics*, 1998, **83**, 6491-6493.
15. S. S. P. Parkin, N. More and K. P. Roche, *Physical Review Letters*, 1990, **64**, 2304-2307.
16. D. H. Kim, K. W. Moon, S. C. Yoo, B. C. Min, K. H. Shin and S. B. Choe, *Ieee Transactions on Magnetics*, 2013, **49**, 3207-3210.
17. J. Curiale, A. Lemaître, T. Niazi, G. Faini and V. Jeudy, *Journal of Applied Physics*, 2012, **112**, 103922.
18. K.-J. Kim, J.-C. Lee, S.-B. Choe and K.-H. Shin, *Applied Physics Letters*, 2008, **92**, 192509.
19. A. Yamaguchi, S. Nasu, H. Tanigawa, T. Ono, K. Miyake, K. Mibu and T. Shinjo, *Applied Physics Letters*, 2005, **86**, 012511.
20. S. Grytsyuk, A. Belabbes, P. M. Haney, H. W. Lee, K. J. Lee, M. D. Stiles, U. Schwingenschogl and A. Manchon, *Physical Review B*, 2016, **93**.

21. M. D. DeJong and K. L. Livesey, *Physical Review B*, 2015, **92**.

22. S. Li, S. Goolaup, J. Kwon, F. Luo, W. Gan and W. S. Lew, *Scientific Reports*, 2017, **7**, 972.

23. C. Engel, S. Goolaup, F. Luo, W. Gan and W. S. Lew, *Journal of Applied Physics*, 2017, **121**, 143902.

24. C. Zhang, S. Fukami, H. Sato, F. Matsukura and H. Ohno, *Applied Physics Letters*, 2015, **107**, 012401.

25. Y. Fan, P. Upadhyaya, X. Kou, M. Lang, S. Takei, Z. Wang, J. Tang, L. He, L. T. Chang, M. Montazeri, G. Yu, W. Jiang, T. Nie, R. N. Schwartz, Y. Tserkovnyak and K. L. Wang, *Nature materials*, 2014, **13**, 699-704.

26. M. Cubukcu, O. Boulle, M. Drouard, K. Garello, C. Onur Avci, I. Mihai Miron, J. Langer, B. Ocker, P. Gambardella and G. Gaudin, *Applied Physics Letters*, 2014, **104**, 042406.

27. E. Martinez, S. Emori and G. S. D. Beach, *Applied Physics Letters*, 2013, **103**, 072406.

28. Y. W. Oh, S. H. Chris Baek, Y. M. Kim, H. Y. Lee, K. D. Lee, C. G. Yang, E. S. Park, K. S. Lee, K. W. Kim, G. Go, J. R. Jeong, B. C. Min, H. W. Lee, K. J. Lee and B. G. Park, *Nature Nanotechnology*, 2016, **11**, 878-884.

29. Y. C. Lau, D. Betto, K. Rode, J. M. Coey and P. Stamenov, *Nature Nanotechnology*, 2016, **11**, 758-762.

30. G. Yu, P. Upadhyaya, Y. Fan, J. G. Alzate, W. Jiang, K. L. Wong, S. Takei, S. A. Bender, L. T. Chang, Y. Jiang, M. Lang, J. Tang, Y. Wang, Y. Tserkovnyak, P. K. Amiri and K. L. Wang, *Nature Nanotechnology*, 2014, **9**, 548-554.

31. D. S. Han, N. H. Kim, J. S. Kim, Y. Yin, J. W. Koo, J. Cho, S. Lee, M. Klaui, H. J. Swagten, B. Koopmans and C. Y. You, *Nano Letters*, 2016, **16**, 4438-4446.

32. S. Pizzini, J. Vogel, S. Rohart, L. D. Buda-Prejbeanu, E. Jue, O. Boulle, I. M. Miron, C. K. Safeer, S. Auffret, G. Gaudin and A. Thiaville, *Physical Review Letters*, 2014, **113**, 047203.

33. S. Rohart and A. Thiaville, *Physical Review B*, 2013, **88**.

34. T. Devolder, C. Chappert, Y. Chen, E. Cambril, H. Launois, H. Bernas, J. Ferré and J. P. Jamet, *Journal of Vacuum Science & Technology B: Microelectronics and Nanometer Structures*, 1999, **17**, 3177.

35. T. Devolder, C. Chappert, Y. Chen, E. Cambril, H. Bernas, J. P. Jamet and J. Ferré, *Applied Physics Letters*, 1999, **74**, 3383-3385.

36. D. Cortes-Ortuno, W. Wang, M. Beg, R. A. Pepper, M. A. Bisotti, R. Carey, M. Vousden, T. Kluyver, O. Hovorka and H. Fangohr, *Scientific Reports*, 2017, **7**, 4060.

37. M. D. DeJong and K. L. Livesey, *Physical Review B*, 2017, **95**, 054424.

Chapter 6 Conclusion and Future Works

6.1 Summary of the Thesis

To use skyrmions as information carriers in memory devices, a reliable means of skyrmion transportation has to be developed. Throughout the thesis, various skyrmion transport methods were studied theoretically and several different types of devices were conceived and demonstrated numerically. One of the most convenient methods is by using spin-orbit torques when the current source can be applied across the skyrmion racetrack. While this transport method has been demonstrated in various experiments,[1-3] the theoretical understanding is quite lacking. In Chapter 3, the skyrmion equation of motion under an applied spin-orbit torque was modelled by using the Thiele approach. Using several approximations, the model was simplified into a linear form:

$$\mathbf{F}_{\mathbf{SHE}} = p\frac{\hbar\theta_H j}{2e}\left(\pi^2 c\right)\left(\cos q\hat{\mathbf{x}} - \sin q\hat{\mathbf{y}}\right) \qquad \text{Equation 6-1}$$

Equation 6-1 shows that the propagative spin Hall force scales linearly with skyrmion radius (c) and that the spin Hall force always acts collinearly or transversely with respect to the applied current density. The first result predicts a poor scaling of skyrmion-based devices at the limit of atomistic skyrmions. To improve the skyrmion speeds, the latter result from our model can be exploited; by choosing the right skyrmion type, the skyrmion can receive an additional propagative force from the repulsive edge forces. This type of amplification was found to be about size times. Choosing the wrong skyrmion type could result in zero net propagative force.

In Chapter 4, the use of anisotropy gradients to generate propagative forces were investigated. The anisotropy gradients were found to be able to move skyrmions as quickly as spin-orbit torques. However, creating an anisotropy gradient across long distances is a challenge for two reasons. Firstly, the fabrication process in creating sloped dielectric layers can be a challenge. Secondly, the skyrmions only exist in a finite anisotropy range. Long gradients can result in anisotropy energies too large/small for sustaining skyrmions. Therefore, a discrete VCMA gate array device was proposed.[4] By applying different voltages to adjacent gate electrodes, an anisotropy gradient can be created and thus a force acting along the nanowire axis can be exerted. The device was found to be very versatile; it enables closed-loop operation where after shifting across all locations, the entire skyrmion chain is returned to its original position.

To reduce the device complexity and skyrmion Hall angle, a single gate electrode providing transversely-oriented force was studied. In such a scheme, the skyrmions moved in a predictable manner, close to the centerline of the nanowire. With the flexibility offered by the VCMA-gradient devices, a mix of longitudinal and transverse driving forces can also be applied. Such a device is used to shape the skyrmion's trajectory such that an initial upwards velocity is acquired to avoid the pinning site. The hybrid skyrmion ratchet device is able to propel skyrmions three times faster than if only a transverse force is used.

In Chapter 5, the discussion shifts to antiferromagnetically-coupled skyrmions driven by spin-orbit torques. Such skyrmions exhibit many positive characteristics but are limited by their limited nucleation options. One very advantageous characteristic is the greatly amplified skyrmion velocity as compared to ferromagnetic skyrmions,[5, 6] which is attributed to the antiferromagnetically-coupled skyrmions' mutually attractively coupling. An injection method using spin Hall torque was proposed. Due to the spin Hall torque's dependence on magnetization direction, it is possible to exert opposite torques on opposite magnetization, thus achieving switching in the antiferromagnetically-coupled thin film. The injection method was implemented in a three-terminal device. To improve the injection efficiency, cumulative domain pressure was investigated for use in domain depinning. When multiple domain walls are on the branch, it was found that the depinning current density decreased by 60% that translates into an injection energy reduction of 84%.

In this thesis, extensive studies in the area of skyrmion transport and nucleation were performed with the ultimate aim of enabling high-performance skyrmion memory devices. The conclusions derived in the work here enables a myriad of other works to be performed, both theoretical and experimental.

6.2 Future works

In this section, several ideas building upon our theoretical methods and device architectures will be discussed. In Chapter 4, the equations derived can be applied to not just anisotropy energy gradients but also to other types of magnetostatic energy gradients; the driving force from a gradient in saturation magnetization, film thickness or exchange stiffness and any material parameter can be calculated similarly to in Chapter 4. Therefore, the theoretical understanding of most types of driving forces has been uncovered. However, an important and inevitable type of driving force is due to thermal gradients.

6.2.1 Skyrmions in a thermal gradient

In applying electrical fields or currents to skyrmion devices, it is inevitable that thermal gradients will arise due to local Joule heating. The effect of temperature on skyrmion dynamics has been studied by some.[7-10] While not exactly an effective or efficient method to drive skyrmions, thermal gradients can produce an unwanted driving force on the skyrmions which can reduce device reliability. In Figure 6-1, the skyrmion magnetization driven by a thermal gradient is shown. It was suggested that under a thermal gradient, there will be a non-uniform generation of thermally-generated magnons. A net magnon flow then arises. Due to the non-zero spin of the magnons, they can exert a spin transfer torque on the local magnetization and propel the skyrmions.[11] However, we propose that the theory is incomplete and that the temperature also induces changes in material parameters.

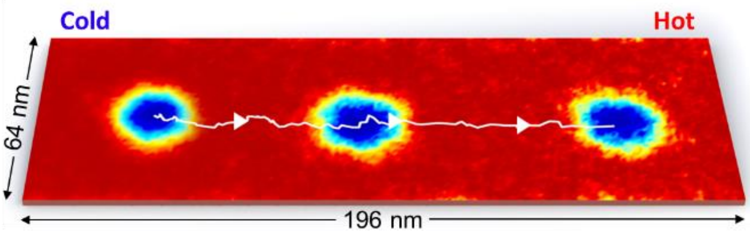

Figure 6-1 Schematic illustration of the skyrmion magnetization on a substrate with a temperature gradient. The temperature gradient drives the skyrmion rightwards as highlighted by the white line.

In Figure 6-2, our initial investigation shows that the temperature-induced reduction in anisotropy is sufficient to account for most of the thermally-induced skyrmion propagation. The anisotropy at different temperatures was calculated from micromagnetics by measuring the hard axis hysteresis at different temperatures. An important reason to derive the contribution of various effects in the thermal gradient-induced skyrmion driving is such that the skyrmion velocity will scale correctly with different parameters. The Thiele equation for spin transfer torque does not depend on the skyrmion radius directly,[12] while the anisotropy-gradient force scales with skyrmion radius. A modified theoretical model can be developed to explain for the discrepancies observed in the current models, especially when the skyrmion size is changing.

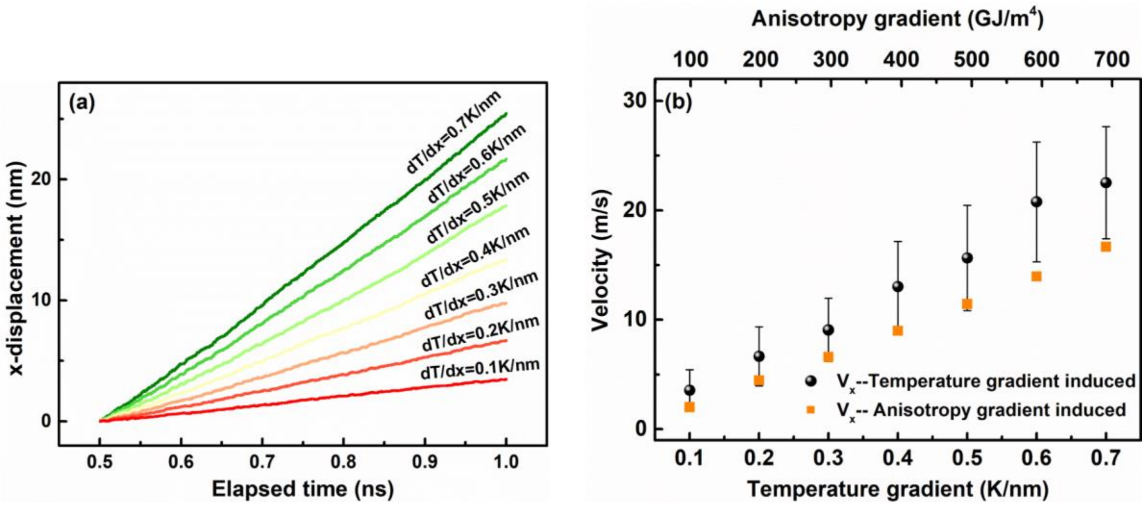

Figure 6-2 (a) Displacement of skyrmions due to temperature gradients of different magnitudes. (b) Skyrmion velocity versus temperature gradients and versus anisotropy gradients.

6.2.2 Experimental verification of skyrmion velocity dependence on radius when under spin-orbit torques

In Chapter 3, the skyrmion velocity was predicted to be linear with the skyrmion radius. This was further confirmed in micromagnetic studies. However, it should be possible to test the model in experiments. To be able to image skyrmions and measure their velocity, extensive efforts have been devoted to constructing a Kerr microscope. The Kerr microscope measures and images the Kerr rotation in polarization induced by the magnet, as shown in Figure 6-3(a). The advantage of Kerr microscope is that it can take as little as 100 ms to form an image and does not require high vacuum nor expensive vibration isolation solutions. Meanwhile, as long as skyrmions are not spaced within 250 nm (the optical resolution), the Kerr microscope can identify the skyrmion size and position with nanometer resolution.[13]

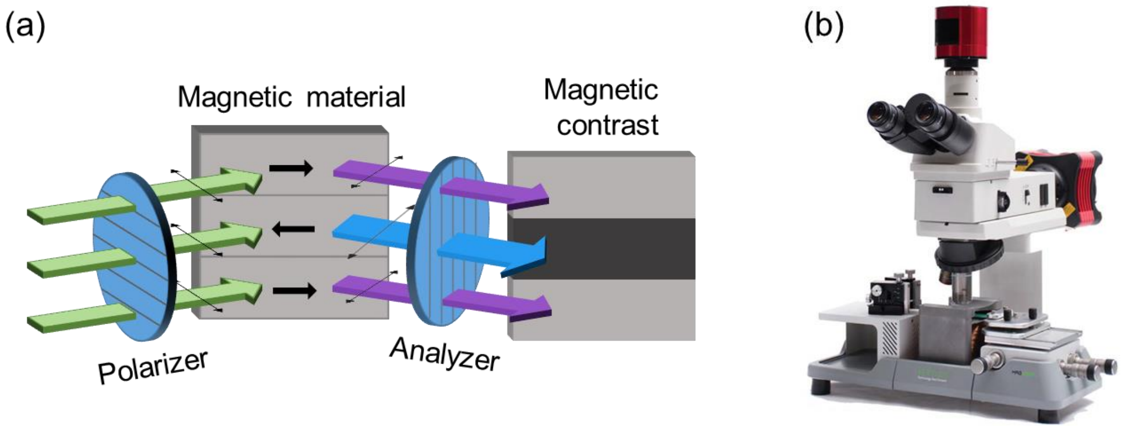

Figure 6-3 (a) Schematic illustration of the operation principle of a Kerr microscope. (b) The Kerr microscope constructed for imaging magnetic skyrmions.

To test the velocity-radius relation, an external magnetic field can be applied, such that the size of skyrmions can be changed.[1] This is shown in Figure 3-4. By sweeping the magnetic field over a wide range and measuring the skyrmion speeds, a linear trend should be observed. If indeed the skyrmion can be sped up by expanding its size, a new class of devices can be developed that temporarily enlarges the skyrmion to benefit from the increased propagation velocity. Such a mechanism could make use of the VCMA effect to speed up antiferromagnetically-coupled skyrmions. Therefore, this simple experiment can potentially unlock higher skyrmion speeds in skyrmion devices.

6.2.3 Experimental realization of antiferromagnetically-coupled skyrmions

In Chapter 4, the advantages of using antiferromagnetically-coupled (AFC) skyrmions are only briefly discussed. It cannot be stressed sufficiently how AFC skyrmions could be a game-changer for skyrmions. Recent skyrmion research has shown great interest in ferrimagnetic materials.[14, 15] In theory, the ferrimagnetic skyrmions would also possess many of the advantages of AFC skyrmions. However, it poses a significant challenge in its electrical detection. Due to the ferrimagnet’s close to net-zero magnetization, tunnelling magnetoresistance sensors would only produce a small change in resistance when the ferrimagnet’s magnetization is flipped. In contrast, the tunnelling spin-polarized current will always interface with a ferromagnetic layer in AFC materials, thus resulting in much larger magnetoresistance changes.

The first prediction for AFC skyrmions is that the skyrmion Hall angle should be proportional to the net magnetization of the individual layers combined. The force due to spin-orbit torque is dependent on the total magnetization $M_s t_F$. Therefore, the SkHE should be dependent on the total magnetization. When the AFC medium is fully compensated, the SkHE should vanish, while the skyrmion should still be detectable by a magnetoresistance sensor.

The AFC medium requires a relatively strong perpendicular magnetic anisotropy, a high DMI, produce a strong spin-orbit torque, and the heavy metal also needs to produce RKKY-coupling. An interesting candidate for AFC skyrmions would be Pt/Co/Fe/Ir/Fe/Co/Pt. Skyrmions have been shown to exist in Ir/Fe/Co/Pt multilayers,[16, 17] which indicates that the proposed multilayer could possess the correct material parameters to sustain skyrmions. In the multilayer, iridium acts as the heavy metal for RKKY-coupling while providing DMI and spin-orbit torque.[18]

References

1. G. Yu, P. Upadhyaya, X. Li, W. Li, S. K. Kim, Y. Fan, K. L. Wong, Y. Tserkovnyak, P. K. Amiri and K. L. Wang, *Nano Letters*, 2016, **16**, 1981-1988.
2. S. Woo, K. Litzius, B. Krüger, M.-Y. Im, L. Caretta, K. Richter, M. Mann, A. Krone, R. M. Reeve, M. Weigand, P. Agrawal, I. Lemesh, M.-A. Mawass, P. Fischer, M. Kläui and G. S. D. Beach, *Nature materials*, 2016, **15**, 501.
3. K. Litzius, I. Lemesh, B. Krüger, P. Bassirian, L. Caretta, K. Richter, F. Büttner, K. Sato, O. A. Tretiakov, J. Förster, R. M. Reeve, M. Weigand, I. Bykova, H. Stoll, G. Schütz, G. S. D. Beach and M. Kläui, *Nature Physics*, 2016, **13**, 170.
4. X. Wang, W. L. Gan, J. C. Martinez, F. N. Tan, M. B. A. Jalil and W. S. Lew, *Nanoscale*, 2018, **10**, 733-740.
5. X. Zhang, Y. Zhou and M. Ezawa, *Nature Communications*, 2016, **7**, 10293.
6. R. Tomasello, V. Puliafito, E. Martinez, A. Manchon, M. Ricci, M. Carpentieri and G. Finocchio, *Journal of Physics D: Applied Physics*, 2017, **50**, 325302.
7. D. Cortes-Ortuno, W. Wang, M. Beg, R. A. Pepper, M. A. Bisotti, R. Carey, M. Vousden, T. Kluyver, O. Hovorka and H. Fangohr, *Scientific Reports*, 2017, **7**, 4060.
8. M. Mochizuki, X. Z. Yu, S. Seki, N. Kanazawa, W. Koshibae, J. Zang, M. Mostovoy, Y. Tokura and N. Nagaosa, *Nature materials*, 2014, **13**, 241.
9. J. Zázvorka, F. Jakobs, D. Heinze, N. Keil, S. Kromin, S. Jaiswal, K. Litzius, G. Jakob, P. Virnau, D. Pinna, K. Everschor-Sitte, L. Rózsa, A. Donges, U. Nowak and M. Kläui, *Nature Nanotechnology*, 2019, **14**, 658-661.
10. L. Kong and J. Zang, *Physical Review Letters*, 2013, **111**, 067203.
11. C. Schütte and M. Garst, *Physical Review B*, 2014, **90**, 094423.
12. J. Iwasaki, M. Mochizuki and N. Nagaosa, *Nature Nanotechnology*, 2013, **8**, 742-747.
13. I. Soldatov, W. Jiang, S. Te Velthuis, A. Hoffmann and R. Schäfer, *Applied Physics Letters*, 2018, **112**, 262404.
14. S. Woo, K. M. Song, X. Zhang, Y. Zhou, M. Ezawa, X. Liu, S. Finizio, J. Raabe, N. J. Lee and S.-I. Kim, *Nature Communications*, 2018, **9**, 959.
15. L. Caretta, M. Mann, F. Büttner, K. Ueda, B. Pfau, C. M. Günther, P. Hessing, A. Churikova, C. Klose, M. Schneider, D. Engel, C. Marcus, D. Bono, K. Bagschik, S. Eisebitt and G. S. D. Beach, *Nature Nanotechnology*, 2018, **13**, 1154-1160.
16. C. Moreau-Luchaire, S. C. Mouta, N. Reyren, J. Sampaio, C. A. Vaz, N. Van Horne, K. Bouzehouane, K. Garcia, C. Deranlot, P. Warnicke, P. Wohlhuter, J. M. George, M. Weigand, J. Raabe, V. Cros and A. Fert, *Nature Nanotechnology*, 2016, **11**, 444-448.

17. A. Soumyanarayanan, M. Raju, A. L. Gonzalez Oyarce, A. K. C. Tan, M.-Y. Im, A. P. Petrović, P. Ho, K. H. Khoo, M. Tran, C. K. Gan, F. Ernult and C. Panagopoulos, *Nature materials*, 2017, **16**, 898.

18. Y. Liu, B. Zhou and J.-G. Zhu, *Scientific Reports*, 2019, **9**, 325.

List of Publications

1. **Weiliang Gan**, Sachin Krishnia, and Lew Wen Siang, "Efficient in-line skyrmion injection method for synthetic antiferromagnetic systems", New Journal of Physics, 20,013029 (2018).

2. **Weiliang Gan**, Calvin Ang Ching Ian, Wang Xuan, and Lew Wen Siang, "Skyrmion ratchet for single-electrode skyrmion transport", submitted.

3. **Weiliang Gan**, Indra Purnama, Jose Chan Martinez, Tomoyasu Taniyama and Lew Wen Siang, "An accurate model for skyrmion dynamics under spin-orbit torques", submitted.

4. **Weiliang Gan**, Chandrasekhar Murapaka, Wong De Wei, Indra Purnama, Chiam Sing Yang, Nancy Wong Lai Mun and Lew Wen Siang, "Multi-vortex states in magnetic nanoparticles", Applied Physics Letters, 105,152405 (2014).

5. Indra Purnama*, **Weiliang Gan***, Wong De Wei, and Lew Wen Siang, "Guided current-induced skyrmion motion in a 1D potential well", Scientific Reports, 5, 10620 (2015).

6. Wang Xuan*, **Weiliang Gan***, Jose Chan Martinez, Tan Funan, M. B. A. Jalil and, Lew Wen Siang, "Efficient skyrmion transport mediated by voltage-controlled magnetic anisotropy gradient", Nanoscale, 10, 733-740 (2018), DOI: 10.1039/C7NR06482A

7. Senfu Zhang*, **Weiliang Gan***, J. Kwon, Luo Feilong, Gerard Joseph Lim Chu Keong, Wang Jianbo, and Lew Wen Siang, "Highly efficient domain walls injection in perpendicular magnetic anisotropy memory devices", Scientific Reports, 6, 24804 (2016).

8. Wong De Wei, Chandrasekhar Murapaka, **Weiliang Gan**, Indra Purnama and Lew Wen Siang, "Dynamics of three-dimensional helical domain wall in cylindrical NiFe nanowires", Journal of Applied Physics, 117, 17A747(2015).

9. Hiu Tong Fook, **Weiliang Gan**, Indra Purnama, and Lew Wen Siang, "Mitigation of Magnus force in current-induced skyrmion dynamics", IEEE Transactions on Magnetics, 51, No.11, 1500204 (2015).

10. Mansoor Bin Abdul Jalil, Seng Ghee Tan, Zuo Bin Siu, **Weiliang Gan**, Indra Purnama, and Lew Wen Siang, "Stability of topological charge of magnetic skyrmion configuration", Journal of Magnetism and Magnetic Materials, 399, 155 (2016).

11. Hiu Tung Fook, **Wei Liang Gan**, and Wen Siang Lew, "Gated skyrmion transport via field-induced potential barrier modulation", Scientific Reports, 6, 21099 (2016).

12. Wong De Wei, Indra Purnama, Gerard Joseph Lim Chu Keong, **Weiliang Gan**, Chandrasekhar Murapaka and Lew Wen Siang, "Current-induced three-dimensional domain

---

[*] These authors contributed equally to the work

wall propagation in cylindrical NiFe nanowires", Journal of Applied Physics, 119, 153902 (2016).

13. Fusheng Ma, Charles Reichhardt, **Weiliang Gan**, Cynthia J. Olson Reichhardt, and Wen Siang Lew, "Emergent geometric frustration of artificial magnetic skyrmion crystals", Physical Review B, 94, 144405 (2016).

14. Sihua Li, Sarjoosing Goolaup, Jaesuk Kwon, Feilong Luo, Christian Engel, **Weiliang Gan** and Wen Siang Lew, "Deterministic spin-orbit torque induced magnetization reversal in Pt/[Co/Ni]2/Ta structure", Scientific Reports, 7, 972(2017).

15. Christian Engel, Sarjoosing Goolaup, Feilong Luo, **Weiliang Gan**, and Wen Siang Lew, "Spin-orbit torque induced magnetization anisotropy modulation in Pt/(Co/Ni)4/Co/IrMn heterostructure", Journal of Applied Physics, 121, 143902 (2017).

16. Jaesuk Kwon, Sarjoosing Goolaup, **Weiliang Gan**, Chang Chip Hong, Kaushik Roy, and Lew Wen Siang, "Asymmetrical domain wall propagation in bifurcated PMA wire structure due to the Dzyaloshinskii-Moriya interaction", Applied Physics Letters, 110, 232402 (2017).

17. Pankaj Sethi, Sachin Krishnia, **Weiliang Gan**, Farhan Nur Kholid, Tan Funan, Ramu Maddu and Lew Wen Siang, "Bi-directional high-speed domain wall motion in perpendicular magnetic anisotropy Co/Pt double stack nanowires", Scientific Reports, 7, 4964 (2017).

18. Wong De Wei, **Weiliang Gan**, N. Liu and Lew Wen Siang, "Magneto-actuated cell apoptosis by biaxial pulsed magnetic field", Scientific Reports 7, 10919 (2017).

19. Sachin Krishnia, Pankaj Sethi, **Weiliang Gan**, Farhan Nur Kholid, Ramu Maddu, Herng Tun Seng, Ding Jun, Indra Purnama, and Lew Wen Siang, "Role of RKKY torque on domain wall motion in synthetic antiferromagnetic nanowires with opposite spin Hall angles", Scientific Reports, 7, 11715 (2017).

20. Jiangwei Cao, Yifei Chen, Tianli Jin, **Weiliang Gan**, Ying Wang, Yuqiang Zheng, Hua Lv, Susana Cardoso, Dan Wei, Wen Siang Lew, "Spin-orbit torques induced magnetization reversal through asymmetric domain wall propagation in Ta/CoFeB/MgO structures", Scientific Reports, 8, 1355 (2018).

21. Wong Qiying, **Weiliang Gan**, Feilong Luo, Gerard Joseph Lim Chu Keong, Calvin Ang Ching Ian, Tan Funan, Law Waicheung, Lew Wen Siang, "In-Situ Kerr harmonic measurement in determining current-induced effective fields in MgO/CoFeB/Ta", Journal of Physics D: Applied Physics, 51, 115004 (2018).

22. Wong De Wei, **Weiliang Gan**, Teo Yuan Kai and Lew Wen Siang, "Interplay of cell death signalling pathways mediated by alternating magnetic field gradient", Cell Death Discovery, 4, 49 (2018)

23. Jose Martinez, Cong Son Ho, Zhuo Bin Siu, Mansoor bin Abdul Jalil, Wen Siang Lew, and **Weiliang Gan**, "Theory of current-induced skyrmion dynamics close to a boundary", Journal of Magnetism and Magnetic Materials, 465, 685 (2018).

24. Tianli Jin, Durgesh Kumar, **Weiliang Gan**, Mojtaba Ranjbar, Rachid Sbiaa, Feilong Luo, Xiaoxi Liu, Wen Siang Lew, and S. Piramanayagam, "Nanoscale compositional modification in Co/Pd multilayers for controllable domain wall pinning in racetrack memory", Physica Status Solidi (RRL), 1800197 (2018).

25. Law Waicheung, Taiebeh Tahmasebi, Tan Funan, Jin Tianli, **Weiliang Gan**, Ramesh Rao Nistala, X.T. Zhu, Z.Q. Mo, H.W. Teo, Seet Chim Seng, A. See, S.N. Piramanayagam, and Lew Wen Siang, "High-temperature Ferromagnetic Resonance study on pMTJ stacks with diffusion barrier layers", Journal of Physics D: Applied Physics, 51, 405001 (2018).

26. Li Sihua, Gerard Joseph Lim Chu Keong, **Weiliang Gan**, W.C. Law, Tan Funan and Lew Wen Siang, "Tuning the spin-orbit torque effective fields by varying Pt insertion layer thickness in perpendicularly magnetized Pt/Co/Pt(t)/Ta structures", Journal of Magnetism and Magnetic Materials, 473, 394 (2018).

27. Tianli Jin, **Weiliang Gan**, Chuang Ma, Rudolf Schaefer, Funan Tan, Wen Siang Lew, Ivan Soldatov, Xiaoxi Liu, Law Wai Cheung, SN Piramanayagam, "Nanoscale modification of magnetic properties for effective domain wall pinning", Journal of Magnetism and Magnetic Materials, 475, 70 (2019).

28. Sachin Krishnia, Pankaj Sethi, **Weiliang Gan**, Wong Qiying, Gerard Joseph Lim Chu Keong, and Lew Wen Siang, "Spin orbit torque induced effective field modulation in synthetic antiferromagnetic strcuture", Journal of Magnetism and Magnetic Materials, 475, 327 (2019).

29. Wong Qiying, Chandrasekhar Murapaka, Law Waicheung, **Weiliang Gan**, Gerard Joseph Lim Chu Keong, Lew Wen Siang, "Enhanced Spin-orbit Torques in Rare Earth Pt/[CoNi]2/Co/Tb systems", Physical Review Applied, 11, 024057 (2019).

30. Calvin Ang Ching Ian, **Weiliang Gan**, and Lew Wen Siang, "Bilayer skyrmion dynamics on a magnetic anisotropy gradient", New Journal of Physics, 21, 043006 (2019).

31. Funan Tan, Q.Y. Wong, **Weiliang Gan**, Li Sihua, Liu Hongxi, Francis Poh, and W.S. Lew,"Electric field control for energy-efficient domain wall injection", Journal of Magnetism and Magnetic Materials, 485, 174 (2019).

32. Funan Tan, **Weiliang Gan**, Calvin Ang Ching Ian, G.D.H. Wong, Liu Hongxi, Francis Poh, Danny Shum, and Lew Wen Siang, "High-velocity domain wall propagation using voltage-controlled magnetic anisotropy", Scientific Reports, 9, 7369 (2019).

33. Tianli Jin, Funan Tan, Calvin Ang Ching Ian, **Weiliang Gan**, Jiangwei Cao, Wen Siang Lew, S. N. Piramanayagam, "Tilted magnetisation for domain wall pinning in racetrack memory", Journal of Magnetism and Magnetic Materials, 489, 165410 (2019).

34. Tetsuya Hajiri, Lorenzo Baldrati, Romain Lebrun, Mariia Filianina, Andrew Ross, N. Tanahashi, M. Kuroda, **Weiliang Gan**, Tevfik Onur Menteş, Francesca Genuzio, Andrea Locatelli, H. Asano, Mathias Klaui, “Spin structure and spin Hall magnetoresistance of epitaxial thin films of the insulating non-collinear antiferromagnet SmFeO3”, Journal of Physics: Condensed Matter, accepted.

35. Jin Tianli, **Weiliang Gan**, Tan Funan, Nicolo Sernicola, Lew Wen Siang, S. N. Piramanayagam, “Synaptic Element for Neuromorphic Computing Using a Magnetic Domain Wall Device with Synthetic Pinning Sites”, Journal of Physics D: Applied Physics, accepted.

36. Kang Lixing, Yu Xuechao, Zhao Xiaoxu, Ouyang Qingling, Di Jun; Xu Manzhang, Tian Dan, **Weiliang Gan**, Calvin Ang Ching Ian, Ning Shoucong, Fu Qundong, Zhou Jiadong, Kutty, R. Govindan, Deng Ya, Song Pin, Zeng Qingsheng, Stephen J. Pennycook, Wang Qi Jie, Shen Jun, Yong Ken-Tye, Liu Zheng, "Space-confined Microwave Synthesis of Ternary Layered BiOCl Crystals with High-Performance Ultraviolet Photodetection", InfoMat, accepted.

37. Li Yong, Feng Qiyuan, Li Sihua, Huang Ke, **Weiliang Gan**, Zhou Haibiao, Jin Xiangjun, Cao Liang, Wang Renshaw, Ma Fusheng, Lu Qingyou, and Lew Wen Siang, “An IEC Synthetic Skyrmion Platform with Robust Tunability”, Advanced Materials, submitted.

List of Conference Presentations

1) “Role of effective anisotropy in temperature gradient-induced skyrmion motion”
   X. Wang, W. L. Gan, T. L. Tian, and Wen Siang Lew
   INTERMAG 2018, Singapore

2) “Pinning sites with tiled magnetisation for domain wall motion control in racetrack memory”
   T.L. Jin, F.N. Tan, W.L. Gan, , J.W. Cao, W. S.Lew, and S. Piramanayagam
   INTERMAG 2018, Singapore

3) “High speed bilayer skyrmion transport by voltage controlled magnetic anisotropy gradient”
   C. C.I. Ang, W.L. Gan, Wen Siang Lew
   INTERMAG 2018, Singapore

4) “*In-situ* high temperature FMR measurements of pMTJ with various diffusion barrier cap”
   Wai Cheung Law, Taiebeh Tahmasebi, Funan Tan, Weiliang Gan, Gerard Joseph Lim, Seet Chim Seng, Alex See, Wen Siang Lew
   62nd Annual Conference on Magnetism and Magnetic Materials (MMM 2017), Pittsburgh, USA

5) “H_Z-biased Field Modulation of The Harmonic Measurement In The Determination Of The Effective Fields In MgO/CoFeB/W”
   Q.Y. Wong, G.J. Lim, W.L. Gan, W.S. Lew
   62nd Annual Conference on Magnetism and Magnetic Materials (MMM 2017), Pittsburgh, USA

6) “Observation of Large Planar Hall Effect on the Current Induced Spin-orbit Effective Fields in Ta/MgO/CoFeB/Ta”
   Q. Y. Wong, W.L. Gan, F.L Luo, and W.S. Lew*
   INTERMAG 2017, Dublin, Ireland

7) “SOT induced magnetization reversal in Pt/[Co/Ni]*2*/Co/Ta multilayer Hall bars without external magnetic field”
   Sihua Li, Sarjoosing Goolaup, Weiliang Gan and Wen Siang Lew
   INTERMAG 2017, Dublin, Ireland

8) “Skyrmion in-line injection and driving by spin Hall torque”
   Weiliang Gan, Sachin Krishnia, Qi Ying Wong, Wai Cheung Law, Gerard Joseph Lim and Wen Siang Lew
   INTERMAG 2017, Dublin, Ireland

9) “In vitro magneto-mechanical cancer cell destruction efficacy under biaxial DC pulsed magnetic field”
   D. W. Wong, W. L. Gan, N. Liu, and W. S. Lew
   INTERMAG 2017, Dublin, Ireland

10) "Quantifying data retention and the effect of radiation on domain wall memory devices"
S. Krishnia, P. Sethi, W. L. Gan, I. Purnama, R. Maddu, and W. S. Lew
INTERMAG 2017, Dublin, Ireland

11) "Angular dependence of spin-orbital torque induced magnetization switching in synthetic antiferromagnetic structures"
S. Krishnia, P. Sethi, W. L. Gan, Q. Y. Wong, and W. S. Lew
INTERMAG 2017, Dublin, Ireland

12) "Spin orbital torque induced effective field modulation in synthetic antiferromagnetic structures"
S. Krishnia, P. Sethi, W. L. Gan, Q. Y. Wong, and W. S. Lew
INTERMAG 2017, Dublin, Ireland

13) "Spin-orbit torque induced high speed domain wall motion in Co/Pt dual stack"
Pankaj Sethi, Sachin Krishnia, Weiliang Gan, Farhan N. Kholid, Ramu Maddu, Chen Yunjie, Leong Siang Huei, Wen Siang Lew
61st Annual Conference on Magnetism and Magnetic Materials (MMM 2016), New Orleans, USA

14) "Effect of the interlayer exchange torque on the domain wall dynamics in perpendicularly magnetized synthetic antiferromagnetic nanowires"
S. Krishnia, P. Sethi, W. L. Gan, F. N. Kholid, I. Purnama, M. Ramu, T. S. Herng, J. Ding and W. S. Lew*
61st Annual Conference on Magnetism and Magnetic Materials (MMM 2016), New Orleans, USA

15) "Stray field interference of free layer switching in perpendicular magnetic anisotropy magnetic tunnel junction"
D. W. Wong, N. Thiyagarajah, H. Yang, W. L. Gan, S. Ye, H. Cong, A. See, and W.S. Lew,
Magnetics Symposium 2016, Singapore

16) "Shape-dependent dynamics of skyrmion under spin orbit torque"
Indra Purnama, Weiliang Gan, and W.S. Lew,
The 4th International Conference of Asian Union of Magnetics Societies (IcAUMS 2016), Tainan, Taiwan

17) "Spin-related effects in heavy metal/ferromagnet/antiferromagnet layer structure"
C. Engel, Weiliang Gan, S. Goolaup and W. S. Lew,
The 4th International Conference of Asian Union of Magnetics Societies (IcAUMS 2016), Tainan, Taiwan

18) "Three terminal skyrmion device for memory applications"
W.L. Gan, H. T. Fook, and W.S. Lew,
The 4th International Conference of Asian Union of Magnetics Societies (IcAUMS 2016), Tainan, Taiwan

19) "Electric-field control of Skyrmion motion"
H. T. Fook, W.L. Gan, and W.S. Lew,

The 4th International Conference of Asian Union of Magnetics Societies (IcAUMS 2016), Tainan, Taiwan

20) “Dynamics and control of electric field-induced Skyrmion motion”
H. T. Fook, W.L. Gan, I Purnama and W.S. Lew,
2016 Joint MMM-Intermag Conference, San Diego, USA

21) “Highly efficient Skyrmion transport and nucleation using spin-orbit torque”
W.L. Gan, H. T. Fook, and W.S. Lew,
2016 Joint MMM-Intermag Conference, San Diego, USA

22) “Modified Thiele equation with spin orbit torque for Skyrmion dynamics”
Indra Purnama, S. G. Wu, W.L. Gan and W.S. Lew,
2016 Joint MMM-Intermag Conference, San Diego, USA

23) “Dynamics of Guided Skyrmions in Magnetic nanotracks” (invited)
Fusheng Ma, Wei Liang Gan, Hiu Tung Fook, Indra Purnama, Wen Siang Lew,
6th Annual Symposium on Magnetics 2015, Singapore

24) “Multi-vortex magnetic nanoparticles: A twin-functionalized agent for magnetomechanical cancer-cell destruction and hyperthermia”
D. W. Wong, N. Liu, C. B. Tan, W. L. Gan, , I. Purnama, and W. S. Lew,
The 20th International Conference on Magnetism 2015, Barcelona, Spain

25) “Skyrmion pinning dynamics in nanostructures for diode and symmetric operations”
H. T. Fook, C. C. I. Ang, W.L. Gan, I. Purnama, and W.S. Lew,
The 20th International Conference on Magnetism 2015, Barcelona, Spain

26) “Micromagnetics and emergent electrodynamics of skyrmions, and their application to skyrmion-based memory”
M. B. Jalil, W. L. Gan, and W. S. Lew
INTERMAG 2015, Beijing, PR China

27) “Determining pseudo-particle properties of skyrmion from its response to applied alternating current”
S. G. Wu, W. L. Gan, I. Purnama, W. S. Lew
INTERMAG 2015, Beijing, PR China

28) “2D transport of superparamagnetic microbeads on a ferromagnetic hexagonal nanolattice”
J.X. Chen, W. L. Gan, D. W. Wong, I. Purnama, W. S. Lew
INTERMAG 2015, Beijing, PR China

29) “Effects of geometry on skyrmion pinning and operation symmetry”
C. C. I. Ang, H. T. Fook, W.L. Gan, I. Purnama, and W.S. Lew,
INTERMAG 2015, Beijing, PR China

30) “Mitigation of magnus force in current-induced skyrmion dynamics”
H. T. Fook, C. C. I. Ang, W.L. Gan, I. Purnama, and W.S. Lew,,
INTERMAG 2015, Beijing, PR China

31) “Magnetic nanoparticles for magnetomechanical cell destruction and magnetic hyperthermia agents ”
D. W. Wong, Y. Yang, W. L. Gan, N. Liu, I. Purnama, M. Chandra Sekhar, S. Y. Wong, J. Ding and W. S. Lew
INTERMAG 2015, Beijing, PR China

32) “Quaternary memory based on magnetic skyrmion”
S. F. Zhang, W. L. Gan, I. S. Kerk, J. Kwon, F. L. Luo, J. B. Wang, Q. F. Liu, W. S. Lew
INTERMAG 2015, Beijing, PR China

33) “Guiding current-induced Skyrmion motion” (invited)
I. Purnama, W. L. Gan, D. W. Wong, and W. S. Lew
The 9th International Conference on Computational Physics 2015, Singapore

List of Intellectual Property

1) "**Electromagnet design for Kerr Imaging**",
   Weiliang Gan, and Wen Siang Lew
   Technology Disclosure, NTU ref TD/263/17 (2017),
   Singapore provisional patent application no: 10201800208W,
   NTU reference: PAT/263/17/18/SG PRV
   Licensed by: *Advanced Magnetic Devices Pte. Ltd.*

2) "**An apparatus and method for Kerr imaging**",
   Weiliang Gan, and Wen Siang Lew
   Singapore Provisional Patent 10201603665S (2016),
   PCT Application No : PCT/SG2017/050237
   Licensed by: *Vertisis Technology Pte. Ltd.*

3) "**A Method for Creating Spatially Non-Uniform Polarization**",
   Weiliang Gan, and Wen Siang Lew
   Technology Disclosure, NTU TD ref 2018-356 (2018).
   Licensed by: *Advanced Magnetic Devices Pte. Ltd.*

4) "**Motorized High-Resolution Rotation of Optics**",
   Weiliang Gan, and Wen Siang Lew
   Technology Disclosure, NTU TD ref 2018-357 (2018).
   Licensed by*: Advanced Magnetic Devices Pte. Ltd.*

5) "**A High Brightness Narrow Bandwidth Light Source**",
   Weiliang Gan, and Wen Siang Lew
   Technology Disclosure, NTU TD ref 2018-358(2018).
   Licensed by: *Advanced Magnetic Devices Pte. Ltd*.

6) "**Real-time 3D drift correction for Kerr Imaging**",
   Weiliang Gan, and Wen Siang Lew
   Technology Disclosure, NTU TD ref 2018-189 (2018).

7) "**Laser illumination system**",
   Weiliang Gan, and Wen Siang Lew
   Technology Disclosure, NTU ref TD/264/17 (2017).

8) "**Magnetic memory devices and methods of operating the same**",
   W.S. Lew, S.F. Zhang, W.L. Gan, and G.J. Lim
   PCT Application No: PCT/SG2016/050526 (2016).

9) "**Fabrication Of magnetic nanoparticles by electrodeposition and differential chemical etching techniques**",
   W.L. Gan, M. Chandra Sekhar, D.W. Wong, and W.S. Lew
   Technology Disclosure, NTU ref TD/083/14 (2013).